

AD-A148 371

COMBUSTION IN HIGH SPEED AIR FLOWS(U) SCIENCE
APPLICATIONS INC CHATSWORTH CA COMBUSTION SCIENCE AND
ADVANCED TECHNOLOGY DEPT R B EDELMAN ET AL. JUL 84

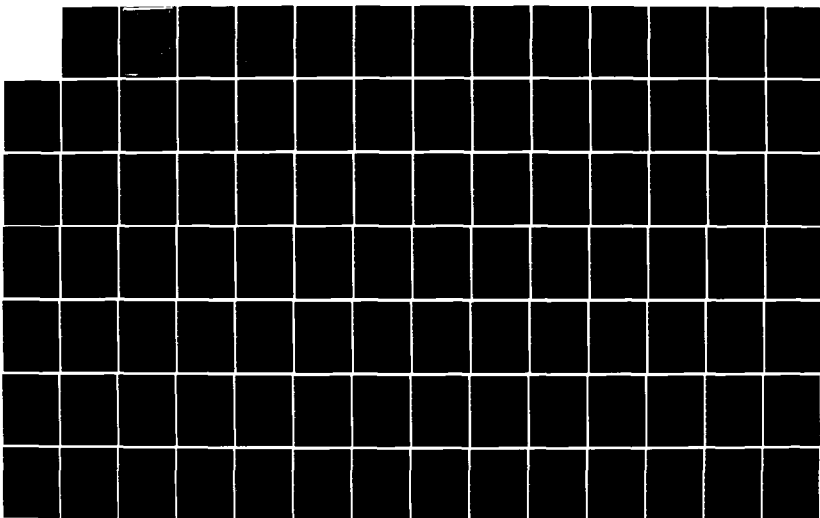
1/2

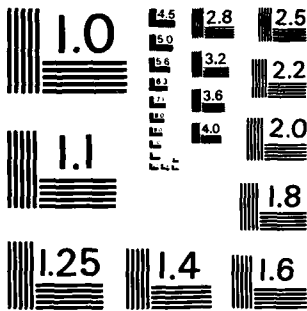
UNCLASSIFIED

AFOSR-TR-84-0924 F49620-80-C-0082

F/G 21/2

NL





MICROCOPY RESOLUTION TEST CHART
NATIONAL BUREAU OF STANDARDS-1963-A

AFOSR-TR- 84 0224

12

AD-A148 371

COMBUSTION IN HIGH SPEED

AIR FLOWS

FINAL REPORT

DTIC FILE COPY

DTIC
RECEIVED
DEC 10 1984
E

Approved for public release:
distribution unlimited.

SCIENCE APPLICATIONS, INC.
COMBUSTION SCIENCE AND ADVANCED TECHNOLOGY

84 11 20 015

54

188 19

12

COMBUSTION IN HIGH SPEED

AIR FLOWS

FINAL REPORT

R. B. Edelman
P. T. Harsha

SCIENCE APPLICATIONS, INC.
Combustion Science and Advanced Technology Dept.
9760 Owensmouth Avenue
Chatsworth, California 91311

Prepared for:

Air Force Office of Scientific Research
Bolling Air Force Base
Washington, D.C. 20332

F49620-80-C-0082

DEC 10 1984
E

AIR FORCE OFFICE OF SCIENTIFIC RESEARCH (AFSC)

NOTICE OF TRANSMITTAL TO AFSC

This technical report has been reviewed and approved for distribution by AFSC.

Distribution is unlimited.

MATTHEW J. KIRKPATRICK

July, 1984 Chief, Technical Information Division

TABLE OF CONTENTS

<u>Section</u>	<u>Page</u>
1. RESEARCH OBJECTIVES AND SUMMARY.	1
2. RESEARCH STATUS.	8
2.1 Spray Flame Model	8
2.2 Modeling of Boron Combustion Processes.	42
2.3 The Modular Model for Ramjet Performance Assessment	74
2.4 Modeling of the Ducted Rocket Combustion Process.	107
2.5 References.	113
3. PUBLICATIONS	115
4. PROFESSIONAL PERSONNEL	116
5. INTERACTIONS	117

Accession For	
NTIS GRA&I	<input checked="" type="checkbox"/>
DTIC TAB	<input type="checkbox"/>
Unannounced	<input type="checkbox"/>
Justification	
By _____	
Distribution/	
Availability	
Price	
A-1	



AIR FORCE OFFICE OF SCIENTIFIC RESEARCH (AFOSR)
 NOTICE OF FUNDING AWARD
 This technology is being developed under AFOSR contract number F49620-93-1-0012.
 approved for release
 Distribution is unlimited.
 MATTHEW J. KEENE
 Chief, Technical Information Division

LIST OF FIGURES

<u>Figure</u>		<u>Page</u>
1	Initial Droplet Size Distribution and Discretized Approximation.	21
2	Axial Variation of Centerline Velocity and Species Mass Fractions, Vaporizing Spray Jet	22
3	Radial Variation of Freon Concentration Vaporizing Spray Jet	24
4	Radial Variation of Axial Velocity, Vaporizing Spray Jet . .	25
5	Computed Evolution of Droplet Size Distribution, Vaporizing Spray Jet.	26
6	Comparison of Computed Centerline Temperature with Experimental Data, Pentaine Spray Flame.	28
7	Centerline Temperature Distribution Reacting n-Pentane Spray Jet, With and Without Gas-Phase Thermal Radiation.	30
8	Effects of Neglect of Mean Flow Buoyancy in Predicted Centerline Temperature Distribution.	31
9	Effects of Mean Flow Buoyancy on Centerline Velocity Distribution, Reacting n-Pentane Flame	33
10	Comparison of Computed and Measured Centerline Velocities, n-Pentane Spray Flame.	34
11	Radial Velocity Profile Comparison, n-Pentane Spray Flame. .	35
12	Reynolds Stress Profile, Reacting n-Pentane Jet.	36
13	Comparison of Computed and Measured Temperature Profiles, Pentane Spray Flame.	37
14	Temperature Contours in Initial Spray Flame Region.	40
15	Droplet Total Mass Fraction (all classes) Contours, Initial Spray Flame Region	41
16	Predicted Kinetic-to-Diffusion Controlled Combustion of Boron.	61
17	Effect of Pressure on Burn Time.	63
18	Comparison of Predictions with Data; Oxygen Concentration = 0.21, $T_{\text{Gas}} = 300^{\circ}\text{K}$	64
19	Comparison of Predictions with Data; Oxygen Concentration = 0.40, $T_{\text{Gas}} = 300^{\circ}\text{K}$	65

LIST OF FIGURES (CONT.)

<u>Figure</u>		<u>Page</u>
20	B_2O_3 Vapor Pressure Data	69
21	Surface Tension of B_2O_3	71
22	Effects of B_2O_3	72
23	Schematic of Sudden-Expansion (Dump) Burner.	75
24	Comparison of Well-Stirred Reactor with Recirculation Region Flowfield.. . . .	77
25	Predicted Fuel Mass Fraction Distributions for Simultaneous Injection at Three Radial Locations	89
26	Modular Model Calculation Logic.	91
27	Comparison of Predicted and Measured Combustion Efficiency and Wall Static Pressure Distributions, Premixed Sudden- Expansion Combustor, Global Finite-Rate Chemistry Model.	94
28	Comparison of Modular Model Prediction with Measured Dump Combustor Performance, Liquid Fuel Injection	97
29	Recirculation Zone Fuel Concentration.	99
30	Combustor Performance Prediction, Poppet Injection	100
31	Flowfield Streamlines, Sudden-Expansion with Swirl; Swirl No. = 2.0, Constant Angle.	104
32	Axial Velocity Profiles, $S = 0.4$, Different Initial Swirl Distributions.	105
33	Tangential Velocity Profiles, $S = 0.4$, Different Initial Swirl Distributions.	106
34	Schematic of Ducted Rocket Configuration for Aerodynamic Flowfield Analysis	109
36	Longitudinal Cross-Section through Inlet Arms, Ducted Rocket Combustor Aerodynamic Flowfield	111
37	Lateral Cross-Section through Inlet Arms, Ducted Rocket Combustor Aerodynamic Flowfield.	111

LIST OF TABLES

<u>Table</u>		<u>Page</u>
1	Turbulence Model Constants	13
2	Advanced Quasiglobal Kinetics Model for Aliphatic Fuels. .	18
3	Nomenclature for EQ's 1-17	19
4	Summary of Available Boron Ignition and Combustion Models.	44
5	Nomenclature for Expressions Summarized in Table 3	49
6	Toluene and Iso-Octane Quadiglobal Kinetics Model.	84
7	Finite Rate Kinetics Model Used in Ramjet Computations . .	87

1. RESEARCH OBJECTIVES AND SUMMARY

The results described in this report have been obtained from work whose overall objective is the analysis of reacting multiphase flows in advanced air-breathing propulsion systems. This work involves the formulation and evaluation of new theoretical descriptions of multiphase turbulent mixing and chemical kinetic phenomena in subsonic and supersonic air flows, and the generation of new experimental data on these phenomena. The specific objectives of this research may be described as follows:

- (a) Spray Modeling; This task area involves the development of analytical models of the phenomena occurring in the multiphase turbulent reacting flows involved in spray flame evolution. The model is to include the effects of heterogeneous and homogeneous finite rate chemical reaction, turbulent transport, and velocity and temperature nonequilibrium between the droplets and gas phase. Both liquid fuels and slurries are to be considered. The analytical modeling work is to be supplemented with experimental studies of spray injector characteristics and spray flame structure for both ramjet and gas turbine applications.
- (b) Modeling of Boron Combustion Processes; In this task area advanced analytical models of the combustion of boron particles are to be developed. A survey of the existing boron kinetics literature is to be performed to provide the data base for the development of advanced boron kinetics models. This survey leads to the definition of an advanced model for boron particle combustion, to be incorporated in modular models of slurry combustion process in ramjet. Required boron kinetics data are also to be defined.
- (c) Modeling of Ramjet Combustion Processes; The modular modeling approach to the analytical characterization of high speed combustion processes is to be further refined and developed, and applied to the analysis of results generated from experiments relevant to high speed combustion

processes. Model refinements including the advanced quasiglobal chemical kinetics model for the characterization of fuel-rich combustion of complex hydrocarbon fuels and the spray model formulations developed under item (a) above are to be incorporated. This modeling work will also emphasize slurry fuels, particularly boron slurries. Of specific importance in this area is the experimental data on gas-phase, liquid-phase, and slurry-fuel combustion phenomena being obtained at the Naval Weapons Center under a joint AFOSR/NWC sponsored program. Also of importance in this area is the continued development of unified elliptic computational techniques for modeling ramjet combustion processes.

- (d) Modeling of the Ducted Rocket Combustion Process. This task area involves the formulation and development of a modular model for the ducted rocket combustor. This model is to be based on a delineation of flow characteristic regions obtained through the use of three-dimensional elliptic aerodynamic calculations, and is to be used to develop a broad base of new and fundamental information on three-dimensional multi-stream interaction in reacting ducted flows.

Work carried out to meet these objectives during the contract period resulted in a number of significant accomplishments. In summary, these accomplishments include:

- (a) Development of a Comprehensive Spray Flame Model: A spray flame model was completed which includes sub-models for two-phase transport and diffusion, heterogeneous and homogeneous combustion kinetics, turbulent mixing, gas-phase radiation, and buoyancy effects. Based on the assumption of near dynamic equilibrium, this approach allows a detailed computation of the evolution of the droplet size distribution throughout the flame, and incorporates the advanced quasiglobal

kinetics model to accurately account for gas-phase hydrocarbon combustion processes in fuel-rich regions of the flame. Utilization of the model to predict spray flame development has shown the necessity of incorporating accurate representations of physical processes which control the flame development, including those mechanisms which occur on a droplet scale but also including gas-phase phenomena involving finite-rate kinetics, thermal radiation, and, for the flowfield considered, buoyancy. The computer model that has been developed from this work provides a generalized framework for the development and testing, in conjunction with key experimental data, of physically perceptive models of the many mechanisms involved in spray combustion.

(b) Development of an Accurate Boron Combustion Model:

Based on the results of a survey of boron combustion modeling, an exiting model in which both diffusion and chemical kinetics mechanisms are implemented was selected for further development. The model is based on a clean-particle assumption - it is assumed that no B_2O_3 layer is present. Since particle consumption at a significant rate can only occur for clean particles, this approach allows examination of the effects of kinetics limitations on boron consumption rate. The model, coupling finite rate oxidation kinetics and diffusional mechanisms, shows excellent agreement with experimental data for boron particle burn time as a function of particle size, temperature and pressure. Further, the model indicates that kinetics effects enter over the entire size range of interest. The model results also predict quenching for certain combinations of particle size, environment pressure and temperature, and environment O_2 concentration. These results indicate a critical balance between heat generation and heat

loss on the particle scale, indicating that the coupling of fluid dynamics and particle cloud processes is of fundamental importance in the combustion of boron in practical systems.

- (c) Modeling of Ramjet Combustion Processes: Under this program, a detailed modular model for sudden-expansion ramjet combustor performance evaluation was completed. This model combines state-of-the-art representations of the turbulent mixing and chemical kinetics rate processes with submodels for the fuel injection, vaporization and mixing phenomena in the combustor inlet. It is founded on the use of a perfectly-stirred reactor model to represent large-scale recirculation regions in the combustor and, in particular, the flame stabilization characteristics of these regions. A variety of computations have been carried out using this approach, under this and other Air Force- and Navy- sponsored programs, to analyze and interpret experimental data obtained using a variety of sudden-expansion ramjet configurations. Results of this work have demonstrated the role of the sudden-expansion recirculation regions in flame stabilization at lower Mach numbers, that performance fall-off at high overall fuel-air ratios at moderate flight Mach numbers can be directly related to the effects of fuel-rich combustion in large regions of the combustor flow-field, and that a desirable fuel distribution at high Mach number is considerably different from that which is desirable at lower Mach numbers. All of these results provide a critical input to the analysis and interpretation of ramjet performance data.

In addition to the modular approach, development of elliptic Navier-Stokes solution techniques has also continued. This work has centered on the examination of turbulence models, and has shown that

the algebraic stress modeling approach can provide a potentially more valid description of turbulent mixing in combustor flowfields. The increased generality of the algebraic stress modeling approach is of particular importance in swirling flows where large-scale non-isotropy of the apparent viscosity is evident. At the same time, this work has demonstrated that for many combustors of interest, for example, axisymmetric sudden expansions with area ratios of four or more, inertia effects dominate in much of the flow, thus reducing the effect of choice of turbulence model on the overall flow-field prediction.

- (d) Ducted Rocket Model Development: Work in this area focused on the examination of different techniques for the prediction of ducted rocket flowfields and performance. Aerodynamic flowfield predictions were carried out for a representative combustor flowfield, but without simulation of the gas generator exhaust. Limited modular model evaluation of ducted rocket performance characteristics was also accomplished. Examination of available modeling approaches applicable to the ducted rocket showed that none examined accounted for the mixing and shock interaction effects of a highly underexpanded gas generator fuel jet. The existence of this key feature of the flowfield, which may well dominate the overall flow structure, should be included in any ducted rocket modeling approach.

Although as noted in the proceeding paragraphs, there have been considerable advances made in each of the research areas considered under this project, profitable research work can still be carried out in each of these areas. In the following paragraphs the research recommendations that result from the work already done are outlined:

- (a) Spray Modeling: Two avenues of approach can be taken in further spray modeling work. With the existing model,

experiments can be designed which will closely approximate the model assumption, so that direct comparisons of the various aspects of the model predictions which data can be made. In this way, each of the submodels incorporated in the overall spray model can be examined, to provide information on, for example, the effects and importance of droplet interactions, droplet/turbulence, combustion/turbulence and radiation/turbulence interactions, and the effects of different diffusion rates for droplet and gas phase. This would then provide a wealth of further data on droplet transport and spray combustion phenomena in a regime where the droplet and gas phase motions are nearly in equilibrium. The second avenue of investigation involves the relaxation of the near equilibrium hypothesis. Within the context of the present model an Eulerian formulation for droplet transport can be constructed, and a Lagrangian formulation can also be defined. Note that by carrying out such an analysis for a flowfield which in general satisfies the boundary layer assumptions, as in the present spray flame formulation, many of the numerical problems inherent in elliptic Navier-Stokes solution techniques can be avoided, an important consideration in establishing an understanding of the phenomena while maintaining relevance to airbreathing propulsion systems.

- (b) Boron Combustion Modeling: Work accomplished to date shows the importance of incorporating both diffusional and kinetics mechanisms in developing an accurate model for particle-scale boron combustion processes. There are several areas of research and model improvement that this work suggest. Extension of the model to include the effects of the existence of an oxide layer is clearly a critical need with respect to the practical use of the existing approach. At the same time, there are several other areas which require continued research. For example, the potential importance of suboxide formation and disposal is at the present unclear and requires further investigation, while more mechanistic models of B-O, B-O-H, and B-O-H-C kinetics

are also needed. Further, finite rate condensation of B_2O_3 is important in the overall heat release process, and itself represents an important area of continued research related to problems of boron combustion.

- (c) Modeling of Ramjet Combustion Processes: Work carried out under this and other programs has shown the fundamental advantages that can be gained through the use of a detailed and mechanistic modular model of the ramjet combustion process. The modular model developed in this work is however, limited to nonswirling sudden expansion flowfields. Similar approaches can be developed for swirl flow in subsonic combustors and for supersonic combustion applications. At the same time, fundamental model development work is required using unified Navier-Stokes approaches, and expanding the capabilities of these models to characterize flowfields with chemical reactions. This in turn indicates a need for the continued development of simple yet sufficiently general hydrocarbon chemical kinetics models as well as broadening the delineation of the regimes of model applicability.
- (d) Ducted Rocket Model Development: There is a dearth of information on the mixing characteristics of turbulent recirculating flows with embedded supersonic, under-expanded jets, yet this type of combined flowfield is central to the ducted rocket configuration. Clearly a need exists to explore the characteristics of these flows, both experimentally and through the development of theoretical models, in order to develop the understanding necessary to control them in practical applications.

2. RESEARCH STATUS

2.1 SPRAY FLAME MODEL

The spray flame model developed under this program applies to the near-dynamic equilibrium, thermal nonequilibrium limit of a two-phase flow. Thus, it is assumed that the mean velocity of both the droplets and the gas phase is nearly the same, but diffusion of particles relative to the gas phase is allowed. Gradient diffusion is assumed, with an apparent eddy viscosity that can be different from that which applies to the gas phase. The conditions required for the near-dynamic equilibrium assumption to be valid are clearly not met near the exit of a spray nozzle injecting fuel into a quiescent ambient. Nevertheless, the extent of the region in which this assumption is not valid is not well known, and it can be expected to become more valid as the spray flame flowfield develops. Thus it is of interest to investigate the capabilities of the approach, noting that when liquid fuels are injected using air streams to accomplish primary atomization, the near dynamic equilibrium assumption may indeed be reasonably valid over most of the flow.

2.1.1 Governing Equations

Governing equations for the two-phase spray flame flowfield are obtained following the development outlined in Ref. 1. A key element of this analysis involves the definition of the turbulent fluxes and their relationship to the gradients of the appropriate mean quantities. The "near" equilibrium concept simply recognizes that an exact equality in velocities between the phases does not exist, but that it is meaningful to characterize the global system with a single barycentric velocity in direct analogy with molecular diffusion. It is assumed that the droplets form a dilute suspension in the gas flow, and can be treated using continuum concepts. Thus the continuous distribution of droplet sizes within

the spray flame is discretized into a number of classes, each of which contains all droplets in a given size range about the average range for the class. These classes are then treated as droplet-phase "species", and transport equations are written for each class. For example, if the droplet distribution function in terms of droplet radius is discretized into a number of radius intervals, the independent variable becomes the droplet number density for a given size, defined as the total droplet mass of a given size range per unit volume. The total droplet density is obtained by summing over the droplet size distribution function, and the partial and total particle densities are determined through solution of appropriate transport equations.

The diffusivities of the droplets will generally be different from that which pertains to the gas phase components, precluding a straightforward application of Fick's Law to the global droplet-gas system. A multicomponent diffusion law can be developed, however, by treating each droplet class and the gas phase as a binary subsystem to which Fick's Law may be applied.

The basic governing equations are then as follows; where the nomenclature is as described in Table 3 following Eq. (17).

Global Continuity

$$\frac{\partial r \rho u}{\partial x} + \frac{\partial r \rho v}{\partial r} = 0 \quad (1)$$

Momentum

$$\rho u \frac{\partial u}{\partial x} + \rho v \frac{\partial u}{\partial r} = \frac{1}{r} \frac{\partial}{\partial r} \left[r \rho c_{vg} (\alpha_g + \sum_j \sigma_j \beta_{pj}) \frac{\partial u}{\partial r} \right] - (\rho - \rho_\infty) g \quad (2)$$

Gas Phase Species Transport, i^{th} Gas Phase Species

$$\rho u \frac{\partial \alpha_i}{\partial x} + \rho v \frac{\partial \alpha_i}{\partial r} = \frac{1}{r} \frac{\partial}{\partial r} \left\{ r \rho \frac{\epsilon_{vg}}{Sc} \left[\frac{\partial \alpha_i}{\partial r} - \alpha_i \left(\frac{1 - \sum_j \theta_j \beta_{pj}}{\alpha_g} \frac{\partial \alpha_g}{\partial r} + \sum_j \theta_j \frac{\partial \beta_{pj}}{\partial r} \right) \right] \right\} + \dot{w}_{gi}^C + \dot{w}_{pij}^F \quad (3)$$

Droplet Phase "Species" Transport, j^{th} Droplet Class

$$\rho u \frac{\partial \beta_{pj}}{\partial x} + \rho v \frac{\partial \beta_{pj}}{\partial r} = \frac{1}{r} \frac{\partial}{\partial r} \left\{ r \rho \frac{\epsilon_{vg}}{Sc} \theta_j \left[\frac{\partial \beta_{pj}}{\partial r} - \beta_{pj} \left(\frac{1 - \sum_k \frac{\theta_k \beta_{pk}}{\theta_j}}{\alpha_g} \frac{\partial \alpha_g}{\partial r} + \sum_k \frac{\theta_k}{\theta_j} \frac{\partial \beta_{pk}}{\partial r} \right) \right] \right\} + \dot{w}_{pj}^F \quad (4)$$

Mixture Energy Equation

$$\rho u \frac{\partial H}{\partial x} + \rho v \frac{\partial H}{\partial r} = \frac{1}{r} \frac{\partial}{\partial r} \left\{ r \rho \epsilon_{vg} \left\{ \frac{1}{Pr} \frac{\partial H}{\partial r} + \left[h_g \frac{1}{Sc} \sum_j \theta_j \beta_{pj} - \frac{H_g}{Pr} - \frac{1}{Pr} \left(\frac{Pr}{Sc} - 1 \right) h_g - \frac{1}{Sc} \sum_j \theta_j h_{pj} \beta_{pj} \left(\frac{1 - \sum_k \frac{\theta_k \beta_{pk}}{\theta_j}}{\alpha_g} \right) \right] \frac{\partial \alpha_g}{\partial r} \right\} \right\} +$$

Mixture Energy Equation (cont'd).

$$\begin{aligned}
 & - \frac{1}{Pr} \sum_j \beta_{pj} (\delta_{pj} - 1) \frac{\partial h_{pj}}{\partial r} + \frac{1}{Pr} \left(\frac{Pr}{Sc} - 1 \right) \cdot \\
 & \sum_i h_{ig} \frac{\partial \alpha_i}{\partial r} + \sum_j \left[\theta_j \frac{(h_{pj} - h_g \alpha_g)}{Sc} - \frac{h_{pj}}{Pr} \right] \cdot \\
 & \frac{\partial \beta_{pj}}{\partial r} + \left[\beta_g \left(1 - \frac{1}{Pr} \right) - \sum_i \beta_{pi} \frac{\delta_i}{Pr} \right] \frac{\partial (u^2/2)}{\partial r} - \\
 & \frac{1}{Sc} \left(\sum_j \beta_{pj} h_{pj} \right) \left(\sum_k \theta_k \frac{\partial \beta_{pk}}{\partial r} \right) \Bigg] \Bigg] - \rho u g - q'' R
 \end{aligned} \quad (5)$$

Droplet Energy Equation for j^{th} Droplet Class

$$\begin{aligned}
 \beta_{pj} \left(\rho u \frac{\partial h_{pj}}{\partial x} + \rho v \frac{\partial h_{pj}}{\partial r} \right) &= \dot{q}_{pj} + \frac{1}{r} \frac{\partial}{\partial r} \left(r \frac{\delta_{pj}}{Pr} \rho c_{vg} \beta_{pj} \cdot \right. \\
 & \left. \frac{\partial h_{pj}}{\partial r} \right) - \frac{\rho c_{vg}}{Sc} \theta_j \left\{ \frac{\partial \beta_{pj}}{\partial r} - \right. \\
 & \left. \beta_{pj} \left[\frac{(1 - \sum_k \theta_k \beta_{pk})}{\alpha_g} \frac{\partial \alpha_g}{\partial r} + \right. \right. \\
 & \left. \left. \sum_k \theta_k \frac{\partial \beta_{pk}}{\partial r} \right] \right\} \frac{\partial h_{pj}}{\partial r}
 \end{aligned} \quad (6)$$

The mixture density is given by the equation of state

$$\rho = P / [R_0 T_g (\sum_i \frac{\alpha_i}{W_i})] \quad (7)$$

where W_i is the molecular weight of gas phase species i , R_0 is the universal gas constant, and T_g is the local gas temperature.

To close the equation set and complete the model, a variety of additional submodels are required. These include models for the various production rate terms \dot{w}_{gi}^C , \dot{w}_{pj}^F , and \dot{w}_{pij}^F ; an expression for the thermal energy transferred to the droplets, \dot{q}_{pj} and the radiative energy transfer from the system, \dot{q}^R ; a droplet tracking scheme; and a turbulence model to define the effective gas-phase eddy diffusivity, ϵ_{vg} .

Turbulence Model

Turbulent transport, including the effects of buoyancy, is modeled using a two-equation formulation along with a temperature fluctuation equation. This results in a "three-equation" formulation, developed under a modified version of the Boussinesq hypothesis in which density fluctuations are neglected everywhere except when they appear in a buoyancy term. Writing density fluctuations in terms of temperature fluctuations leads to a formulation in which the buoyancy term in the turbulent kinetic energy balance is related to the root mean square of the temperature fluctuation, (Ref. 2) Thus the turbulence model is given by

$$\rho \epsilon_{vg} = \mu_T = c_\mu \frac{k^2}{\epsilon} \quad (8)$$

in which k and ϵ are obtained through solution of the equation for

Turbulent Kinetic Energy

$$\rho u \frac{\partial k}{\partial x} + \rho v \frac{\partial k}{\partial r} = \frac{1}{r} \frac{\partial}{\partial r} \left(r \frac{\mu_T}{\sigma_k} \frac{\partial k}{\partial r} \right) + \mu_T \left(\frac{\partial u}{\partial r} \right)^2 - \rho \epsilon + \rho g B C_k (qk)^{\frac{1}{2}} \quad (9)$$

Turbulent Kinetic Energy Dissipation Rate

$$\rho u \frac{\partial \epsilon}{\partial x} + \rho v \frac{\partial \epsilon}{\partial r} = \frac{1}{r} \frac{\partial}{\partial r} \left(r \frac{\mu_T}{\sigma_\epsilon} \frac{\partial \epsilon}{\partial r} \right) + C_1 \frac{\epsilon}{k} \mu_T \left(\frac{\partial u}{\partial r} \right)^2 - C_2 \frac{\rho \epsilon}{k} + C_3 C_4 \rho g \beta \epsilon (q/k)^{1/2} \quad (10)$$

and the temperature fluctuation, $[(T')^2]^{1/2} \equiv q$ is obtained through the solution of a

Temperature Fluctuation Transport Equation

$$\rho u \frac{\partial q}{\partial x} + \rho v \frac{\partial q}{\partial r} = \frac{1}{r} \frac{\partial}{\partial r} \left(r \frac{\mu_T}{\sigma_q} \frac{\partial q}{\partial r} \right) + C_{q1} \mu_T \left(\frac{\partial T}{\partial r} \right)^2 - C_{q2} \rho \frac{\epsilon}{k} q \quad (11)$$

This formulation introduces seven adjustable constants and three turbulent exchange coefficients. For most of the work described in this paper a single set of constants and coefficients was used in the turbulence model, as noted in Table 1. The basic turbulence model coefficients: C_μ , C_1 , C_2 , σ_k , and σ_ϵ were obtained from an extensive study of turbulent flowfield modeling reported in Ref. 3 while the coefficients used in the buoyancy modeling C_3 , C_4 , C_{q1} , C_{q2} , and σ_q were evaluated through comparison of nonreacting hot jet predictions with experimental data.

Table 1 Turbulence Model Constants

Parameter	C_μ	C_1	C_2	C_3	C_4	C_{q1}	C_{q2}	σ_k	σ_g	σ_q
Value	0.09	1.44	1.84	2.0	0.5	2.7	1.8	1.0	1.3	0.7

Droplet Tracking Methodology

The spray flame model requires a droplet tracking and category readjustment methodology, since the rate processes result in droplet size changes and these, and the diffusion of droplets of different classes, alter the droplet distribution at each local point in the flow. At each step in the computation a new average size for each class must be defined, based on the alterations that result from diffusion and rate processes. This procedure follows the methodology outlined in Ref. 4; in it the appropriate drop-size average is defined through conservation of mass and conservation of the parameter defining the dominant rate process affecting droplet size. Thus, if the rate process is dependent on radius to the power q , the appropriate expression for the new average radius is given by

$$\bar{r}_j^{n+1,m} = \left\{ \frac{\beta_{pj}^k + \Delta\beta_{pj1} + \Delta\beta_{pj2} + \Delta\beta_{pj3}}{\frac{\beta_{pj}^k}{(r_j^{n,m})^k} + \frac{\Delta\beta_{pj1}}{(r_j^{n,m+1})^{3-q}} + \frac{\Delta\beta_{pj2}}{(r_j^{n,m})^{3-q}} + \frac{\Delta\beta_{pj3}}{(r_j^{n,m-1})^{3-q}}} \right\}^{\frac{1}{3-q}} \quad (12)$$

where the averaging has been done assuming a three-point explicit finite difference scheme. The term $\beta_{pj}^{n,m}$ is the mass fraction of droplet class j at grid point n,m , the three diffusional components that contribute to the droplet class j at $n+1, m$ are $\Delta\beta_{pj1}$, $\Delta\beta_{pj2}$ and $\Delta\beta_{pj3}$; β_{pj}^k is the contribution from finite rate processes. Knowing the mass fraction and size, the number density of droplets of class j at point $n+1,m$ is then determined from

$$N_j^{n+1,m} = \rho^{n+1,m} \beta_{pj}^{n+1,m} / \left[\frac{4}{3} \pi \rho_L (r_j^{n+1,m})^3 \right] \quad (13)$$

Note that the commonly used Sauter mean diameter (SMD), given by the expression $d_{eff} = \sum N_j d_j^3 / \sum N_j d_j^2$ implies a d^2 or surface area dependent rate process, i.e., $q=2$ in Eq. (12). However, the " d^2 " law for vaporizing droplets implies a rate process that is proportional to the droplet diameter, so that, in Eq. (12) $q=1$. Somewhat different average radii will result depending on the governing rate process, and examination of calculational results shows that the use of $q=2$ (i.e., the SMD definition) in Eq. (12) yields a slightly different overall spray development than use of $q=1$ for a vaporizing spray. This difference is small for the conditions considered in this report, but in situations in which several different droplet-scale rate processes are occurring, the choice of average diameter definition may become more critical. Indeed under some circumstances it may be necessary to define more than one average diameter for each class of droplets.

Thermal Energy Transfer Terms

Two thermal energy transfer terms appear in the mixture energy and droplet-phase energy equations. These are \dot{q}^R , appearing in the mixture energy equation, which represents thermal energy transferred out of the flame by radiation, and \dot{q}_{pj} in the droplet energy equation, which represents a transfer of thermal energy to the droplets from the gas phase. Radiation from the flame to the surroundings is assumed to be dominated by gas phase CO_2 and H_2O emission, and is defined by an empirical expression, similar to that used in Ref. 5:

$$\dot{q}^R = 6.68 \times 10^{-12} T^4 [\alpha_{H_2O} \exp(-1.49 \times 10^{-3} T) + \alpha_{CO_2} \exp(-1.81 \times 10^{-3} T)] \quad (14)$$

yielding \dot{q}^R in BTU/ft²-sec with T in °K.

yielding \dot{q}^R in BTU/ft²-sec with T in °K.

Energy transfer between gas phase and particle is accounted for through relationships obtained (Ref. 6) using the classical spherical droplet, flame sheet approach and solving the resulting governing equations for the droplet heat and mass transfer processes. For a vaporizing droplet, and accounting for droplet-gas heat transfer resulting from both conduction and radiation, this yields an expression for the energy transfer to the droplet of the form

$$\dot{q}_{pj} = \frac{38 p_j}{r_j \rho_L} \rho \left\{ \frac{\lambda Nu}{2 r_j} [(T_g - T_L) - \frac{L}{C_p}] - \epsilon \sigma (T_L^4 - T_g^4) \right\} \quad (15)$$

Production Rate Terms

Three species production rate terms appear in the formulation. These involve production of gas phase species i through gas phase chemical reaction, \dot{w}_{gi}^C , production of droplet class j from other droplet classes through the effects of vaporization and combustion, \dot{w}_{pj}^F , and production of gas phase species i through vaporization or combustion of droplet class j, \dot{w}_{pij}^F .

The mass change of droplet class j per unit volume of mixture per unit time is evaluated using the classical spherical droplet-flame sheet model. Thus the rate of change of droplet mass is given by

$$\dot{w}_{pj}^F = 38 p_j \frac{\lambda}{C_p \rho_L r_j^2} \ln(1+B) \quad (16)$$

where the transfer number, B, is given by

$$B = \frac{1}{C_p} [C_p (T_g - T_d) + \frac{Q_{Y_{O_2}, \infty}}{T}] \quad (17)$$

The species produced from the droplet class j will be either fuel, in the case of vaporization, or CO₂ and H₂O if the droplet is burning. In the model described in this report, the droplet is assumed to burn if suffi-

cient oxygen is present in its immediate environment; otherwise a pure vaporization process takes place. Thus if $\alpha_{O_2} \geq 0.001$, the present model produces CO_2 , H_2O (and excess fuel) from a complete combustion process in the flame sheet, and otherwise only gas phase fuel is produced. This lower limit is of course arbitrary.

Gas phase chemical kinetics are evaluated using the advanced quasiglobal formulation described in Ref. 7. This approach includes models for the fuel pyrolysis process that occurs in high temperature, oxygen deficient regions, and thus eliminates the inaccuracy evident in the original quasiglobal model formulation (Ref. 8) when applied to fuel-rich combustion. In the advanced quasiglobal kinetics approach, the fuel to be modeled is broken down into aromatic and aliphatic components, modeled using rates developed for toluene and iso-octane, respectively. That is, the model fuel component which can be treated as aromatic is assigned rates which have been developed by extensive comparison of toluene predictions with experimental data, and the model fuel component that can be treated as aliphatic is assigned the rates developed for iso-octane. Each of these fuels break down into secondary fuels, C_2H_2 from toluene and C_2H_4 from iso-octane, following the pure pyrolysis pathway, as well as undergoing partial oxidation by attack from both O_2 and OH . The secondary fuels then react with the remaining OH and O_2 , and the wet CO mechanism follows.

For the computations to be described in this report, the fuel was pentane, so that only the aliphatic component needed to be included in the kinetics formulation. Since NO_x -formation reactions were also neglected, the gas-phase kinetics model used for these computations involved the 20 reactions among the 10 species shown in Table 2.

TABLE 2. ADVANCED QUASIGLOBAL KINETICS MODEL FOR ALIPHATIC FUELS

$$\text{FUEL} = \text{C}_N\text{H}_M$$

(a) SUBGLOBAL STEPS

$$k_f = AT^B \exp(-E/RT)$$

SUBGLOBAL MECHANISM	A	B	E/R	POWER DEPENDENCE
Primary Fuel				
$\text{C}_N\text{H}_M \rightarrow \frac{N}{2}\text{C}_2\text{H}_4 + (\frac{M-2N}{2})\text{H}_2$	1.0473 E12	0	3.5229 E3	$[\text{C}_5\text{H}_{12}]^{1.0}$
$\text{C}_N\text{H}_M + \frac{N}{2}\text{O}_2 \rightarrow \text{NCO} + \frac{M}{2}\text{H}_2$	1.2900 E9	1	2.5160 E4	$[\text{C}_5\text{H}_{12}]^{0.5}[\text{O}_2]^{1.0}$
$\text{C}_N\text{H}_M + \text{OH} \rightarrow (\frac{2N-1}{4})\text{C}_2\text{H}_4 + 0.5\text{CO} + 0.5\text{H}_2\text{O} + (\frac{M-2N+1}{2})\text{H}_2$	2.0000 E17	0	1.4919 E4	$[\text{C}_5\text{H}_{12}]^{1.0}[\text{OH}]^{1.0}$
Secondary Fuel				
$\text{C}_2\text{H}_4 + 6\text{OH} \rightarrow 2\text{CO} + 2\text{H}_2\text{O} + \text{H}_2$	2.2020 E15	0	1.2079 E4	$[\text{C}_2\text{H}_4]^{1.0}[\text{OH}]^{1.0}$
$\text{C}_2\text{H}_4 + 2\text{OH} \rightarrow 2\text{CO} + 3\text{H}_2$	2.1129 E27	-3.0	6.3062 E3	$[\text{C}_2\text{H}_4]^{1.0}[\text{OH}]^{1.5}$
$\text{C}_2\text{H}_4 + \text{M} \rightarrow \text{C}_2\text{H}_2 + \text{H}_2 + \text{M}$	2.0893 E17	0	3.9810 E4	$[\text{C}_2\text{H}_4]^{1.0}[\text{M}]^{1.0}$
$\text{C}_2\text{H}_2 + 6\text{OH} \rightarrow 4\text{H}_2\text{O} + 2\text{CO}$	4.7850 E15	0	1.3883 E4	$[\text{C}_2\text{H}_2]^{1.0}[\text{OH}]^{1.0}$
$\text{C}_2\text{H}_2 + 2\text{OH} \rightarrow 2\text{CO} + 2\text{H}_2$	2.8000 E16	0	0	$[\text{C}_2\text{H}_2]^{1.0}[\text{OH}]^{1.5}$

(b) ELEMENTARY STEPS

$$k_f = AT^B \exp(-E/RT)$$

ELEMENTARY MECHANISM	A	B	E/R
$\text{CO} + \text{OH} = \text{H} + \text{CO}_2$	4.0000 E12	0	4.026 E3
$\text{OH} + \text{H}_2 = \text{H}_2\text{O} + \text{H}$	2.1900 E13	0	2.5900 E3
$\text{OH} + \text{OH} = \text{O} + \text{H}_2\text{O}$	6.0230 E12	0	5.5000 E2
$\text{O} + \text{H}_2 = \text{H} + \text{OH}$	1.8000 E10	1.0	4.4800 E3
$\text{H} + \text{O}_2 = \text{O} + \text{OH}$	1.2200 E17	-0.91	8.3090 E3
$\text{O}_2 + \text{H}_2 = \text{OH} + \text{OH}$	1.7000 E13	0	2.4070 E4
$\text{CO} + \text{O}_2 = \text{O} + \text{CO}_2$	3.0000 E12	0	2.5000 E4
$\text{M} + \text{O} + \text{H} = \text{OH} + \text{M}$	1.0000 E16	0	0
$\text{M} + \text{H} + \text{H} = \text{H}_2 + \text{M}$	5.0000 E15	0	0
$\text{M} + \text{H} + \text{OH} = \text{H}_2\text{O} + \text{M}$	8.4000 E21	-2.0	0
$\text{M} + \text{CO} + \text{O} = \text{CO}_2 + \text{M}$	6.0000 E13	0	0
$\text{M} + \text{O}_2 = \text{O} + \text{O} + \text{M}$	2.5500 E18	-1.0	5.9380 E4

TABLE 3. NOMENCLATURE FOR EQ'S. 1-17

B	transfer number, defined by Eq. 17	δ_{pj}	ratio of droplet class j and gas phase thermal diffusivities = $\frac{\epsilon_{Tj}}{(\epsilon_{vg}/Pr)} - \frac{c_{pg}}{c_{pj}}$
C_p	liquid phase specific heat	ϵ	turbulent kinetic energy dissipation rate
C_1	coefficients in turbulent kinetic energy dissipation rate equation, defined in Table 1.	ϵ_{Tj}	droplet phase thermal diffusivity, class j
C_2		ϵ_{vg}	gas phase eddy viscosity
C_3		λ	gas phase thermal conductivity
C_4	coefficients in temperature fluctuation equation, defined in Table 1.	ν_T	turbulent effective viscosity = $\rho \epsilon_{vg}$
C_q		ρ	mixture density
C_u	eddy viscosity coefficient, defined in Table 1	ρ_L	liquid density
e	droplet emissivity	ρ_∞	ambient density
g	gravitational constant	σ	Stefan-Boltzmann constant
H	Mixture total enthalpy per unit mass of mixture = $h_g + \sum_j \beta_j h_{pj} + u^2/2$	σ_j	ratio of eddy viscosity of droplet class j to gas phase eddy viscosity = $\epsilon_{vj}/\epsilon_{vg}$
h_g	Static enthalpy of gas phase per unit mass of mixture = $\sum_i \alpha_i h_i(T)$	σ_k	effective "Prandtl number" for turbulent kinetic energy, Table 1
h_{pj}	Static enthalpy of droplet class j per unit mass of droplet class j	σ_q	effective "Prandtl number" for temperature fluctuation, Table 1
J_{gi}	gas phase species i diffusional flux	σ_G	effective "Prandtl number" for turbulent energy dissipation, Table 1.
J_{pj}	droplet phase species j diffusional flux		
k	turbulent kinetic energy		
k_f	forward reaction rate coefficient, Table 2		
L	latent heat of vaporization per unit mass		
N_j	number density of droplets of class j, Eq. 13		
Nu	Nusselt number for gas-droplet heat transfer		
P	pressure		
Pr	turbulent Prandtl number		
q	root-mean-square temperature fluctuation		
\dot{q}^r	energy transfer from mixture by gas-phase radiation, Eq. 14		
\dot{q}_{pj}	energy transfer to droplet class j, Eq. 15		
Q	heat of vaporization		
r	radial coordinate		
r_j	radius of droplet of class j		
R_0	universal gas constant		
Sc	turbulent Schmidt number		
T_g	gas phase temperature		
T'	gas phase temperature fluctuation		
T_L	droplet temperature		
u	axial velocity		
v	radial velocity		
\dot{w}_{gi}	production of gas phase species i through chemical reaction		
\dot{w}_{pj}	production of droplet phase class j through effects of vaporization, combustion, and agglomeration, per unit volume of mixture per unit time		
\dot{w}_{pij}	production of gas phase species i through vaporization or combustion of droplet class j, per unit volume of mixture		
W_i	molecular weight of species i		
x	axial coordinate		
Y_0	oxygen concentration, fraction of gas phase		
α_g	mixture mass fraction of gas phase = $\sum_i \alpha_i$		
α_i	mixture mass fraction of species i		
β_{pj}	mixture mass fraction of droplet class j		

2.1.2 Comparison with Experimental Results

Vaporizing Spray

In Ref. 9, Shearer, et al. describe detailed measurements of mean velocity, total concentration (both liquid and vapor phase), and Reynolds stress which were made in a two-phase Freon-11/air jet mixing with still air. The jet was produced by the injection of Freon-11 into the air using an air-atomizing nozzle; the initial liquid-phase Freon mass fraction was 0.87. Shearer, et al. do not report droplet distributions; however, they give the initial SMD (Sauter mean diameter) of the Freon-11 droplets as 29 microns. The injection temperature of the Freon-11 was just below its saturation temperature, which in turn was just below the ambient air temperature. Thus the vaporization process for this jet was driven primarily by concentration gradients. Within the context of the model, this vaporization process was approximated by assuming a transfer number, B , of ten, in the droplet vaporization expression, Eq. (16). Vaporization was assumed to initiate when the droplet temperature reached the saturation temperature. An assumed initial droplet distribution, obtained from literature data for air-atomizing nozzles, was used to initiate the calculations; this distribution, shown in Fig. 1, has a 29μ SMD. All other initial conditions (i.e., velocity, temperature and droplet mass fraction, turbulence energy and dissipation rate) were taken to be uniform across the jet. All droplet classes were taken to diffuse at the same rate as the gas phase, i.e., $\theta_j=1$ for all j . The phenomenon of phase separation, or relative diffusion, is included in the formulation but in the absence of detailed data θ_j must be established parametrically, so that $\theta_j=1$ provides a reasonable baseline case.

Axial variations of centerline velocity and species mass fractions are compared with the data of Shearer, et al. in Fig. 2. As noted on the figure, these computations have been carried out for a turbulent Prandtl number of 0.70. These results indicate that the predicted velocity profile compares reasonably well with the experimental results,

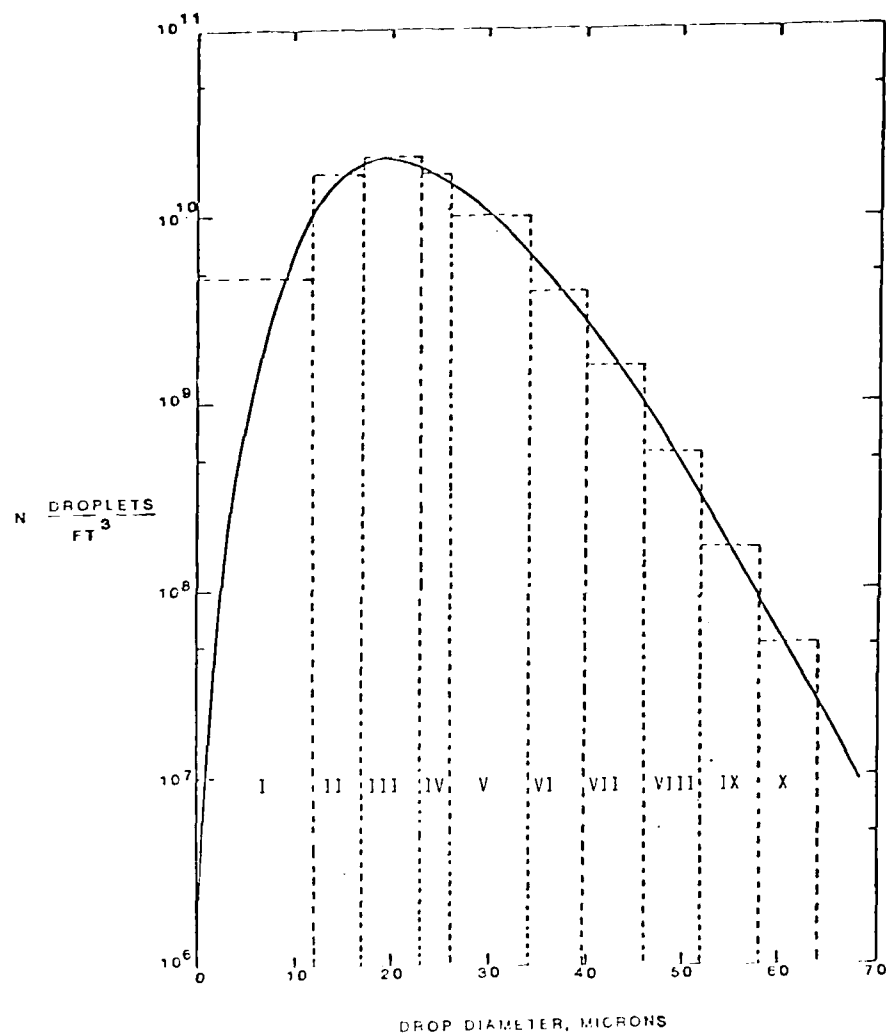


Figure 1. Initial Droplet Size Distribution and Discretized Approximation. Roman numerals indicate droplet class.

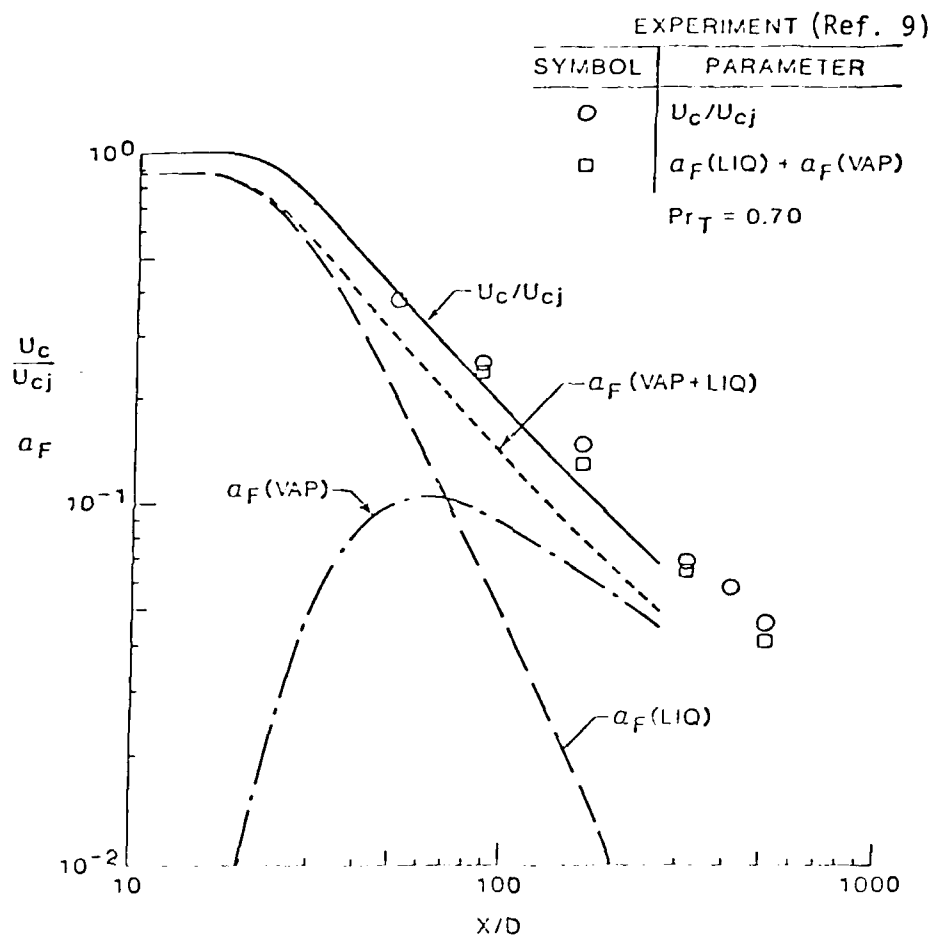


Figure 2. Axial Variation of Centerline Velocity and Species Mass Fractions, Vaporizing Spray Jet

but that the centerline Freon concentration (both liquid and vapor phase) is somewhat underpredicted. More accurate predictions of the centerline Freon concentration can be achieved by using a unity turbulent Prandtl number assumption, but results obtained with this assumption strongly underpredict the width of the concentration profile. As can be seen from Fig. 3, the present computations (at a turbulent Prandtl number of 0.70) provide very accurate predictions of the shape and width of the concentration profiles.

Radial profiles of mean axial velocity are also predicted very well by the vaporizing spray jet model, as shown by the results presented in Fig. 4. Note that, despite its two-phase nature, the vaporizing spray jet exhibits the profile similarity behavior expected of an axisymmetric single-phase jet into still air.

The analytical model described here provides, in addition to the mean profile results already discussed, a variety of information with respect to the development of the spray. For example, the evolution of the drop size distribution in the spray is an output of the computation, and results for this parameter are shown in Fig. 5. The drop size distribution evolution is shown here for the centerline and an r/x value of 0.10, which corresponds roughly to the half-radius of the spray jet. Of interest is the fact that as the number of droplets decreases, the distribution remains roughly the same, so that the SMD, for example, shows little change. The nearly vertical lines on Fig. 5 represent the average diameter for each class at each value of X/D ; the fact that they are nearly vertical indicates little change in mean diameter is occurring despite a nearly two-order-of-magnitude decrease in droplet number density. Thus the mean diameter of a spray distribution does not, from these results, appear to be a good indicator of the spray vaporization rate by itself.

Burning Spray

Mao, et al. (Ref. 10) report results for a spray diffusion flame. The experimental apparatus and measurement techniques used are quite similar to those used in the vaporizing spray study of Shearer, et al. already dis-

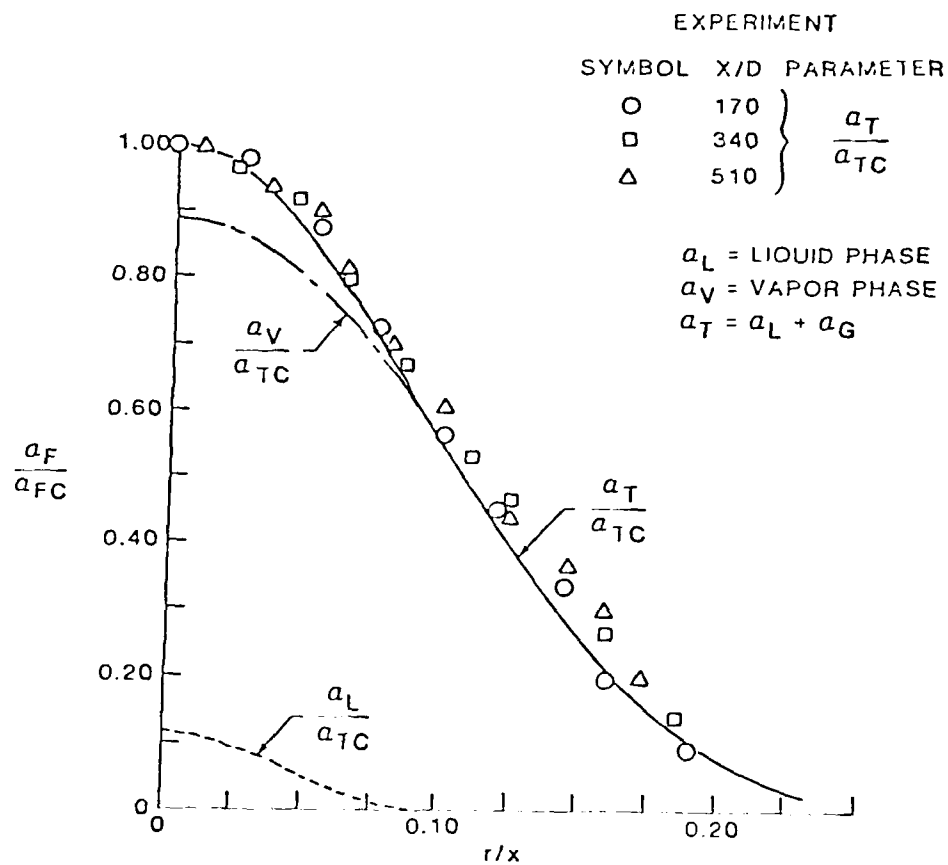


Figure 3. Radial Variation of Freon Concentration
Vaporizing Spray Jet. Data from Ref. 9
Model Predictions at $X/D = 235$

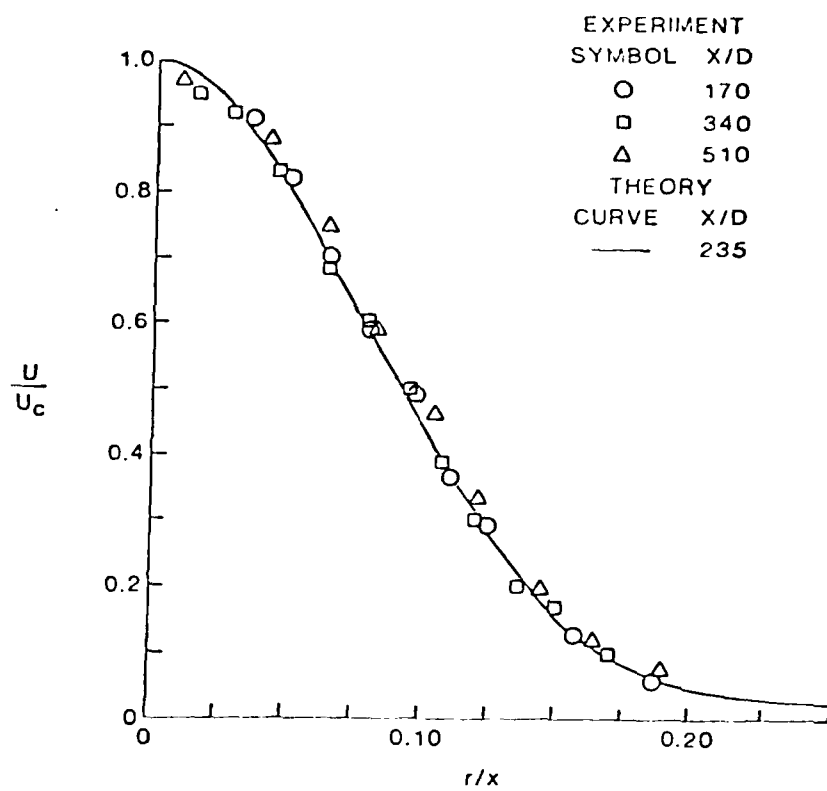


Figure 4. Radial Variation of Axial Velocity, Vaporizing Spray Jet. Data from Ref. 9

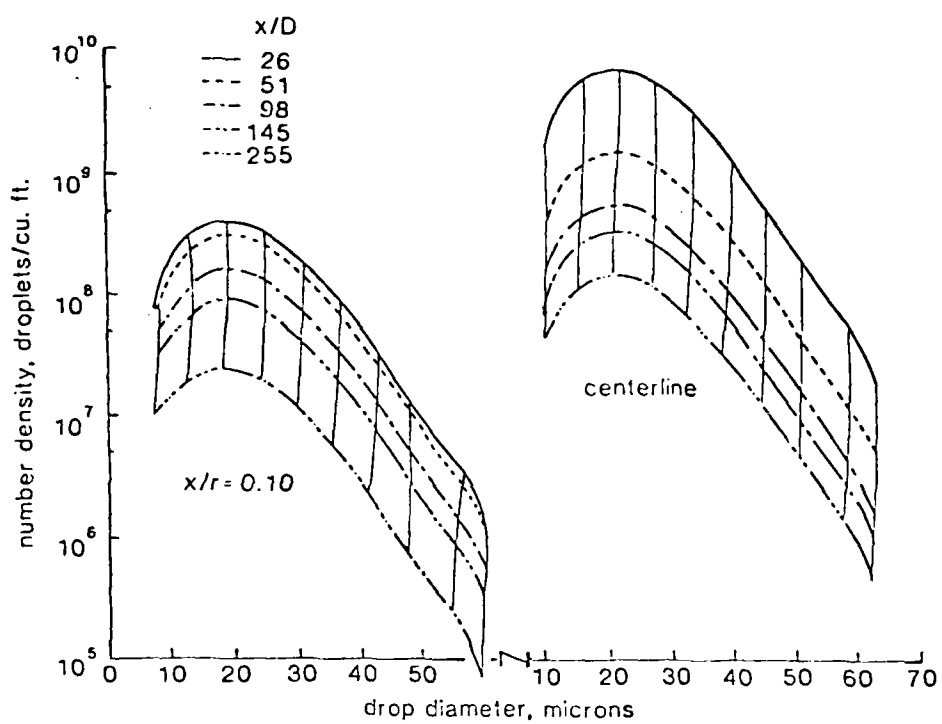


Figure 5. Computed Evolution of Droplet Size Distribution, Vaporizing Spray Jet

cussed. For the spray flame experiments, Mao et al. utilized n-pentane as a fuel, with an initial droplet distribution having a SMD of $35\text{ }\mu\text{m}$. Measurements include centerline velocity, fuel species, and temperature distributions, as well as radial profiles of velocity and temperature. Analysis of these data using the locally-homogeneous-flow (LHF) approximation is also reported in Ref. 10.

The calculations carried out using the spray flame model described in this report were initiated using a droplet distribution similar to that used for the nonburning spray, but adjusted to yield an SMD of $35\text{ }\mu\text{m}$. Initiation of the flame in the calculations is provided by the droplet flame sheet assumption: since an air-atomizing nozzle was used sufficient oxygen is available at the injector exit to initiate chemical reaction. This is an artifice, but it does provide an appropriate flame initiation zone to begin the computations. This initial reaction quickly exhausts the available oxygen, so that the bulk of the droplets vaporize in a hot fuel rich region in the interior of the flame. The fact that in the computations the bulk of the droplets do not enter directly into the combustion process is fully supported by experimental observations made by Mao et al. Gas phase combustion is described in the model using the advanced quasiglobal approach described in the preceding section, and gas phase thermal radiation is also included. This latter phenomenon was found to strongly affect the development of the flame, as described below.

A comparison of predicted centerline temperature with the temperature experimentally measured in the pentane spray flame is shown in Fig. 6. The overall profile shape is very well predicted, particularly for $X/D > 200$, but the predicted temperature is everywhere higher than that measured. Here radiation may play a role, both in the model and in the experiment. For $X/D < 200$, the predicted temperature is substantially in excess of that measured. In these calculations, the droplets vaporized by $X/D = 100$, whereas experimental observations of droplets to 150 diameters were reported. This suggests that the computed droplet vaporization rate is too high, and that the flame sheet model for droplet consumption on the edge of the flame is an oversimplification. Nevertheless, noting that there is no normalization in this comparison (other than division of the axial distance by the physical jet diameter), these results are very encouraging.

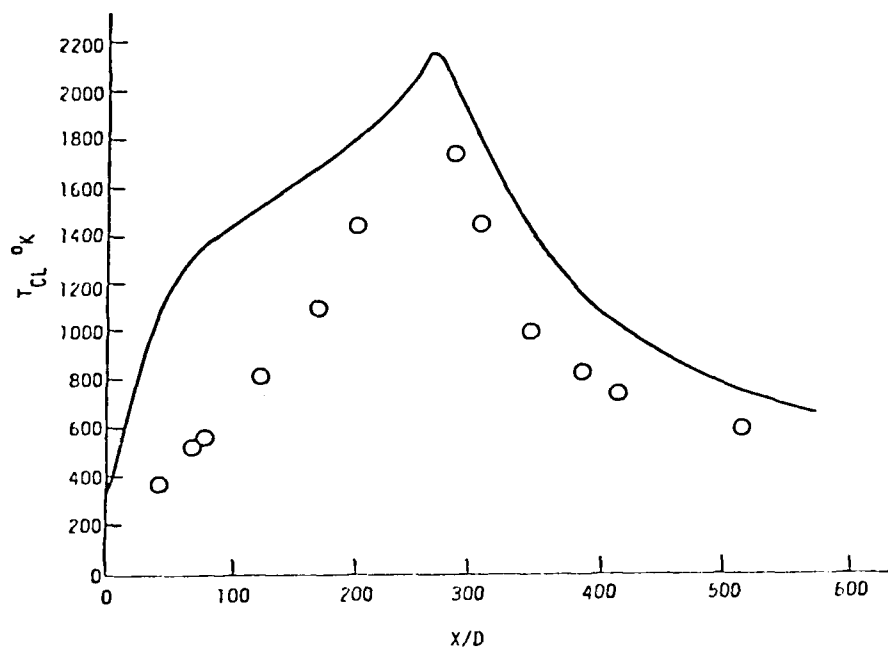


Figure 6. Comparison of Computed Centerline Temperature with Experimental Data, Pentaine Spray Flame. Data from Ref. 10

Both thermal radiation and buoyancy effects had to be included in the computational model in order to achieve a reasonable representation of the spray flame development. A number of parametric computations were carried out during the development of the approach, the results of which illustrate the effects of the neglect of these important phenomena. For example, the results shown in Fig. 7 indicate centerline temperature distributions obtained without including the effects of buoyancy, but with and without incorporation of the effects of gas-phase thermal radiation. The measured centerline temperature peaks at a value of some 1800°K. Without incorporating the effects of gas-phase thermal radiation, the predicted centerline temperature continues to increase, eventually reaching the adiabatic flame temperature for stoichiometric pentane-air combustion. Incorporating radiation losses, the model prediction of centerline temperature is much reduced with, in this case, a predicted temperature peak of only 1550°K.

Buoyancy influences both the mean flow and turbulence structure in the spray flame, and the relative effects of buoyancy increase as the magnitude of the buoyancy-induced body force term in the momentum equation increases relative to the momentum flow per unit area term. Since in a jet-into-still-air the local momentum flow per unit area is continuously decreasing with axial distance, at the same time as the temperature and therefore body force term increases, buoyancy effects can be expected to always exert some influence on the development of a spray flame in a quiescent ambient. The magnitude of this influence is illustrated by the results shown as Fig. 8, which presents computed centerline temperatures obtained including the effects of gas-phase thermal radiation, but with and without incorporation of the effects of buoyancy as the mean flow. Note that these results do not include the influence of buoyancy effects on the turbulent mixing rate. The results shown in Fig. 8 show that there are very large effects of buoyancy in this spray flame structure, since with mean-flow buoyancy effects included the calculation represents the shape of the centerline temperature profile quite well, particularly with respect to the rapid decay of centerline temperature downstream of the location of the temperature. However, the effects of incorporation of mean flow buoyancy without incorporating the corresponding buoyancy-turbulence structure effects produce a quite

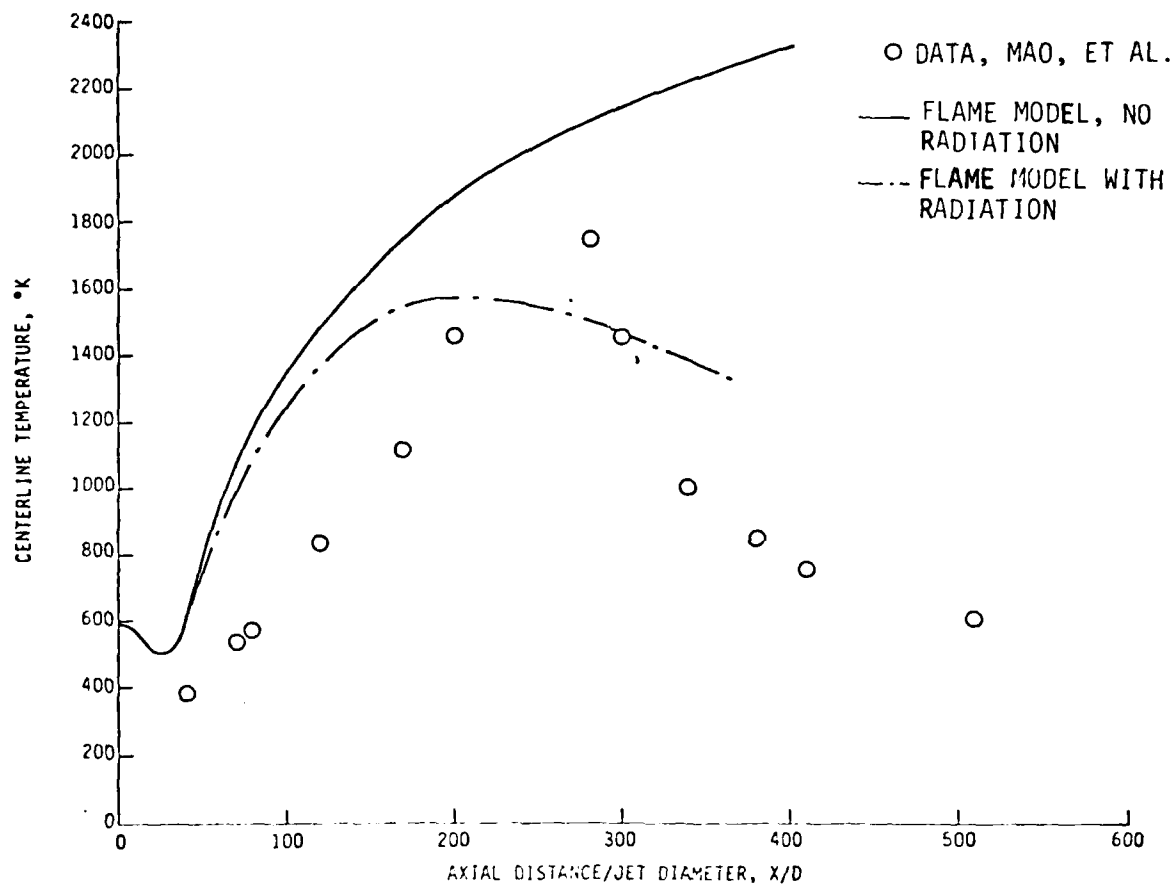


Figure 7. Centerline Temperature Distribution Reacting n-Pentane Spray Jet, With and Without Gas-Phase Thermal Radiation. Effects of buoyancy neglected. Data from Ref. 10.

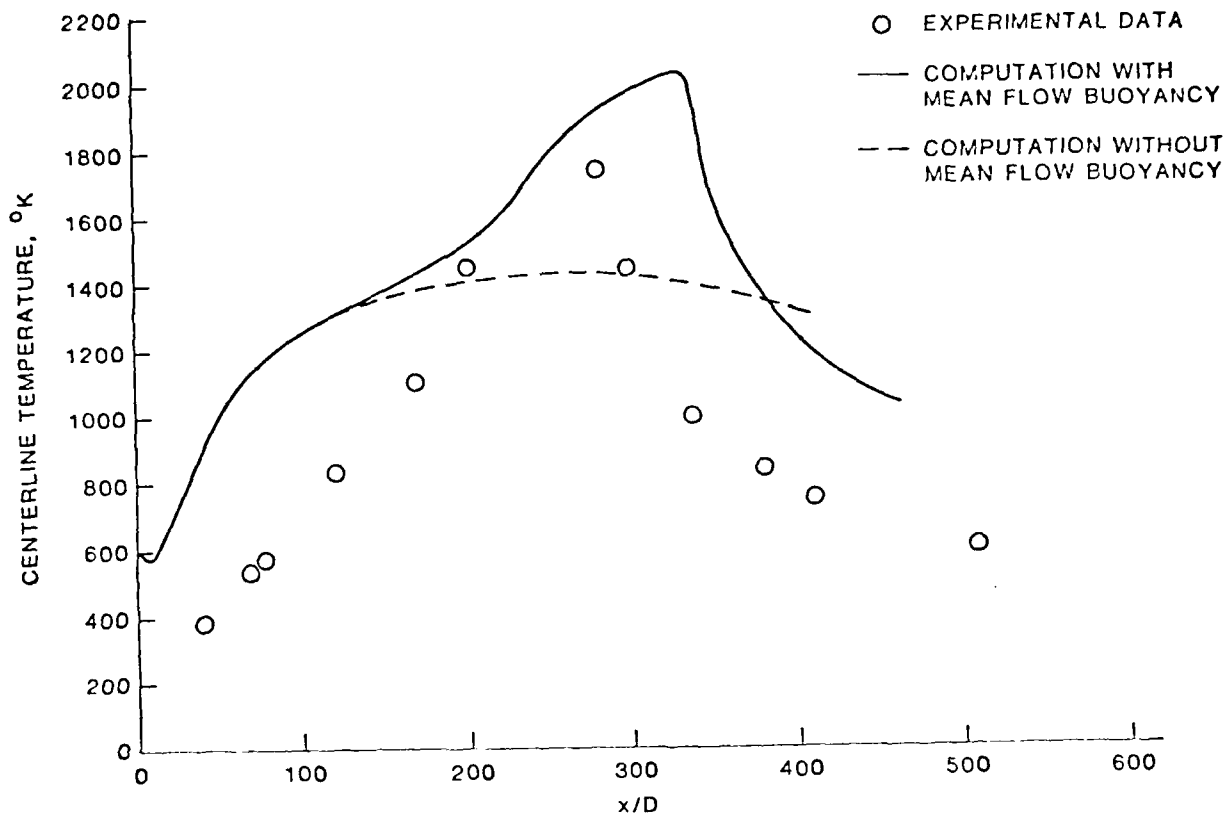


Figure 8. Effects of Neglect of Mean Flow Buoyancy in Predicted Centerline Temperature Distribution

different result when computed centerline velocity is compared with experimental data. This is demonstrated by the results shown in Fig. 9 where it can be seen that with mean-flow buoyancy, an increase in centerline velocity is observed for $100 < X/D < 300$. Clearly the data do not support this result. However, if the effects of buoyancy on the turbulent mixing process are included, through the buoyancy terms appearing in Equations (9) and (10), this centerline velocity increase phenomenon is to a large extent avoided. This result is shown by the centerline velocity variation results shown in Fig. 10, which correspond to the centerline temperature results of Fig. 6. These results show that the effects of buoyancy become apparent at around $X/D=200$, and result in a reduced rate of centerline velocity decay compared to the experimental data. The underprediction of the velocity decay rate is consistent with the overprediction of the centerline temperature, one effect of which would be to increase the magnitude of the buoyancy effect. Yet velocity profiles, Fig. 11, agree extremely well with the data for $X/D > 200$; these profiles, while normalized with the centerline velocity (as was the data) are not normalized with respect to the physical coordinate in a way that would mask disagreement. Indeed, the normalization used indicates that the computations correctly model the spread rate of the spray diffusion flame, at least for $X/D > 170$.

The accuracy of the spread rate prediction is also indirectly supported by comparison of the calculated and measured Reynolds stress component. This result, shown in Fig. 12, shows a very good level of agreement both in magnitude and location of the maximum shear stress. It has been established for single phase jets into quiescent ambients that the rate of spread of the jet is controlled by the peak shear stress levels encountered in the profile, so that the good level of agreement seen in Fig. 12 supports the velocity profile agreement displayed in Fig. 11.

Finally, computed and measured temperature profiles are compared in Fig. 13. Here it is evident that in the center of the flame the model predicts higher temperatures than are experimentally observed. Again, both droplet vaporization rate and gas phase radiation submodels are implicated in this disagreement. Other factors may enter as well. For example,

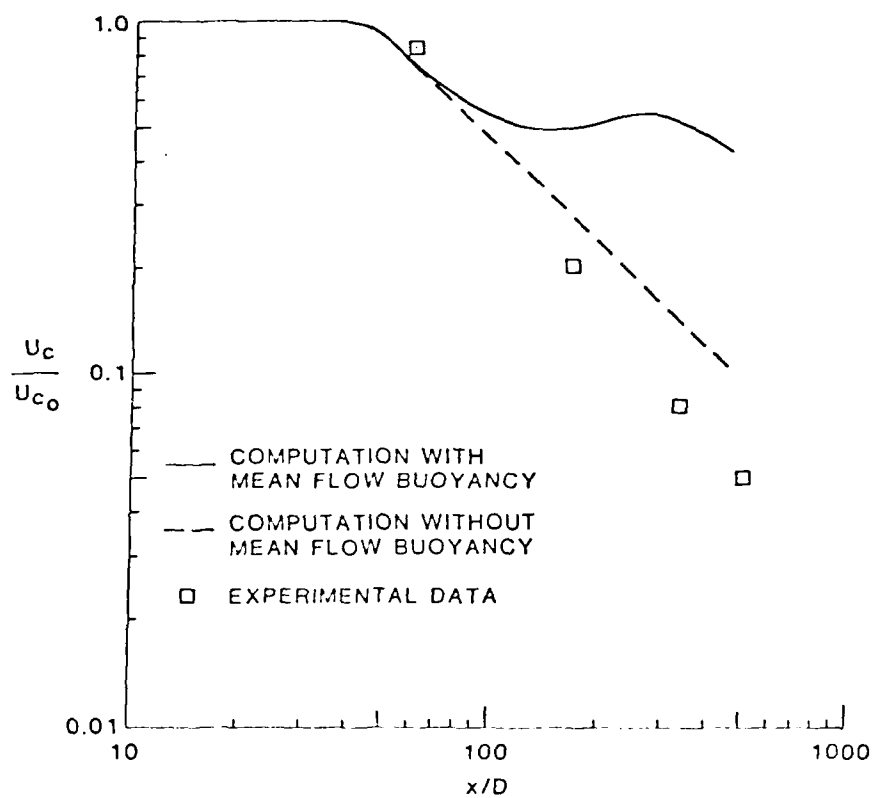


Figure 9. Effects of Mean Flow Buoyancy on Centerline Velocity Distribution, Reaching n-Pentane Flame. Data from Ref. 10

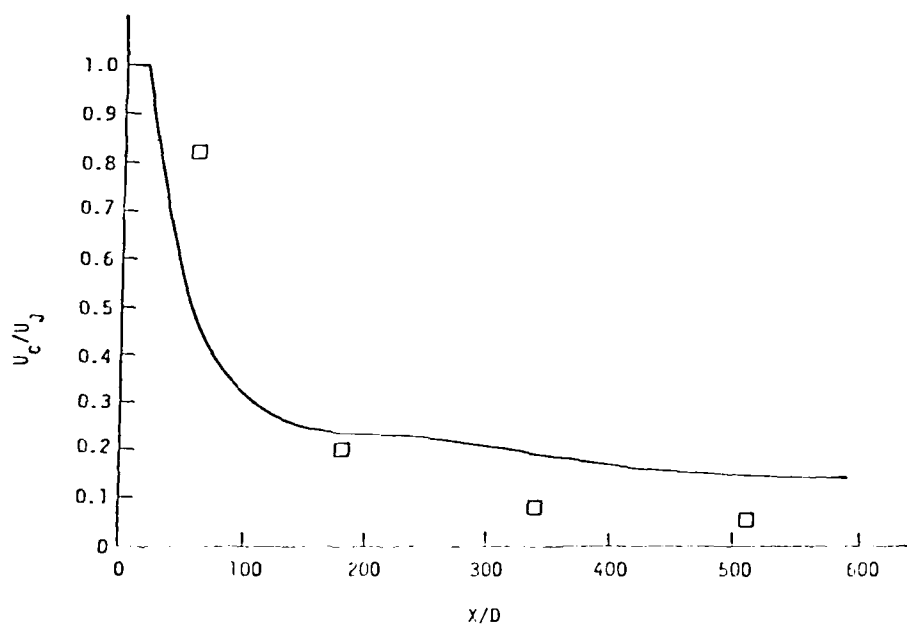


Figure 10. Comparison of Computed and Measured Centerline Velocities, n-Pentane Spray Flame. Calculation includes gas-phase thermal radiation, mean-flow and turbulence structure buoyancy effects. Data from Ref. 10.

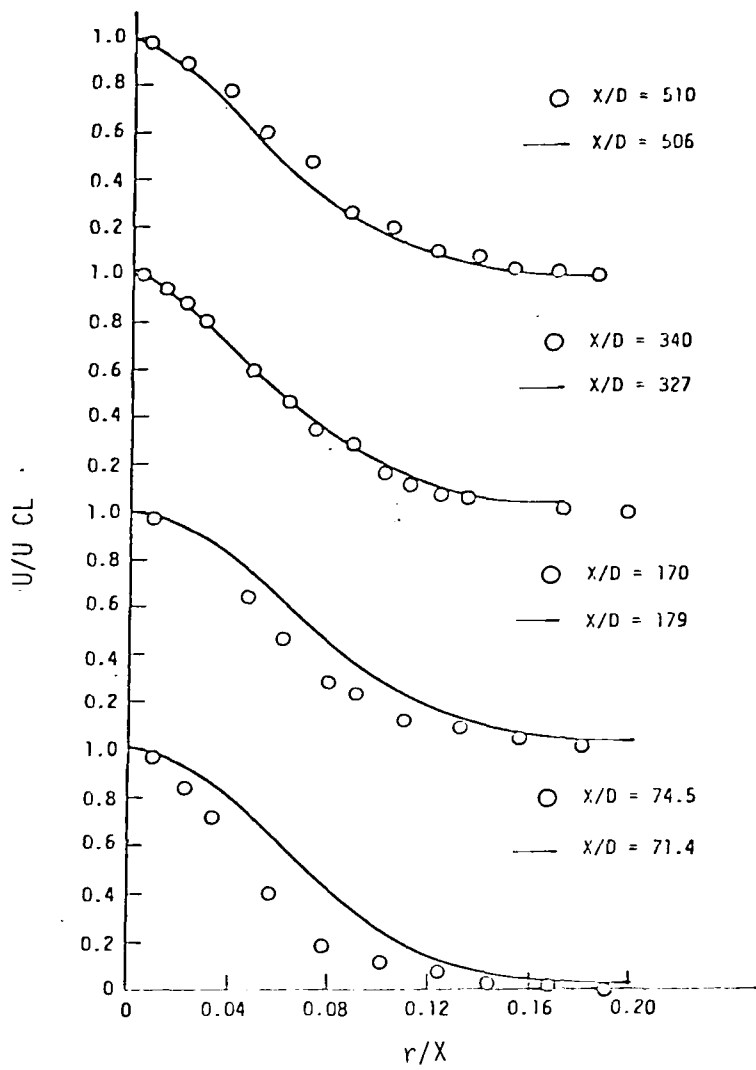


Figure 11. Radial Velocity Profile Comparison, n-Pentane Spray Flame. Calculation includes gas-phase thermal radiation, mean-flow and turbulence structure buoyancy effects. Data from Ref. 10

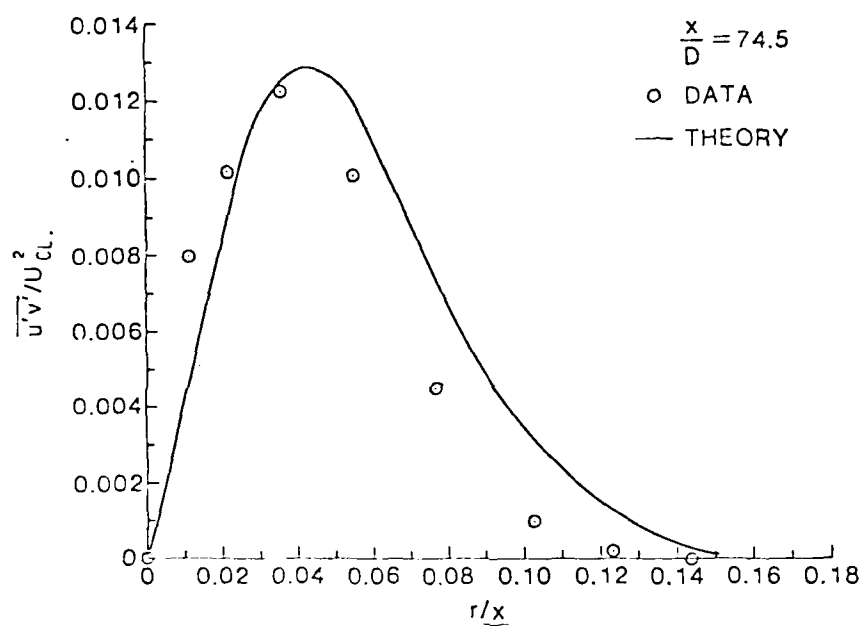


Figure 12. Reynolds Stress Profile, Reacting
n-Pentane Jet

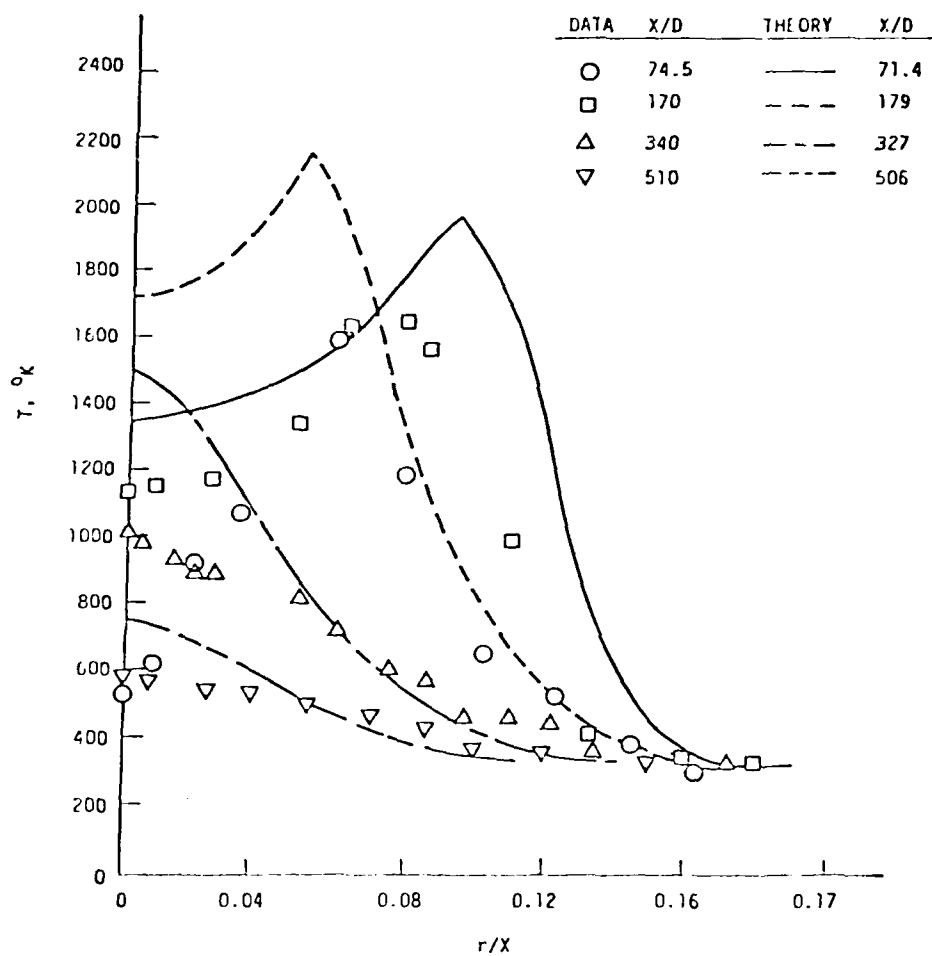


Figure 13. Comparison of Computed and Measured Temperature Profiles, Pentane Spray Flame

although the flow has been treated as fully turbulent, in both the original experiment documentation and in this work, it may have actually involved a laminar or transitional flow in the first 100 diameters or so. If this were the case, a slower rate of mixing than predicted herein would have existed, resulting in lower centerline temperature than predicted by this fully turbulent model.

2.1.3 Discussion

In assessing the performance of the spray flame model just described, it is important to keep in mind the important effects of the the strong coupling inherent in a spray diffusion flame. For the particular flow-field considered this coupling includes not only the mixing and kinetics, but also the effects of phase change, radiation, and buoyancy. Taking just one of these as an example, the effects of inclusion of thermal radiation were found to be significant in these calculations, accounting for centerline temperature differences ranging from 400°K to 1000°K. This level of temperature difference is significant with respect both to chemical kinetic and buoyancy effects. The buoyancy model is also worth noting, since results of additional computations clearly showed that neglecting the influence of buoyancy on the turbulent structure produced erroneous results. Thus, while attention in assessing the performance of this model may be focused on the use of the near dynamic equilibrium hypothesis, it is not altogether clear that this hypothesis exerts a dominant effect on the overall results.

Overall, the approach described in this paper provides a reasonably valid picture of the development of a spray diffusion flame. Moreover, it provides a computational tool which can usefully be applied to the parametric examination of the many physical and chemical interactions that underlie spray flame phenomena, both from a purely theoretical standpoint and in conjunction with detailed spray flame measurements. The approach also provides the basis for further development, for example through relaxation of

the limitation to near dynamic equilibrium in the spray transport process. Clearly, the model is complex, and involves a great variety of phenomena. But spray diffusion flames are themselves complex, and careful theoretical and experimental study is required to determine where model simplification may justifiably be made.

From a computational standpoint the complexity of the model is actually more apparent than real. Even with detailed finite-rate chemistry as described by the quasiglobal kinetics model, computation of the n-pentane spray flame considered here, carried out to an axial distance of 500 nozzle diameters, requires only about 30 minutes of CPU time on a CDC 7600. Computational times on more advanced computers can be expected to be considerably less. What the model provides for the investment in computer time is substantial detail with respect to the general structure of the spray flame flow field. For example, detailed temperature contours in the spray flame can be presented to illustrate the structure of the flame, as in Fig. 14. When compared with droplet distributions, as shown in terms of total mass fraction in liquid form on Fig. 15, conclusions can be drawn as to the mechanisms which the modeling indicates will dominate in the flame structure. Comparison of Figs. 14 and 15 shows that the bulk of the droplets are found in regions on the flame in which local temperature is greater than 800°K, but below 1200°K. Comparison with gas-phase oxygen profiles shows that this is a very fuel-rich region. Thus, except for an initial short region near the nozzle exit where temperatures range from 1600°K to 2000°K (and which is an artifice of the assumption that droplets burn, rather than vaporize, if $\alpha_{O_2} > 0.001$), vaporization is the primary mechanism responsible for the reduction in liquid-phase mass fraction. Combustion occurs only in a narrow region surrounding the droplet cloud, and for $X/D < 80$, is a low-temperature, fuel-rich process involving the mechanisms of pure and oxidative pyrolysis. Beyond $X/D \sim 80$, the liquid-phase mass fraction drops below 0.05 and there is a sudden and rapid increase in the reaction rate as indicated by the widening of the predicted flame shape seen on Fig. 14. This behavior is qualitatively in agreement with that observed experimentally, although these predictions indicate its occurrence rather sooner in the spray flame development than was otherwise observed.

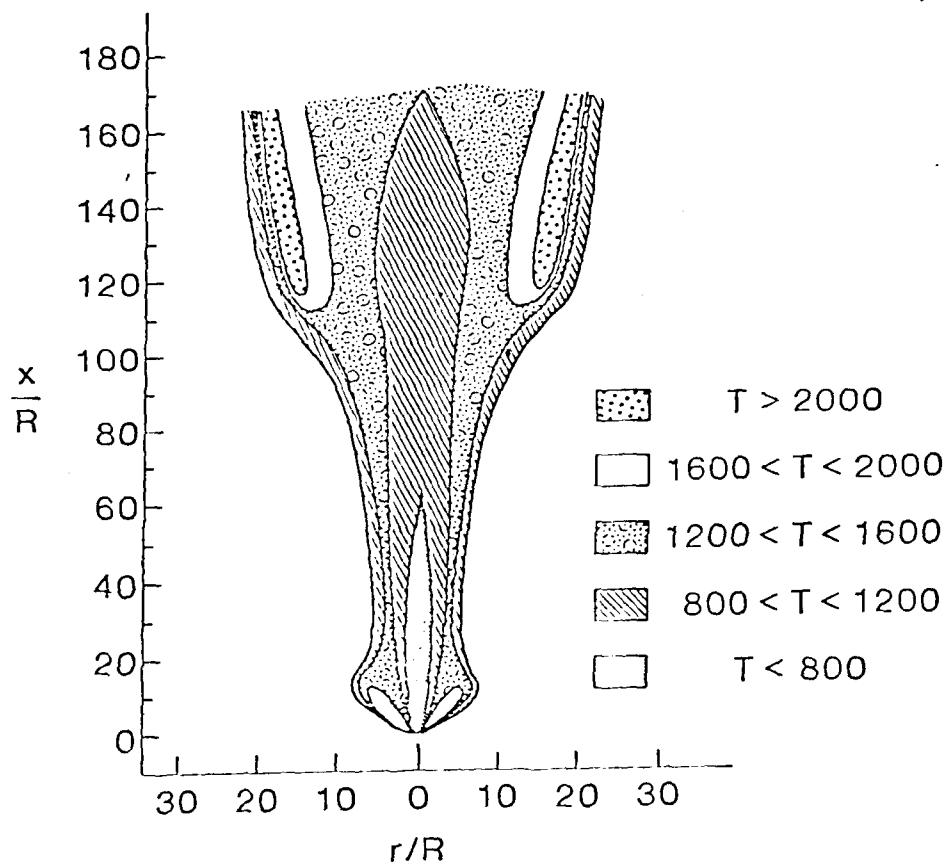


Figure 14. Temperature Contours in Initial Spray Flame Region

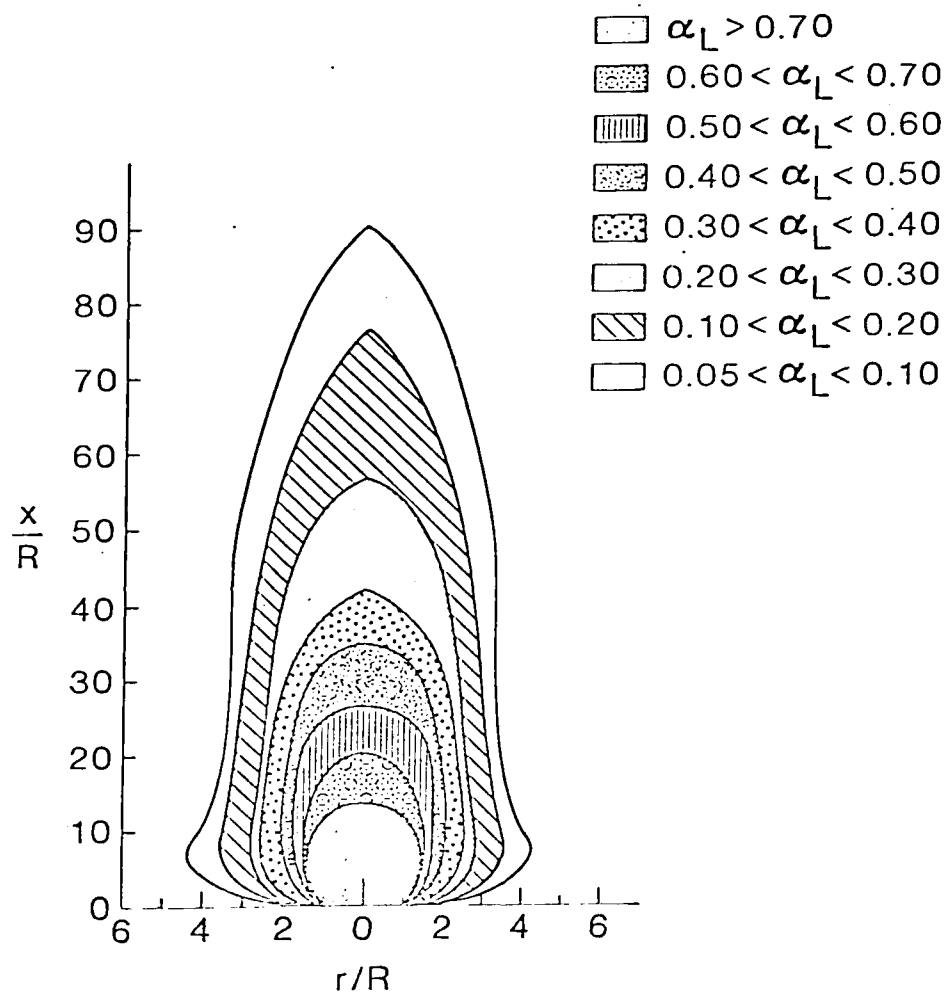


Figure 15. Droplet Total Mass Fraction (all classes)
Contours, Initial Spray Flame Region

It should also be noted that the particular experimental configuration selected for study in this work was not ideal from the standpoint of modeling complexity. In particular, the quiescent ambient introduces larger effects of buoyancy than would be the case in a coflowing situation. Indeed, it is possible to design an experiment which satisfies the assumptions of the analysis much more closely than that considered here, for example, with respect to the near-dynamic equilibrium assumption, while at the same time reducing the magnitude of the buoyancy effects. By doing this, and carefully comparing the experimental results with analytical predictions it would be possible to considerably enhance the characteristics of the multiphase spray flame model described in this work. By inference, then, questions of droplet-scale modeling, droplet-droplet and turbulence interaction could all be addressed in a step-by-step manner.

Finally, the results presented here are, in terms of level of agreement with the data, substantially similar to those reported in Ref. 10. The results described in Ref. 10 were obtained using a model which ignores two-phase flow effects, finite-rate vaporization, finite-rate gas phase kinetics, gas-phase thermal radiation, and buoyancy phenomena. Instead, the model utilized in Ref. 10 incorporates a turbulence-chemistry interaction model based on an assumed probability distribution function approach. Two-phase flow, finite-rate vaporization, finite-rate gas phase kinetics, gas-phase thermal radiation, and buoyancy are all physically real phenomena, and the parametric investigation reported above indicate the magnitude of their effects. Thus, the agreement with experiment of a theoretical treatment that ignores each of these phenomena in succession requires further explanation.

2.2 MODELING OF BORON COMBUSTION PROCESSES

Boron slurry fuel combustion is a complex phenomenon involving two-phase flow and finite-rate reaction processes in the gas phase and in the particle surface. In a slurry fuel, the boron is generally in the form of micron-sized particles suspended in a carrier hydrocarbon. As the hydrocarbon carrier burns, the boron is heated to the ignition temperature, and

it then subsequently burns with exposure to sufficient oxygen. One of the difficulties encountered in boron combustion is that a surface oxide layer can form on the particle. This oxide has a boiling point below that of the metal, so that the boron combustion process involves a diffusion of oxidizing gases through the liquid oxide layer with a surface reaction taking place at the particle/liquid interface. Since this is a slow process, one strategy for obtaining high boron combustion efficiencies is to limit the amount of oxygen reaching the surface of the particle during the heat-up process; i.e., carrying out the particle heatup in a regime which is fuel-rich relative to the hydrocarbon carrier, and then exposing the hot particles and remaining fuel to additional air. This form of staged combustion is difficult to achieve in practice, and the development of boron slurry fueled combustors could be materially aided by the availability of analytical design tools. The modular model described in the next section of this report provides the framework for the type of design tool that could be used for this purpose, but its extension to the analysis of boron slurry combustion requires the development of submodels of the boron combustion process. These submodels are the principal focus of the work carried out under this portion of the AFOSR-sponsored research at SAI.

2.2.1 Boron Combustion Models

Single-particle boron ignition and combustion models have been reported by King (Refs. 11, 12), Meese and Skifstad (Ref. 13), Vovchuck et al. (Ref. 14), Mohan and Williams (Ref. 15) and Edelman, et al. (Refs. 16, 17). The component equations that make up each of these models are summarized in Table 3, which also includes a review of the assumptions built into each of the models. The nomenclature for Table 3 is given in Table 4. In general, these formulations are based on the assumption of a spherical particle (except for the work of Mohan and Williams) and on the conservation equations for mass and energy. The momentum equation is not explicitly coupled into the equation set, but in certain of the models the relative velocity effect is accounted for through a Nusselt number correction on heat

TABLE 4. SUMMARY OF AVAILABLE BORON IGNITION AND COMBUSTION MODELS

COMPLETE HEAT TRANSFER EQUATIONS	$\left(\frac{4}{3} \pi r_p^2 \rho_B c_{PB(S \text{ or } L)} + 4 \pi r_p^2 \lambda \rho_{B_2O_3} c_{PB_2O_3} \right) \frac{dT_p}{dt} = \rho_B (C_{RX}) - \rho_L (\Delta H_{VAP}) - \rho_H \Delta H_H + 4 \pi (r_p + x)^2 [h (T_\infty - T_p) + \sigma \epsilon c_R (T_{RAD}^* - T_p^*)]$	King
	$(\rho_B c_{PB} + \rho_{B_2O_3} c_{PB_2O_3}) \frac{dT_p}{dt} = RQ - \rho_L \Delta H_{VAP} + 4 \pi r_p^2 [h (T_g - T_p) + \sigma \epsilon c_R (T_{RAD}^* - T_p^*)]$	Meese
	$-4 \pi \lambda r^2 \frac{dT}{dr} = I_{O_2} H_{O_2}(T) + I_B H_B(T_k) - I_{B_2} H_{B_2O_3}(T) - Q_R^K$	Vovchuk
	$h \rho_C c_C \frac{dT_C}{dt} = q_B \rho_B \rho_B - q_C \rho_C \rho_C - L$	Mohan
	$\frac{dT_p}{dt} = \frac{3}{2} \frac{\pi \lambda (Nu)}{\delta_s c_{ps} R^2 c_p} \cdot \left\{ \frac{c_p (T_g - T_p)}{e^{\theta} - 1} - L + A k_s \left[\frac{2 c_p \rho_s R}{\delta \lambda (Nu) y_{O_2,s}} \right] + \frac{H_B}{H_{O_2}} \Delta H_R - \frac{2 \sigma \epsilon R c_p}{\delta \lambda (Nu)} (T_p^* - T_w^*) \right\}$	Edelstein
HEAT TRANSFER: CONDUCTION-CONVECTION COMPONENTS	① $\left(\frac{4}{3} \pi r_p^2 \rho_B c_{PBS} + 4 \pi r_p^2 \lambda \rho_{B_2O_3} c_{PB_2O_3} \right) \frac{dT_p}{dt} = 4 \pi (r_p + x)^2 (T_\infty - T_p) h$ BELOW PHASE CHANGE OF BORON, $T_p < 2450$	King
	② $\left(\frac{4}{3} \pi r_p^2 \rho_B \Delta H_m \right) \frac{df}{dt} = 4 \pi (r_p + x)^2 (T_\infty - T_p) h$ AT PHASE CHANGE, $T_p = 2450, 0 < f < 1$	
	③ $\left(\frac{4}{3} \pi r_p^2 \rho_B c_{PBL} + 4 \pi r_p^2 \lambda \rho_{B_2O_3} c_{PB_2O_3} \right) \frac{dT_p}{dt} = 4 \pi (r_p + x)^2 (T_\infty - T_p) h$ ABOVE PHASE CHANGE, $T_p > 2450, f = 1$	
	$(\rho_B c_{PB} + \rho_{B_2O_3} c_{PB_2O_3}) \frac{dT_p}{dt} = 4 \pi r_p^2 h (T_g - T_p)$	Meese
	$h \rho_C c_C \frac{dT_C}{dt} = (T_C - T_\infty) \frac{2\lambda}{D}$	Mohan
HEAT TRANSFER: RADIATION	$\frac{4}{3} \pi k^2 \epsilon_s c_{ps} \frac{dT_p}{dt} = 4 \pi r_p^2 h (T_g - T_p) \frac{\sigma}{e^{\theta} - 1}$	Edelstein
	① $\left(\frac{4}{3} \pi r_p^2 \rho_B c_{PBS} + 4 \pi r_p^2 \lambda \rho_{B_2O_3} c_{PB_2O_3} \right) \frac{dT_p}{dt} = 4 \pi (r_p + x)^2 \sigma \epsilon c_R (T_{RAD}^* - T_p^*)$	King
	② $\left(\frac{4}{3} \pi r_p^2 \rho_B \Delta H_c \right) \frac{df}{dt} = 4 \pi (r_p + x)^2 \sigma \epsilon c_R (T_{RAD}^* - T_p^*)$	
	③ $\left(\frac{4}{3} \pi r_p^2 \rho_B c_{PBL} + 4 \pi r_p^2 \lambda \rho_{B_2O_3} c_{PB_2O_3} \right) \frac{dT_p}{dt} = 4 \pi (r_p + x)^2 \sigma \epsilon c_R (T_{RAD}^* - T_p^*)$	
	$(\rho_B c_{PB} + \rho_{B_2O_3} c_{PB_2O_3}) \frac{dT_p}{dt} = 4 \pi r_p^2 \sigma \epsilon c_R (T_{RAD}^* - T_p^*)$	Meese
	$-4 \pi \lambda r^2 \frac{dT}{dr} = -4 \pi r_k^2 \sigma \epsilon c_R (T_k^* - T_\infty^*)$	Vovchuk

TABLE 4. (Continued)

HEAT TRANSFER: RADIATION	$h p_c \epsilon_c \frac{dT_c}{dt} = -1.36 \epsilon \left(\frac{T_c}{1000} \right)^4$	Mohr
	$\frac{4}{3} \pi R^2 \epsilon_{ps} \delta_s \frac{dT_p}{dt} = -4 \pi R^2 \sigma \epsilon (T_p^4 - T_\infty^4)$	Edelman
OXIDE FORMATION	$B(s, l) + \frac{3}{4} O_2(g) \rightarrow \frac{1}{2} B_2O_3(g)$ FAST REACTION DIFFUSION LIMITED HAPPENS AT OXIDE-BORDO INTERFACE	King
	$B(s, l) + \frac{3}{4} O_2(g) \rightarrow \frac{1}{2} B_2O_3(g)$ WORK BASED ON KING'S	Morse
	$2BO_2(g) \rightleftharpoons B_2O_3(g) + \frac{1}{2} O_2(g)$ THERMAL EQUILIBRIUM $B_2O_3(g) \rightleftharpoons 2BO(g) + \frac{1}{2} O_2(g)$ DIFFUSION CONTROLLED LOWER OXIDES ONLY AT SURFACE $B_2O_2(g) \rightleftharpoons 2BO(g)$	Vovchuk
	$B(s) + \frac{3}{4} O_2(g) \rightarrow \frac{1}{2} B_2O_3(l)$ DIFFUSION CONTROLLED EQUILIBRIUM VAPORIZATION OF B_2O_3 AND ABSORPTION OF O_2 IN THE LIQUID B_2O_3 AT LIQUID- GAS SURFACE.	Mohr
	$B(l) + \frac{1}{2} O_2(g) \rightarrow BO(g)$ FINITE-RATE KINETICS CONTROLLED $B(l) + \frac{3}{4} O_2(g) \rightarrow \frac{1}{2} B_2O_3(g)$	Edelman
OXIDE CONSUMPTION	$H_2O(g) + B_2O_3(l) \rightarrow 2HBO_2(g)$ DIFFUSION LIMITED ENDOTHERMIC REACTION RATE CONTROLLED EVAPORATION	King
	$H_2O(g) + B_2O_3(l) \rightarrow 2HBO_2(g)$ WORK BASED ON KING'S	Morse
DIFFUSION THROUGH GAS FILM RATES AND CONSTANTS	DIFFUSIVITY OF B_2O_3 , HBO_2 , H_2O GAS THROUGH N_2 FILM; J - ONE OF: B_2O_3 , HBO_2 , H_2O $D_{J, N_2} = 4.3 \cdot 10^{-8} \frac{T_p^{1.75}}{P (V_{J, N_2}^{1/2} + V_{N_2}^{1/2})} \sqrt{\frac{1}{(M_J)_{N_2}} + \frac{1}{(M_{N_2})_J}}$ $\frac{R_H}{4 \pi (r_p + x)^2} = \frac{D_{H_2O, N_2} Nu}{2 (r_p + x) R T_p} (P_{H_2O, \infty} - P_{H_2O, SURF})$ $\frac{R_H}{4 \pi (r_p + x)^2} = \frac{D_{HBO_2, N_2} Nu}{4 (r_p + x) R T_p} (P_{HBO_2, SURF})$ POLAR REMOVAL RATE OF OXIDE BY WATER	King
	WORK BASED ON KING'S	Morse
	$I_{O_2} = -4 \pi r^2 \frac{D}{RT} \frac{dP_{O_2}}{dr}; I_{BO} = -4 \pi r^2 \frac{D}{RT} \frac{dP_{BO}}{dr}$ ETC. B_2O_2 , B_2O_3 , BO_2	Vovchuk
	$R_c = 2 X_a D_a p_a / p_c d$ OUTWARD GAS-PHASE DIFFUSION OF B_2O_3 $R_B = R_c = (q_c p_c R_c + L) / q_b p_b$ AT LOW TEMP. STAGE KINETICALLY CONTROLLED	Mohr Edelman

TABLE 4. (Continued)

DIFFUSION THROUGH OXIDE LAYER	$R_B = \frac{4 + (r_p + x)^2 k_1 e^{-1/T_p} (P_{O_2}) T_p}{x}$ <p>MOLAR CONSUMPTION RATE OF BORON</p> $R_B = \frac{64.8 \cdot 10^{-8} (r_p + x)^2 T_p e^{-11500/T_p} (P_{O_2, SURF})}{x}$ <p>$\frac{3}{4} O_2$ to 1 B</p>	King
	$R = \frac{1}{\Delta r} \frac{2.0 \cdot 10^{-8} r_2^2 T_p P_{O_2} \exp(-11500/T_p)}{\text{ONLY CHANGE FROM KING'S}}$	Morse
	NO OXIDE LAYER	Vovchuk
	$R_B = x k D / h$	Mohen
	NO OXIDE LAYER	Edelman
PHASE CHANGE BORON	$\frac{df}{dB} = z \text{ of } B(z) = \frac{\{R_B(O_{RX}) - R_L(\Delta H_{VAP}) - P_H \Delta H_H + 4\pi(r_p + x)^2 \cdot [h(T_\infty - T_p) + \sigma \epsilon \alpha_r (T_{RAD}^* - T_p^*)]\}}{\frac{4}{3} \pi r_p^3 \rho_B \Delta H_B}$	King
	$\Delta H_f \frac{m_B}{M_B} \int_0^{T_m} dt \left\{ RQ - R_L \Delta H_{VAP} + 4\pi r_1^2 [h(T_\infty - T_p) + \sigma \epsilon (T_{RAD}^* - T_p^*)] \right\}$	Morse
	$\dot{r}_T = \frac{4\pi R^2 \alpha}{\sqrt{2\pi} M_B R_o T_p} [P_{v,B}(T_p) - P_{B,S}]$	Edelman
PHASE CHANGE OXIDE	$P_E = \frac{1.005 \cdot 10^{13} (r_p + x)^2 \alpha e^{-11500/T_p}}{T_p^2 \left\{ 1 + [(4.5 \cdot 10^7) \alpha P (r_p + x) / T_p (Nu)] \right\}}$ <p>MOLAR EVAPORATION RATE OF B_2O_3</p>	King
	$P_E = 1.225 \cdot 10^6 r_2^2 \exp(-42000/T_p)$	Morse
	NO OXIDE LAYER	Vovchuk
	$\frac{R_C}{R_V} = 2 D_8 / d C \alpha$ <p>LIMITED DEPENDING ON α</p>	Mohen
	NO OXIDE LAYER	Edelman
CHEMISTRY	$H_2O(g) + B_2O_3(z) \rightleftharpoons 2HBO_2(g) \quad B(s, z) + \frac{3}{4} O_2(g) \rightleftharpoons \frac{1}{2} B_2O_3(g)$	King
	$H_2O(g) + B_2O_3(z) \rightleftharpoons 2HBO_2(g) \quad B(s, z) + \frac{3}{4} O_2(g) \rightleftharpoons \frac{1}{2} B_2O_3(z, g)$	Morse
	$2B_2O_2(g) \rightleftharpoons B_2O_3(g) + \frac{1}{2} O_2(g)$	Vovchuk
	$B_2O_3(g) \rightleftharpoons 2BO(g) + \frac{1}{2} O_2(g)$	
	$B_2O_2(g) \rightleftharpoons 2BO(g)$	Mohen
	$B(s) + \frac{3}{4} O_2(g) \rightleftharpoons \frac{1}{2} B_2O_3(z) \quad B_2O_2(g) + \frac{1}{2} O_2(g) \rightleftharpoons B_2O_3(g)$	
CHEMICAL KINETICS	$B(s) + \frac{1}{2} O_2(g) \rightleftharpoons BO(g) \quad B(s) + \frac{3}{4} O_2(g) \rightleftharpoons B_2O_3(g)$	Edelman
	$k_c = A k_s \frac{M_B}{M_{O_2}} r_s y_{O_2, s} \left(\frac{R C_{FS}}{h \sqrt{2}} \right)$	Edelman

TABLE 4. (Continued)

SPECIES FOUND AT THE SURFACE	$H_2O(g), HBO_2(g), O_2(g), B_2O_3(l,g), B(s,l), H_2(g)$	King
	$H_2O(g), HBO_2(g), O_2(g), B_2O_3(l,g), B(s,l), H_2(g)$	Morse
	$B(s,l), BO(g), BO_2(g), B_2O_2(g), B_2O_3(g), O_2(g)$	Vovchuk
	$B(s), B_2O_2(g), O_2(g), B_2O_3(l,g)$	Mohan
	$B(s,l), B_2O_2(g), O_2(g), H_2(g), BO(g)$	Edelman
SPECIES FOUND OFF SURFACE (GASES)	$HBO_2, B_2O_3, O_2, H_2O, H_2$	King
	$HBO_2, B_2O_3, O_2, H_2O, H_2$	Morse
	B_2O_3, B_2O_2, O_2	Vovchuk
	B_2O_3, H_2, O_2	Mohan
	B_2O_3, O_2, H_2, BO	Edelman
NUSSELT NUMBER	SET EQUAL TO 2.0	King
	$(1 + 0.296 Fr^{1/2} Re^{1/2}) = Nu$ BASED ON RADIUS	Morse
	$Nu = 2 + 0.276 Fr^{1/2} Re^{1/2}$ $Pr = \frac{c_p v_g}{\lambda} \quad Re = \frac{2 R \rho_g (v_g - v_p)}{\mu_g}$	Edelman
BURNING TIMES	BOIL-OFF TIME OF OXIDE LAYER $t_B = \frac{\rho_{B_2O_3} (r_2^3 - r_1^3) \Delta H_{VAP}}{3 r_2^2 (R/A) Q + h(T_g - T_p) + \alpha \alpha c (T_{RAD}^4 - T_p^4) \rho_{B_2O_3}}$	Morse
	$t_c = \frac{r_B d_{kO}^2}{16 \nu_B \frac{D}{RT} \rho_{O_2}}$ DROPLET COMBUSTION TIME $t_r = \frac{r_B d_{kO}^2}{8 \nu_B \frac{V_B}{V_{O_2}} \frac{P}{R} \frac{D}{T} \left(1 - \frac{1}{V_{E_2O_3}} \right) \left[\ln \left[P - (1 - V_{E_2O_3}/V_{O_2}) \rho_{O_2} \right] \right]}$	Vovchuk
	$t_B = \frac{c_F \rho_L d^3}{8 \lambda} \left\{ \ln \left[1 + \frac{Q_F + c_P (T_\infty - T_L)}{\lambda} \right] \right\}^{-1}$	Mohan
RADIUS CHANGE	$\frac{dr_p}{dt} = \frac{-R_B (M_B)_B}{4 \pi r_p^2 \rho_B} \quad \frac{dx}{dt} = \frac{(R_B/2 - R_E - F_H)(M_B)_B}{4 \pi r_p^2 \rho_{B_2O_3}}$	King
AND/OR	$\frac{dr_B}{dt} = -R_B \quad r_B = \frac{4}{3} \pi r_1^3 \rho_B \quad \frac{dr_{B_2O_3}}{dt} = (R/2 - R_E) \rho_{B_2O_3} \quad r_{B_2O_3} = \frac{4}{3} \pi (r_2^3 - r_1^3) \rho_{B_2O_3}$	Morse
OXIDE CHANGE	$\frac{dh}{dt} = R_B - R_C \quad F_B = X k D / n \quad R_C = 2 X_A D_A \rho_A / \rho_C d$	Mohan
	$\frac{d(R^2)}{dt} = -\frac{\lambda}{6 s} \frac{(Nu)}{c_p}$	Edelman

TABLE 4. (Continued)

EQUATION REFERENCES	η_B eq. includes: an Arrhenius viscosity-temperature law, $\eta = A e^{-E/RT}$ Henry's law, $P_1/X_1 = K_1$ Wille correlation, $D_{AB}^0 = 7.4 \cdot 10^{-8} \frac{(\phi m_B)^{1/2} T}{\eta_B V_A^{1/3}}$	King
	σ Stefan's constant = $5.669 \cdot 10^{-8} \text{ W/m}^2 \text{ } ^\circ\text{K}^{-4}$ = $0.1714 \cdot 10^{-8} \text{ BTU/h-ft}^2 \text{ } ^\circ\text{R}^{-4}$ $D = D_0 (T/T_0)^{1.75}$ $\lambda = \lambda_0 (T/T_0)^{0.75}$	Mc Hut
	$R_B = X K D / h$ $P_E = \exp (H/R^* T_B - H/R^* T_C)$ $K D$ can be expressed in an Arrhenius form (see King)	Mohan
	Clausius - Clapeyron $\frac{d \ln p_s}{dt} = \frac{L_s}{RT^2}$	Edelen
EQUATIONS FOR h	$h = 0.347 \cdot 10^{-4} (\text{Nu}) T_\infty^{-0.4} / (r_p + X)$ (1974) $h = 0.694 \cdot 10^{-4} T_\infty^{-0.4} / r_2$ (1972)	King
	$h = (1 + 0.296 \text{ Fr}^{1/2} \text{ Re}^{1/2}) k_g / r$	Morse
IGNITION	The first stage of a two stage burn. During this time the oxide layer is removed.	King
	A state at which no energy barriers stand between that state and steady-state combustion.	Morse
	Only considers combustion.	Vovchuk
	Similar to King's.	Mohan
	N/A	Edelen
ASSUMPTIONS	Oxide generation controlled by diffusion of oxygen through liquid oxide layer. Uniform particle temperature. Vaporization and diffusion considered as series resistances. H_2O removes Fe_2O_3 by diffusion limited reaction (endothermic). Heat gain/loss by convection, radiation. Partial pressure of H_2O negligible in the free stream. Particle is stationary with respect to surrounding gasses. Paper only deals with ignition.	King
	Initial Fe_2O_3 layer thickness is uniform. Uniform particle temperature. The convective heat transfer coefficient, h , is known. Surroundings treated as black at temperature T_{RAD} . Prior to oxide removal, boron reaction rate is diffusion controlled and forms Fe_2O_3 . Fe_2O_3 evaporation follows an Arrhenius type relation. Particle temperature remains constant during melting and boiling. Variation in h , surface reaction rate and oxide evaporation rate are neglected during oxide boiling. Water vapor reduces the activation energy of oxide evaporation. Initial particle temperature is below oxide boiling and boron melting. Fe_2O_3 formed during boiling may be neglected. No net radiative exchange between particle and cloud. Convective heat transfer neglected in final computations.	Morse
	The particle has been heated to equilibrium temperature. Reaction occurs at the surface. The diffusion coefficients for the oxidant and reaction products are identical. Radiation can be neglected to a first approximation ($d \leq 100 \mu\text{m}$). Particle temperature is above oxide boiling and boron melting points.	Vovchuk
	Diffusion controlled $\text{B} + 3/4 \text{ O}_2 \rightarrow 1/2 \text{ Fe}_2\text{O}_3$. Liquid layer is isothermal. Ideal gas. Absorptive equilibrium for O_2 at C and 1D steady-state diffusion of O_2 within liquid layer. Plane two-dimensional slab model.	Mohan
	No oxide layer. Uniform particle temperature. Surface combustion kinetics. Finite-rate evaporation of boron from the surface.	Edelen

TABLE 5. NOMENCLATURE FOR EXPRESSIONS SUMMARIZED
IN TABLE 3

5.1 KING'S MODEL

C_{PB1}	liquid boron heat capacity (cal/gm°K)
C_{PBS}	solid boron heat capacity (cal/gm°K)
$C_{PB_2O_2}$	liquid boron oxide heat capacity (cal/gm°K)
f	fraction of boron in the liquid phase
h	gas-particle heat transfer coefficient (cal/cm ² sec°K)
k	mass transfer coefficient for transport of boric oxide gas from particle to free-stream (gm-mol/cm ² atm sec)
$(MW)_B$	boron atomic weight (gm/gm-mol)
$(MW)_{B_2O_2}$	boric oxide molecular weight (gm/gm-mol)
Nu	Nusselt Number
P	total pressure (atm)
P_{O_2}	oxygen partial pressure in free stream (atm)
$P_{B_2O_3, \text{ surf}}$	boric oxide partial pressure adjacent to particle surface (atm)
$P_{B_2O_3}^o$	boric oxide vapor pressure (atm)
$P_{H_2O, \text{ surf}}$	water gas partial pressure adjacent to particle surface (atm)
$P_{HBO_2, \text{ surf}}$	HBO ₂ partial pressure adjacent to particle surface (atm)
$P_{B_2O_3, \infty}$	boric oxide partial pressure in free-stream (atm)
Q_{RX}	heat release of $B(s) + \frac{3}{4}O_2 + \frac{1}{2}B_2O_3(l)$ (cal/gm-mol)
Q_{RX2}	heat release of $B(l) + \frac{3}{4}O_2 + \frac{1}{2}B_2O_3(l)$ (cal/gm-mol)
R	gas law constant, 82.06 atm-cm ³ /gm-mol°K
R_B	molar rate of boron consumption (gm-mol/sec)
R_E	molar evaporation rate of boric oxide (gm-mol/sec)
R_H	molar rate of removal of B_2O_3 by water reaction (gm-mol/sec)
r_p	boron particle radius (cm)
T_∞	free stream gas temperature (°K)
T_{CL}	particle center temperature (°K)
T_p	particle temperature (°K)
T_{RAD}	surroundings radiation temperature (°K)
T_s	particle surface temperature (°K)
V_j	molecular volume of species j (cm ³)
x	oxide layer thickness (cm)
$D_{B_2O_3, N_2}$	diffusivity of gaseous boric oxide in nitrogen (cm ² /sec)
D_{HBO_2, N_2}	diffusivity of HBO ₂ in nitrogen (cm ² /sec)
D_{H_2O, N_2}	diffusivity of water gas in nitrogen (cm ² /sec)
ΔH_H	heat absorbed by reaction of H_2O with $B_2O_3(l)$ (cal/gm-mol)
ΔH_m	heat of fusion of boron (cal/gm)
ΔH_{VAP}	heat of vaporization of $B_2O_3(l)$ (cal/gm-mol)

TABLE 5. (Continued)

α	evaporation coefficient of boric oxide liquid
α_R	surroundings absorptivity
α_t	thermal diffusivity of boron (cm^2/sec)
σ	Stefan-Boltzmann constant, $1.354 \cdot 10^{12} \text{ cal/cm}^2 \text{ sec}^\circ\text{K}^4$
ϵ	particle emissivity
v	Hertz-Knudsen impingement factor ($\text{gm-mol/cm}^2 \text{ atm sec}$)
θ	time (sec)
ρ_B	boron density (gm/cm^3)
$\rho_{B_2O_3}$	boric oxide density (gm/cm^3)

5.2 MODEL OF MEESE AND SKIFSTAD

A	surface area, cm^2
c_p	specific heat, $\text{cal/g-}^\circ\text{K}$
d	particle diameter, cm
E	activation energy for evaporation
ΔH_f	heat of fusion of boron, cal/g
ΔH_{vap}	heat of vaporization of boron oxide, cal/mole
h	convective heat-transfer coefficient, $\text{cal/cm}^2 \text{ sec-}^\circ\text{K}$
k	thermal conductivity, $\text{cal/cm-sec-}^\circ\text{K}$
M	molecular weight, g/g-mole
m	mass, g
P	pressure, atm
Pr	Prandtl number of the gas
Q	heat of combustion of boron with diatomic oxygen to form liquid B_2O_3 , cal/mole; total energy, cal
R	molar rate of consumption of boron, g-mole/sec; gas constant
R_E	molar rate of evaporation of boron oxide, gm-mole/sec
Re	Reynolds number based on particle diameter and relative velocity between the gas and particle
r	radius, cm
Δr	oxide film thickness, $r_2 - r_1$, cm
T	temperature, $^\circ\text{K}$
t	time, sec
x_{H_2O}	mole fraction of H_2O present in the gas
α	surrounding absorptivity (=1.0)
ϵ	particle emissivity (=0.8)
λ	particle burning rate, cm/sec
ρ	density, g/cm
σ	Stefan-Boltzmann constant, $\text{cal/cm}^2 \text{ sec}^\circ\text{K}^4$

TABLE 5. (Continued)

5.3 MOHAN'S MODEL

C	average molecular velocity normal to the surface (cm/sec)
C_t	heat capacity of $B_2O_3(L)$ (cal/gm $^{\circ}$ K)
D	diffusion coefficient (cm 2 /sec)
d	diameter of particle (cm)
h	thickness (cm)
k	effective distribution coefficient related to the ratio of the mole fraction of O_2 absorbed in $B_2O_3(L)$ to gas phase mole fraction
k'	distribution ratio (liquid phase to gas phase O_2 concentration)
L	sum of heat losses by radiation and conduction $\frac{\text{cal}}{\text{cm}^2 \text{ sec}}$
P	total ambient pressure (atm)
q_B	heat liberated per unit mass of boron consumed at B (cal/g)
q_C	heat absorbed per unit mass of B_2O_3 vaporized at C (cal/g)
R_B or C	regression rate of the surface (cm/sec)
R°	universal gas constant ($8.316 \cdot 10^{-7}$ erg/gm-mole $^{\circ}$ K)
T	temperature ($^{\circ}$ K)
t	time (sec)
W_i	atomic weight
X	mole fraction of O_2 in the ambient atmosphere
X_a	ratio equilibrium vapor pressure of B_2O_3 at T_c to total pressure
α	evaporation coefficient
ϵ	emissivity
λ	gas phase thermal conductivity (cal/cm \cdot sec $^{\circ}$ K)
$\rho_{B,C}$	density boron and B_2O_3 (gm/cm 3)
τ	time for the new combustion regime to appear (sec)
B,C	surfaces

5.4 VOVCHUK'S MODEL

C_p	molar specific heat
D	diffusion coefficient
d_{do}	initial diameter of the boron droplet
H_i	total enthalpy of species i
ΔH_i	heat of reaction of species i
I_i	molar flux of species i
M_B	mass flow of the boron reacting in unit time
P	total pressure
P_i	partial pressure of species i
Q_R^K	radiative heat flux
R	universal gas constant
r	radius
T	temperature
ϵ	emissivity

TABLE 5. (continued)

λ	thermal conductivity of gas
ν_i	molecular weight
ν_i	stoichiometric coefficients
ρ_i	density
σ	Stefan's constant
τ_r	droplet combustion time

Subscripts

B	(molten) boron
K	particle or particle surface
∞	infinity

Note: units not stated, therefore any consistent set of units may be used..

5.5 EDELMAN'S MODEL

A	number of moles of oxygen per mole of product
a	the total (dimensionless) particle consumption rate
B	number of moles of boron per mole of product
C_D	drag coefficient
C_P	specific heat of the gas ($\text{ft}^2/\text{sec}^2 \text{ } ^\circ\text{K}$)
C_{P_S}	specific heat of boron at the surface ($\text{ft}^2/\text{sec}^2 \text{ } ^\circ\text{K}$)
ΔH_R	heat of reaction (calorie/gram)
K_S	surface reaction rate constant
L	latent heat of vaporization
M_B	molecular weight of boron (g/g-mole)
M_{N_2}	molecular weight of nitrogen (g/g-mole)
M_{O_2}	molecular weight of oxygen (g/g-mole)
M_{prod}	molecular weight of the product (g/g-mole)
M_s	average molecular weight at the particle surface (g/g-mole)
P	pressure (in atmospheres)
$P_{V,B}(T_p)$	vapor pressure of boron (atm)
R	particle radius (feet)
T_g	gas temperature ($^\circ\text{K}$)
T_p	particle temperature ($^\circ\text{K}$)
T_w	temperature of the wall ($^\circ\text{K}$)
V_g	gas velocity (ft/sec)
V_p	particle velocity (ft/sec)
$Y_{B,S}$	mass fraction of boron at the surface of the particle
$Y_{N_2,S}$	mass fraction of nitrogen at the surface
$Y_{O_2,S}$	mass fraction of oxygen at the surface of the particle
$Y_{O_2,\infty}$	mass fraction of oxygen in the surrounding (gas)

TABLE 5. (Continued)

$y_{\text{prod},S}$	mass fraction of the product at the particle surface
α	fraction of vaporized product
δ_s	particle bulk density (slugs/ft ³)
ϵ	emissivity
λ	the thermal conductivity of nitrogen (lbs force/sec °K)
ρ_g	gas density (slugs/ft ³)
ρ_s	density at the surface of the particle (slugs/ft ³)
σ	Stefan Boltzmann constant (lbs force/ft·sec °K ⁴)

and mass transfer. In most of the formulations the energy equation is the central element of the model, with the size history and other transport relationships representing auxiliary elements.

King (Refs. 11, 12) considers three stages in the boron combustion process: below the phase change temperature of the boron, at the point of boron phase change, and above the temperature at which phase change occurs (2450°K). Meese and Skifstad (Ref. 13), who based their model on King's 1972 paper (Ref. 12) also include boil-off of the oxide layer. In King's model it is assumed that the particle is moving at the velocity of the surrounding gas, while Meese and Skifstad and Edelman et al. allow for slip between particle and gas phase through the use of a convective heat transfer coefficient. Vovchuk (Ref. 14) does not include convective heat transfer, so that in Table 3 this section is omitted in summarizing Vovchuk's work. (A similar approach is followed in each case in which a given section of Table 3 does not apply to a particular model.) Particle-gas radiation is included in each of the models studied, and the expressions used in each model for this component of the overall heat transfer process are essentially interchangeable, with only those differences related to specific model geometry. It should be noted that the radiation term shown for Vovchuk's model is eventually neglected.

King (Refs. 11 and 12), Meese and Skifstad (Ref. 13), and Mohan and Williams (Ref. 15) all consider oxide formation via the global reaction $B + 3/4 O_2 \rightarrow 1/2 B_2O_3$. Vovchuk (Ref. 14) allows for the formation of the lower oxides BO, BO_2 , and B_2O_2 at the particle surface. Edelman et al. (Refs. 16, 17) considers the product species to be either BO or B_2O_3 , but if BO forms it does not oxidize further. Except for the work of Edelman, et al., all of the models assume that the reaction rate is diffusion controlled. The model described by Edelman, et al. involves a finite-rate reaction of B to either BO or B_2O_3 (vapor). King, and Meese and Skifstad, both include oxide consumption in their models, through the effect of water on boric oxide ($B_2O_3 + H_2O \rightarrow 2 HBO_2$). The only other mechanism considered in any model for oxide removal is evaporation.

The diffusion equations used in King's work are algebraic in form and depend upon the absolute value of the pressure at the surface and at infinity. Vovchuk integrates the partial pressure from the particle surface to infinity. For diffusion through the oxide layer King and Meese and Skifstad, use similar equations which vary only in one constant; the constant used by Meese and Skifstad was derived from data unavailable to King and thus provides a better fit of the available experimental data.

A major feature of King's model (Refs. 11, 12) is the expression representing boron phase change; Meese and Skifstad (Ref. 13) use a similar equation, derived, however, in a slightly different fashion. Edelman, et al. (Refs. 16, 17) provide an expression for the finite-rate evaporation of boron. Phase change does not directly enter the models reported by Vovchuk (Ref. 14) or Mohan and Williams (Ref. 15). King, and Meese and Skifstad, again use a similar expression for boric oxide evaporation, while Vovchuk, and Edelman, et al. have no oxide layer to remove. The oxide phase change model incorporated by Mohan and Williams instead of being equilibrium controlled, is finite rate. As noted earlier, Edelman, et al. describe the only model which includes finite-rate kinetics, but in this model it is assumed that the particle has ignited and no B_2O_3 layer is present, so that oxidation of the boron proceeds directly to either BO or B_2O_3 . Vovchuk considers only boron combustion but in the diffusion controlled mode.

The end product of Vovchuk's model is an expression for the particle burning time, and an expression for burning time is also obtained by Mohan and Williams. In the model described by Meese and Skifstad, it is assumed that no other phenomena occur while the oxide layer boils off, leading to an independent expression for the oxide layer boil-off time. All of the models except Vovchuk's provide expressions for the size decrease of the particle with time as combustion occurs; for those models which incorporate an oxide layer expressions for the time-rate of change of the oxide layer thickness are also defined by the analysis. In three of the models: those of King,

Meese and Skifstad, and Mohan and Williams. ignition time is also provided. In each case ignition is defined as the point at which the oxide layer boils or flashes off.

What this review indicates is that the two most potentially useful models are those described by King (Refs. 11, 12) and by Edelman, et al. (Refs. 16, 17). Each of these approaches is the most general of its respective formulation; diffusion controlled burning in the King approach, including the effects of an oxide layer, and combined diffusion and finite-rate kinetics, but without an oxide layer, on the model of Edelman, et al. The other approaches are either a derivative of these more general models or considerably more restricted in application.

Because it includes both diffusion and finite-rate chemical kinetics mechanisms, the model proposed by Edelman, et al. is useful for examining the available data for boron particle consumption rate as a function of particle size. Since the oxide layer is assumed not to exist, this approach can be interpreted as a model for the combustion process after particle ignition. It is thus useful for examining kinetics effects in boron consumption, keeping in mind that the results obtained represent a limiting case of the overall boron combustion process.

2.2.2 Model Description

The boron combustion model considered in this work involves the simultaneous solution of these coupled differential equations describing the velocity, size, and temperature of the particle. These equations can be written:

$$\frac{dV_p}{dt} = \frac{3C_{D^0}g(V_g - V_p)^2}{8R\delta_s}, \quad (18)$$

where C_D = drag coefficient
 ρ_g = gas density (slugs per cubic foot)
 V_g = gas velocity (ft/sec)
 V_p = particle velocity (ft/sec)
 R = particle radius (feet)
 and δ_s = particle bulk density (slugs/ft³)

$$\frac{dR}{dt} = \frac{-a\lambda N_u}{2R\delta_s C_p}, \quad (19)$$

where a = the total (dimensionless) particle consumption rate (see Eq. 21)
 λ = the thermal conductivity of nitrogen (in pounds force/sec °K)
 N_u = Nusselt number
 C_p = specific heat of the gas (in ft²/sec² °K), and the remaining variables as already defined.

$$\frac{dT_p}{dt} = \frac{3a\lambda N_u}{2\delta_s C_{p_s} R^2 C_p} \left[\frac{C_p (T_g - T_p)}{e^a - 1} - L + \frac{AK_s (2C_{p_s} R) Y_{O_2,s} M_B \Delta H_R}{a\lambda N_u M_{O_2}} - \frac{2\epsilon RC_p (T_p^4 - T_w^4)}{a\lambda N_u} \right] \quad (20)$$

where C_{p_s} = specific heat of boron at the surface (ft²/sec² °K)
 T_g = gas temperature (°K)
 T_p = particle temperature (°K)
 L = latent heat of vaporization
 A = number of moles of oxygen per mole of product
 K_s = surface reaction rate constant

ρ_s = density at the surface of the particle (slugs/ft³)

$Y_{O_2,s}$ = mass fraction of oxygen at the surface of the particle

M_B = molecular weight of boron (g/g·mole)

ΔH_R = heat of reaction (calorie/gram)

M_{O_2} = molecular weight of oxygen (g/g·mole)

σ = Stefan-Boltzmann Constant (lb·force/ft·sec °K⁴)

ϵ = emissivity

T_w = temperature of the wall (°K)

and other parameters are as defined above.

The values for the remainder of the time-varying parameters are treated as simple algebraic equations (using the current value of T_p and R) as follows

$$a = \frac{88.662 C_p \alpha R}{\lambda Nu} \sqrt{\frac{M_B}{T_p}} \left[P_{v,B(T_p)} - \frac{M_s}{M_B} Y_{B,S} P \right] + \frac{2 M_B K_s Y_{O_2,s} C_p \rho_s R A}{M_{O_2} \lambda Nu} \quad (21)$$

where α = fraction of vaporized product

$P_{v,B(T_p)}$ = vapor pressure of boron (atm)

M_s = average molecular weight at the particle surface (g/g·mole)

$Y_{B,S}$ = mass fraction of boron at the surface of the particle

P = pressure (in atmospheres)

and other variables are as previously defined.

$$Y_{O_2,s} = \frac{Y_{O_2,\infty} e^{-a}}{1 + BK_s \left[\frac{2(1-e^{-a})C_{p,s}R}{a\lambda Nu} \right]} \quad (22)$$

where $Y_{O_2,\infty}$ = mass fraction of oxygen in the surrounding (gas)

B = number of moles of boron per mole of product

and the remaining variables are as previously defined.

$$Y_{B,s} = (1-e^{-a}) \left[1 - AK_s \frac{2Y_{O_2,s}C_{p,s}R}{a\lambda Nu} \left(\frac{M_B}{M_{O_2}} \right) \right] \quad (23)$$

$$Y_{prod,s} = (1-e^{-a}) \left[\frac{2K_s Y_{O_2,s} C_{p,s} R}{a\lambda Nu} \left(\frac{M_{prod}}{M_{O_2}} \right) \right] \quad (24)$$

where $Y_{prod,s}$ = mass fraction of the product at the particle surface

M_{prod} = molecular weight of the product (g/g-mole)

and the remaining parameters are defined above

$$M_s = \text{average molecular weight at the surface} = \left[\frac{Y_{O_2,s}}{M_{O_2}} + \frac{Y_{B,s}}{M_B} + \frac{Y_{prod,s}}{M_{prod}} + \frac{Y_{N_2,s}}{M_{N_2}} \right]^{-1} \quad (25)$$

where M_{N_2} = molecular weight of nitrogen (g/g-mole)

$Y_{N_2,s}$ = mass fraction of nitrogen at the surface

and the remaining variables as previously defined.

$$Y_{N_2,s} = (1 - Y_{O_2,s} - Y_{B,s} - Y_{prod,s}) \quad (26)$$

In this formulation the coupling is provided by the appearance in the energy equation of the parameter α , the total (dimensionless) particle combustion rate, which is itself a function of the surface concentrations of both O_2 and B. Thus, the solution problem is one of solving three highly nonlinear, strongly coupled ordinary differential equations. The code developed for this work implemented a Newton-Raphson scheme to solve this coupled set of equations, and this approach proved to be reliable and relatively rapid. Thus the approach was then used to investigate different aspects of the combustion of boron through comparison of results with available experimental data.

2.2.3 Boron Combustion Analyses

The model described in this report combines both diffusive transport and chemical kinetic mechanisms and can thus be used to examine kinetics limitations on boron combustion as a function of particle size, ambient oxygen concentrations, pressure and ambient temperature. Each of these variables is of direct practical interest because each impacts the use of boron in a combustion process. For example, one strategy for maximizing boron combustion efficiency is to hold the boron in an oxygen-deficient environment until it is heated sufficiently to avoid oxide layer formation. Under this scenario, the kinetics of boron consumption at elevated gas temperatures becomes important. As another example, in many propulsion system applications a boron-slurry-fueled vehicle would be required to operate over a wide range of altitudes and flight Mach numbers. This impacts both the temperature in the combustor and the ambient pressure. Thus, these impacts on the kinetics of boron consumption are of interest.

As particle size decreases, at constant pressure, the effects of chemical kinetics increase relative to those of diffusion. This is clearly shown by the results presented in Fig. 16. For example, for 1 atm pressure, the transition from kinetics control ($\tau_b \propto d$) to diffusion control ($\tau_b \propto d^2$) occurs for particles somewhat larger than 200 μm . However, this transition

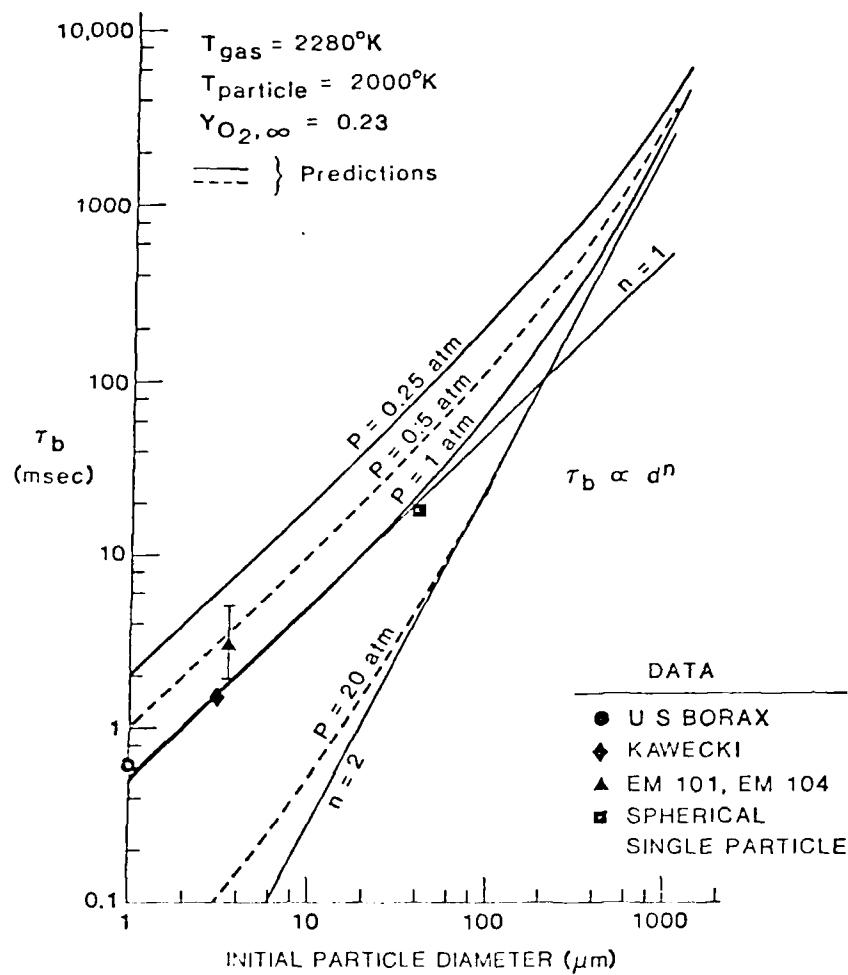


Figure 16. Predicted Kinetic-to-Diffusion Controlled Combustion of Boron

is itself a function of pressure, as the results indicated in Fig. 16 also show. At low pressure, typical of high-altitude ramjet operation, the transition to diffusion control occurs at diameters so large as to be well outside the range of practical interest (for this hot-gas, hot particle case), while at high pressures, such as might be encountered in an advanced gas turbine combustor, the consumption process is diffusion-controlled even for quite small particles.

In most applications, boron particle sizes must be kept small, even at elevated pressures, to avoid long burn times. This is illustrated by Fig. 17, in which the results depicted on Fig. 16 are cross-plotted to indicate the effects of pressure on consumption time for a given particle size. It is immediately evident from this figure that for large particle sizes burn times greater than 10 ms would be expected (in the absence of a B_2O_3 coating; considerably larger burn times can be anticipated for B_2O_3 -clad particles). Note also that for large particles the burn time tends to become independent of pressure at high pressures as the transition to diffusion control is completed. For small particles, on the other hand, kinetics effects dominate throughout the pressure range studied, and at a few atmospheres pressure burn times of a fraction of a millisecond can be achieved.

While the data shown in Fig. 16 represent high-temperature boron combustion, much of the available data involves ignition and combustion in a cold environment. Figs. 18 and 19 provide data at several pressure levels, for several particle sizes, at two ambient oxygen concentrations, and show comparisons between the data and predictions carried out using the present model. Overall, the agreement between the data and the model predictions is quite good, although the model does not represent well the decrease in burn time at pressures above about 20 atmospheres that may be indicated by the data. Another aspect of the model prediction is also of interest: at low pressures, for smaller particles, the model predicts that the boron consumption process will quench, leaving a non-negligible residue. This residue particle, while not insignificant from a combustion inefficiency standpoint,

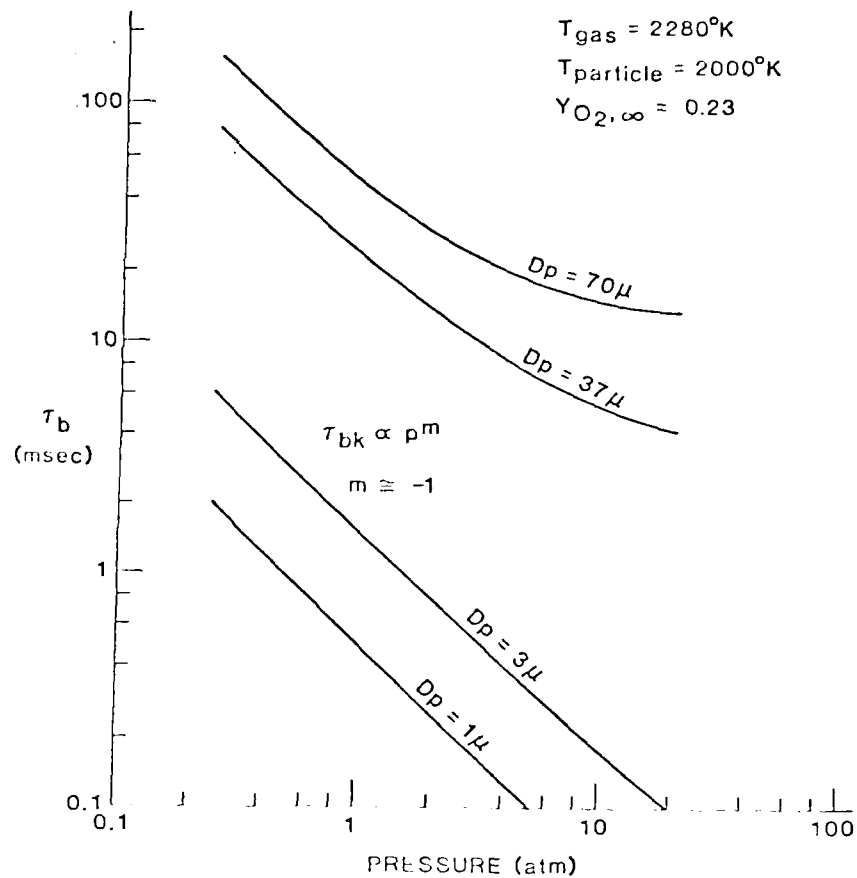


Figure 17. Effect of Pressure on Burn Time

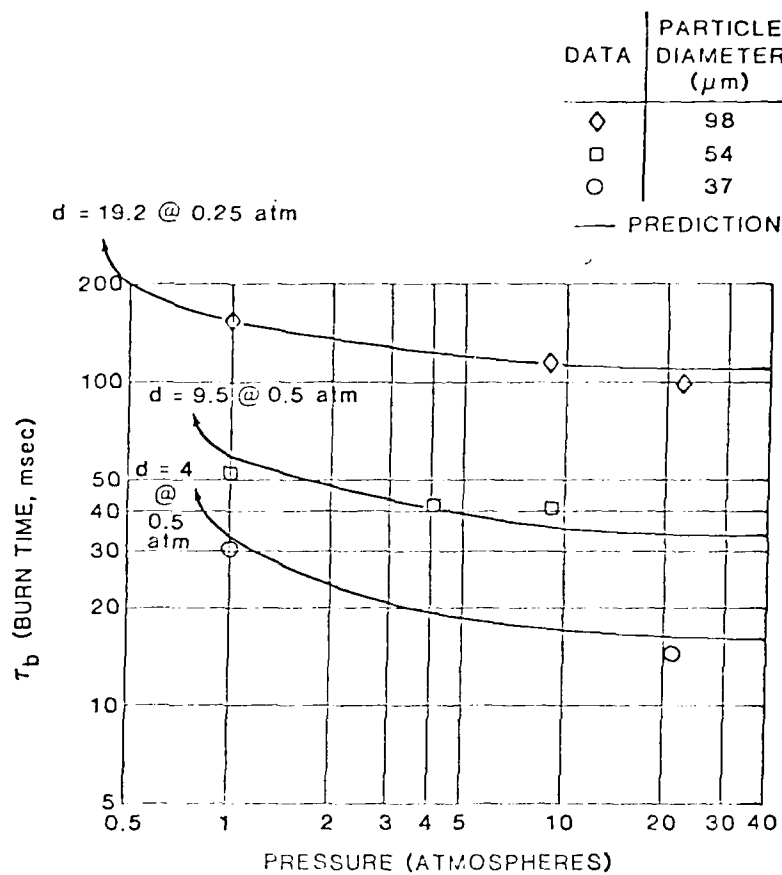


Figure 18. Comparison of Predictions with Data; Oxygen Concentration = 0.21, $T_{\text{Gas}} = 300^\circ\text{K}$

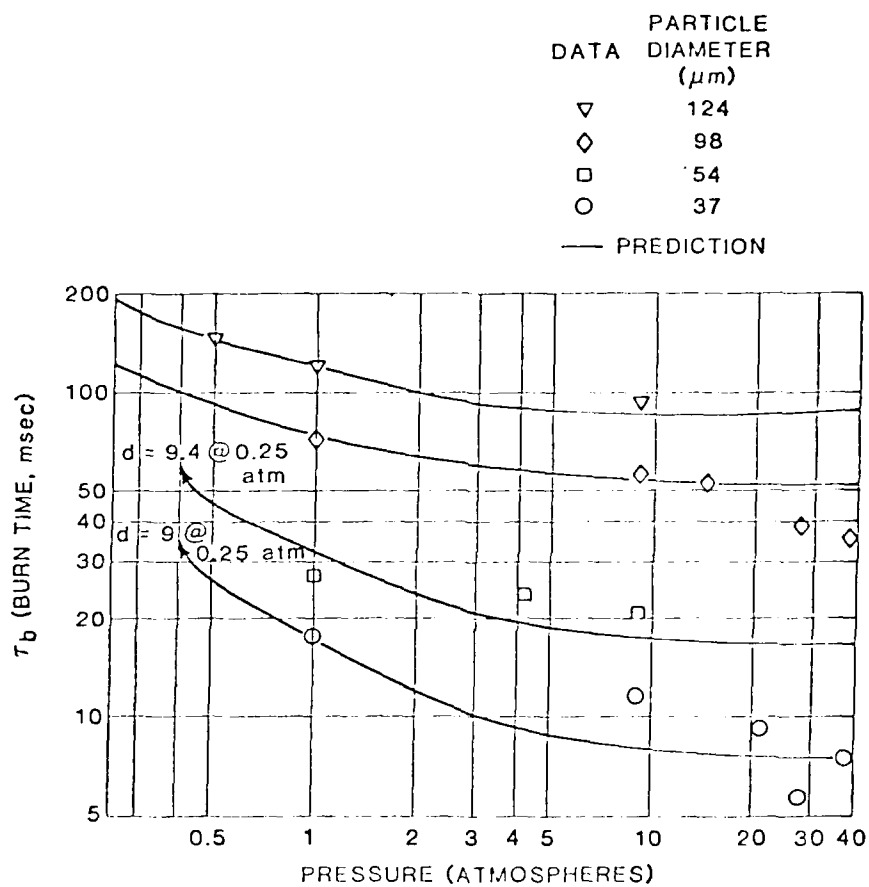


Figure 19. Comparison of Predictions with Data:
Oxygen Concentration = 0.40, $T_{\text{Gas}} = 300^\circ\text{K}$

is not large and could be missed in experimental studies unless its presence was specifically being investigated. The quenching process appears to occur at high pressures for smaller particles, and could be of considerable significance in ramjet operation, where afterburning can be continuing in the exhaust nozzle.

2.2.4 Finite-Rate B_2O_3 Condensation

While the existence of B_2O_3 as an oxide coating on a boron particle is of critical importance in the examination of boron particle ignition, the condensation of the oxide out of the gas phase is also critical to the overall performance of a boron slurry fueled ramjet. This follows from the fact that approximately 30% of the available energy of boron combustion is tied up in the phase transformation between liquid and gaseous B_2O_3 . Where recondensation of B_2O_3 occurs -- in the combustor or in the nozzle -- is thus critical to achieving the optimum performance levels utilizing boron fuels.

Finite-rate condensation effects can be analyzed using single particle nucleation and growth theory. For example, nucleation rate can be approximately using the expression

$$J = B \exp \left(\frac{-\Delta G}{KT} \right) \quad (27)$$

from classical kinetic theory, where

K is the Boltzmann constant,
T is the local temperature, and
B is a rate constant;

ΔG is the free energy of formation of a critical cluster, itself a function of the surface tension of the material, the work of cluster formation, and the number of molecules in a critical droplet. Thus $\Delta G = f_1(\sigma, \omega^*, n^*)$. w^*

and n^* are both functions of r^* , where r^* is the radius of a critical droplet. A number of expressions have been devised for the terms representing the work of cluster formation and the number of molecules in a critical droplet. For example, in the expression developed by Yang (Ref. 18) and used by Edelman and Economos (Ref. 19) to examine boron condensation phenomena, the work of cluster formation is given by

$$\omega^* = \frac{4}{3} \pi \sigma r^{*2} \quad (28)$$

where σ is the liquid surface tension, and the number of molecules in a critical drop is expressed as

$$n^* = \frac{4}{3} \pi \frac{r^{*3}}{M_L} \zeta_L \quad (29)$$

in which M_L is the molecular weight and ζ_L the density of the liquid condensate.

The radius of a critical drop can be expressed as

$$r^* = \frac{2\sigma M_L}{\zeta_L R_0 T \ln(P_v/P_{v\infty})} \quad (30)$$

where P_v is the vapor partial pressure and $P_{v\infty}$ is the equilibrium-saturation partial pressure, i.e., the vapor pressure of a vapor in equilibrium with a plane surface of condensed phase. R_0 is of course the universal gas constant.

Once the nucleation process produces a critical size droplet, it continues to grow by the additional deposition of condensing vapor. A growth law which has been used to calculate water vapor condensation phenomena is given by the expression

$$\frac{dr}{dt} = \frac{(P_v - P_{v\infty})}{\zeta_L} \left(\frac{M_L}{2\pi Kt} \right)^{1/2} \quad (31)$$

Finally, the total production rate of condensed-phase B_2O_3 can be written

$$\dot{w}_{B_2O_3} = \dot{w}_n + \dot{w}_G = \rho J + \sum_j \bar{w}_p^j \quad (32)$$

where the growth rate term is summed over several classes of particles defined by a mean radius r_j , i.e.,

$$w_p^j = 4\pi(r_j)^2 \rho_L N_p^j \frac{dr_j}{dt} \quad (33)$$

in which N_p^j gives the number density of particles of radius class j .

Application of this approach to the finite-rate condensation of B_2O_3 requires knowledge of the surface tension of B_2O_3 and its equilibrium-saturation partial pressure. These data can be estimated for the temperature ranges of interest through modest extrapolation of available data. For example, as shown by Fig. 20, data included in the JANNAF tables allows a modest extrapolation of the low-temperature data to fit the empirical expression

$$P_{v\infty} = \exp \left(19.03 - \frac{44080}{T} \right) \quad (34)$$

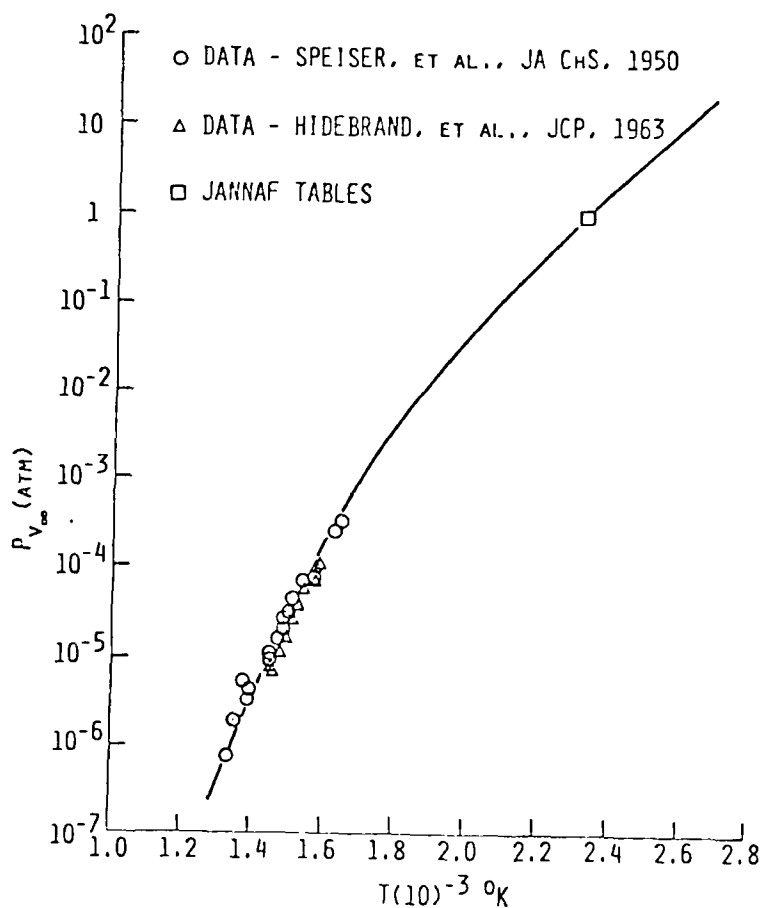


Figure 20. B_2O_3 Vapor Pressure Data

Surface tension data requires a rather larger extrapolation, as shown by the data included in Fig. 21.

The physical data described here and the expressions for nucleation and condensation set out in this section were used in the work outlined in Ref. 19 to compute the condensation of B_2O_3 in a supersonic nozzle expansion process; the B_2O_3 condensation model was incorporated in an analysis which coupled finite-rate chemistry for the B-O-H-N system with finite-rate condensation phenomena. Fig. 22 shows the nozzle pressure distribution data obtained in a test involving B_2O_3 condensation. These experimental data show a definite departure from the otherwise isentropic expansion associated with the conical nozzle geometry. Also given in this figure are the results of a calculation based on the assumption that the latent heat of B_2O_3 condensation is released instantaneously, resulting in a Rayleigh line process assumed to occur in the vicinity of the condensation-induced pressure rise as indicated by the data. The heat release used in the Rayleigh model is based on the condensation of all of the available B_2O_3 in the flow. These results indicate that the agreement of the Rayleigh analysis and the experimental data is in fact quite good, although the ideal model somewhat overestimates the magnitude of the experimental pressure rise. On the other hand, the coupled finite-rate condensation and gas phase kinetics approach agrees fairly well with the data though the initial pressure change is somewhat underpredicted. This initial underprediction casts some doubt on the nucleation and growth laws used in this study, but given the meager data available both for the physical parameters which enter the models and for testing and development of the expressions themselves, such a deviation from measured data as shown here is not unexpected. This work does, on the other hand, provide evidence that the effects of B_2O_3 condensation can be included in analytical approaches intended to model the performance of boron-fueled combustors.

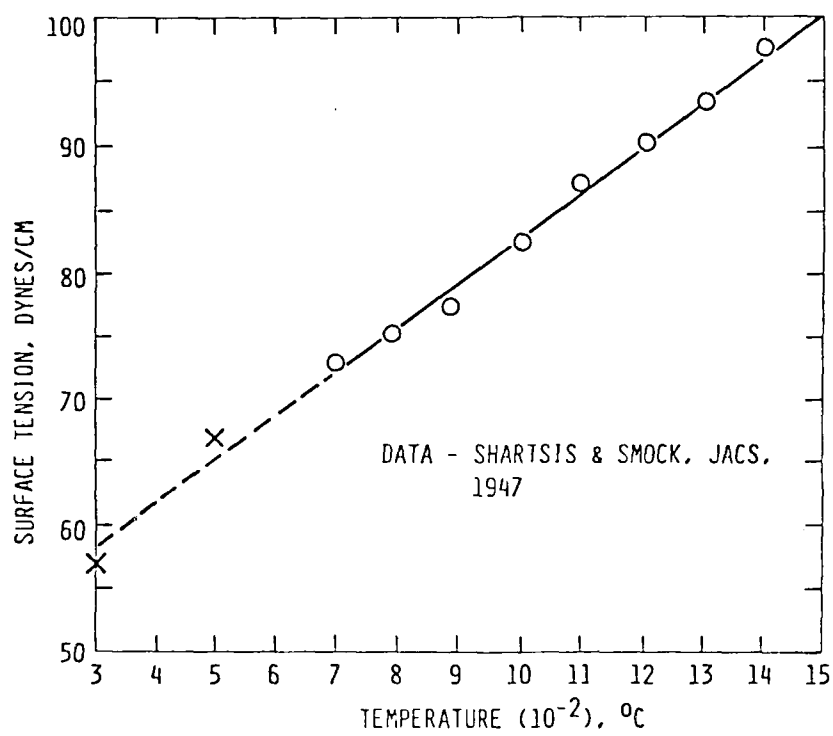


Figure 21. Surface Tension of B₂O₃

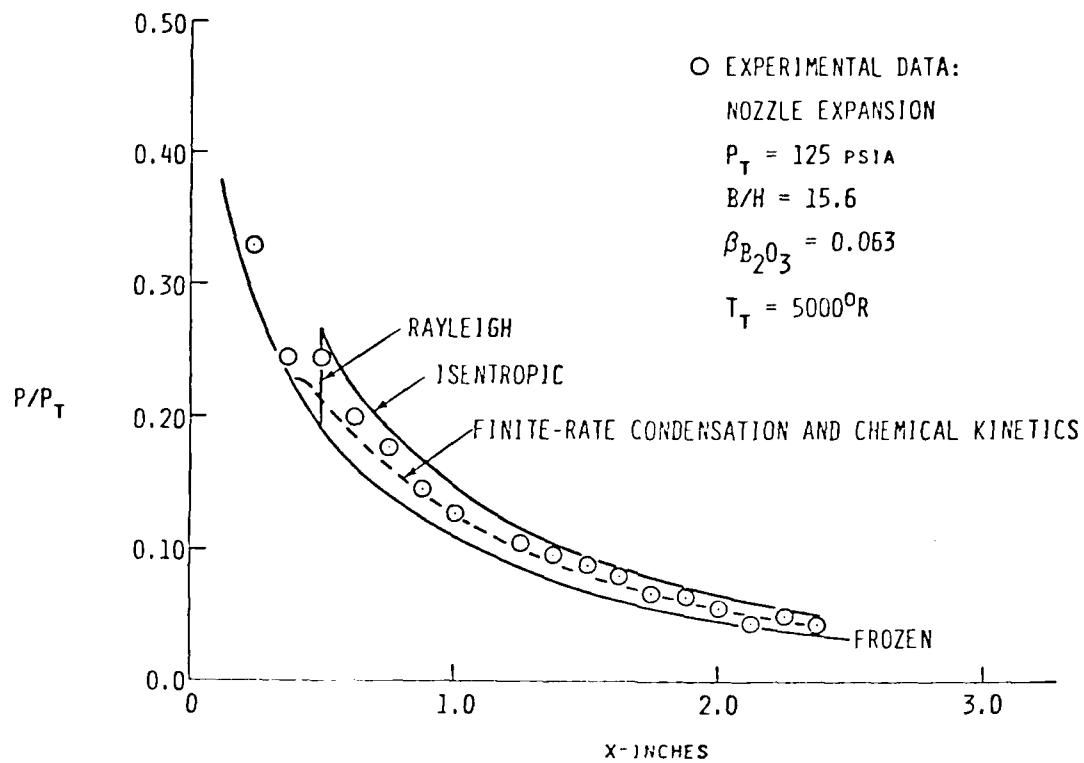


Figure 22. Effects of B_2O_3 Condensation in a Supersonic Nozzle Expansion

2.2.5 Discussion

The results presented in this section indicate that a coupled diffusion and finite-rate kinetics approach is required to adequately examine boron combustion in the context of its use as a fuel in ramjet combustors. These results show that coupling finite-rate oxidation kinetics with diffusional processes allows the behavior of boron combustion as observed in laboratory experiments to be explained, in terms of burn time/particle size and pressure and temperature relationships. An understanding of these phenomena is crucial to the utilization of boron in combustors. The computations also clearly indicate quenching of the boron combustion process even for clean (oxide free) particles for certain combinations of particle size, ambient temperature, and ambient oxygen concentration.

Just as clearly the work described herein indicates the need for a number of improvements. For example, incorporation in the modeling of the presence of an oxide layer on the particle is needed to adequately account for boron ignition phenomena. The role and potential importance of suboxide formation and disposition remains unclear, and more mechanistic and detailed models of B-O, B-O-H, and B-O-H-C kinetics are clearly required. Additionally, the work reported herein also shows that B_2O_3 condensation processes can be modeled, and the impact of this on the overall heat release obtained with boron combustion is such that B_2O_3 condensation needs to be controlled to optimize combustion efficiency. Further work remains to establish appropriate analyses of these processes. Finally, cloud and slurry spray combustion analyses need to be established to aid in the practical use of boron slurry fuels. The individual parts of such an analysis exist, as indicated by the spray modeling work considered in the preceding section, the single-particle boron modeling considered here, and the modular model work to be discussed in the next section. What is required is the merging of the efforts in these three research areas.

The modular model for ramjet performance assessment represents the most advanced and detailed combustor model applicable to sudden-expansion ramjets. It has been developed because the complex flame stabilization, flame propagation, and spray combustion problems which have been encountered in the development of dump combustors require a detailed analytical capability for their resolution. The ability to compute in some detail combustion chamber flowfields is necessary in order to understand the phenomena that occur in existing combustors and to predict the performance of new combustor concepts.

In its basic form, the modular model approach has been described in a variety of reports and papers, of which Refs. 20 and 21 are examples. The model described in this report, however, differs from those previously described in two key areas: first, the well-stirred reactor chemistry model is fully integrated with the chemistry modeling applied to the directed flow, and second, the advanced quasiglobal model for hydrocarbon combustion kinetics is incorporated in the code. This latter difference between the present model and prior versions of the modular approach is extremely important because it is only with the advanced quasiglobal model that it is possible to accurately characterize the combustion kinetics and heat release processes that occur in fuel-rich regions. Since fuel-rich regions make up a significant portion of nonpremixed ramjet combustor flowfields, and can be a significant cause of combustion inefficiency in ramjet operation, this fuel-rich combustion characterization ability is a key requirement for an overall ramjet combustor performance model.

The modular concept is that the combustor flowfield can be broken down into three major components, as represented schematically in Fig. 23. These components are a directed flow (which is computationally modeled as a flowfield satisfying the boundary layer approximation that axial gradients are negligible compared to radial gradients, and the static pressure is radially uniform); a recirculation zone (assumed to be representable as a well-stirred reactor or a combination of well-stirred reactors); and a turbulent shear layer region, located along the dividing streamline

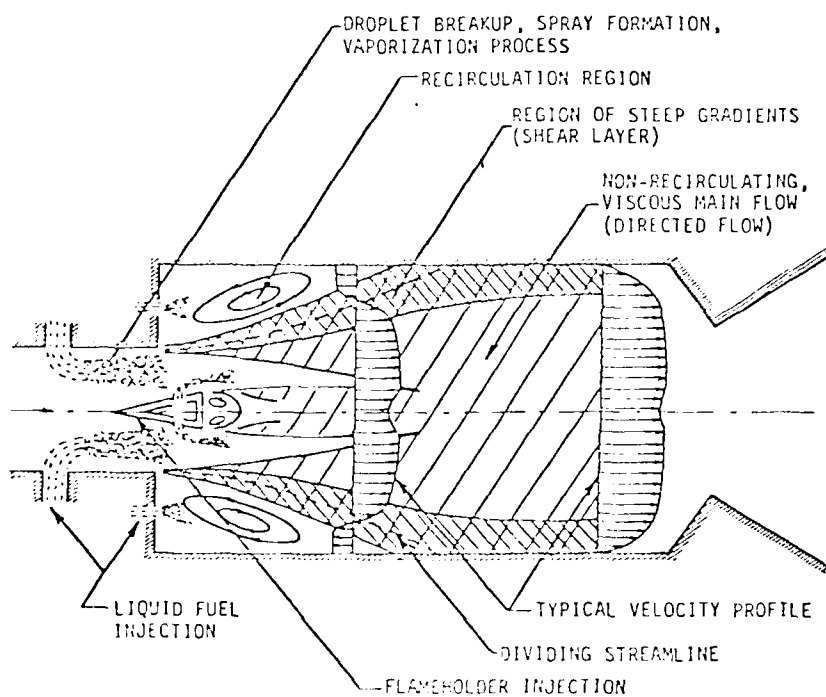


Figure 23. Schematic of Sudden-Expansion (Dump) Burner

which separates the other two regions. The shear layer serves to couple the other two model components; fluxes of species and energy across this shear layer form the boundary conditions on the two computational regions. The directed flow is assumed to be fully turbulent, with the turbulent effective viscosity defined by a conventional two-equation turbulence model (Ref. 22).

2.3.1 Stirred Reactor Modeling of Dump Combustor Recirculation Zones

The well-stirred reactor, shown schematically in Fig. 24, is a laboratory device in which very high mixing rates are achieved. In general, laboratory stirred reactors are designed to ensure that the mixture within the reactor is spatially uniform, so that unreacted feed material is continuously and uniformly mixed with combustion products, reacting for a time defined by the average residence time of the reactor before exiting. For the limit of perfect stirring, this average residence time is given simply by the ratio of the product of the stirred reactor volume and density to the feed mass flow, $\rho V/\dot{M}$; the product mass flux is of course equal to the feed mass flux. In this limit the governing equations for the stirred reactor state reduce to algebraic relations, which allows the use of rapid and efficient solution procedures.

In the lower half of Fig. 24, a typical recirculation region in a sudden-expansion combustor is sketched. Because of the high turbulence intensity and large mixing rates generated in the recirculation zone, the limiting behavior of this region can be thought of as well-mixed, that is, the state of the recirculation region is defined by the chemical kinetics of the reactions occurring and not by the mixing rate. In this sense the volume within the recirculation region sketched in Fig. 24(b) is similar to the volume within the laboratory stirred reactor in Fig. 24(a), and the same solution technique can be used to obtain the thermo chemical static. A comparison of Figs. 24(a) and 24(b) also shows the major difference between the recirculation region and the laboratory stirred reactor. In the laboratory stirred reactor, discrete reactant and product streams can be identified, but in the well-stirred reactor model of a sudden-expansion recirculation zone, separate reactant and product streams cannot be defined. Instead, reactants enter and products leave the recirculation region by turbulent diffusion through

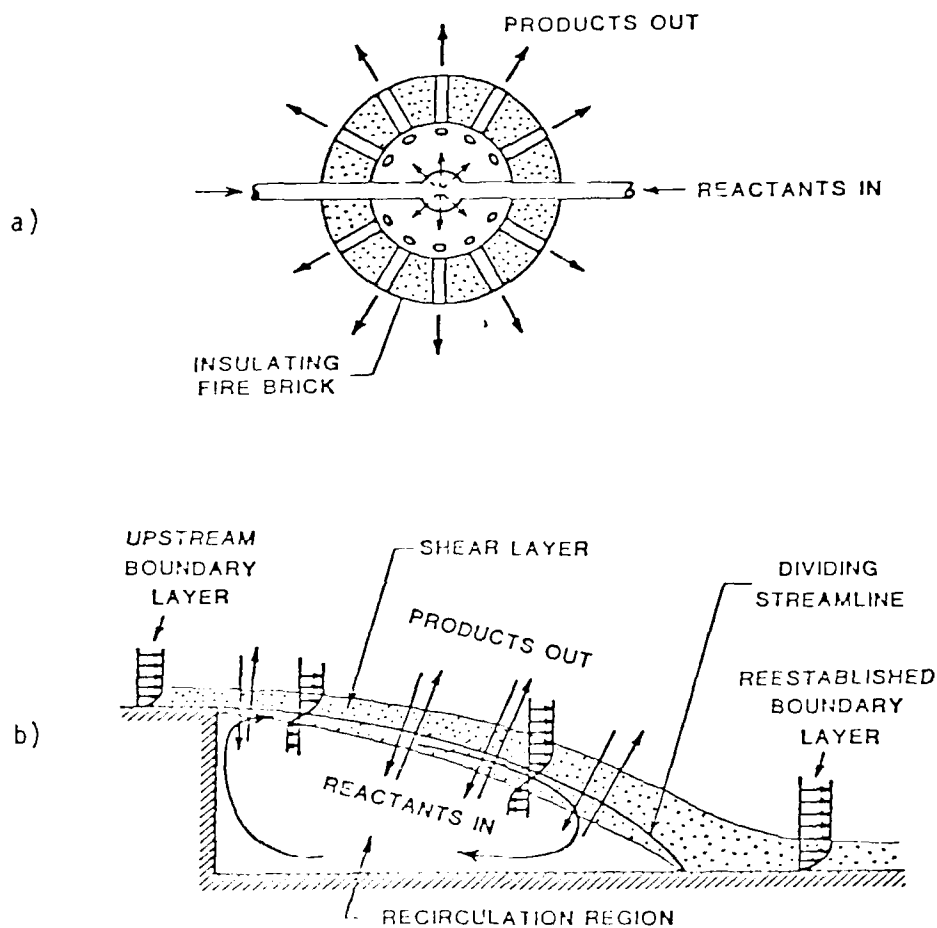


Figure 24. Comparison of Well-Stirred Reactor with Recirculation Region Flowfield.
 a) Schematic design of Spherical Well-Stirred Reactor
 b) Schematic of Sudden-Expansion Recirculation Region

the shear layer which surrounds the dividing streamline. Thus, the reactant stream is the flux of reactants passing through the shear layer, integrated over the surface area of the dividing streamline, and the product stream is defined similarly. These fluxes are of course equal and opposite.

The equations describing the transport of energy and species in the well-stirred reactor reduce to the following relations:

$$\text{Continuity} \quad \dot{m}^I = \dot{m}^O = \dot{m} \quad (35)$$

$$\text{Species,} \quad \frac{dM\alpha_i}{dt} = \dot{m}_i^I + V\dot{w}_i \quad (36)$$

$$\text{Energy,} \quad h = \sum_i h_i \alpha_i = h^I + \dot{Q}/\dot{m} \quad (37)$$

Note that in this set of equations the species transport equation is written in nonsteady form. This formulation has been adopted to facilitate solution of the stirred reactor governing equations with finite-rate chemical kinetics; the steady-state stirred reactor solution is obtained when $d\alpha_i/dt \rightarrow 0$.

Equations (35-37), along with expressions for the volumetric species production rates, for the enthalpy of individual species as a function of temperature, and the equation of state, define the temperature and species concentrations in the stirred reactor, given the inflow rates for species and enthalpy. In the modular model, the net inflow of species and enthalpy are each expressed as line integrals involving gradients evaluated along the dividing streamline, so that the energy and species conservation equations for the stirred reactor are written, respectively.

$$\begin{aligned}
& -2\pi \int_0^s R_c(X) \rho v_T \sum_i \left[h_i^I (T^I) \frac{\partial \alpha_i^I}{\partial r} \right] ds + \dot{Q} \\
& = 2\pi \int_0^s R_c(X) \kappa \frac{\partial T}{\partial s} ds \\
& -2\pi \int_0^s R_c(X) \rho v_T \sum_i \left[h_i^0 (T_R) \frac{\partial \alpha_i^0}{\partial r} \right] ds
\end{aligned} \tag{38}$$

and

$$\begin{aligned}
\frac{d\alpha_i}{dt} &= \frac{-2\pi}{\rho_c V} \int_0^s R_c(X) \left[\rho v_T \frac{\partial \alpha_i^I}{\partial r} \right] ds \\
& - \frac{2\pi}{\rho_c V} \int_0^s R_c(X) \left[\rho v_T \frac{\partial \alpha_i^0}{\partial r} \right] ds + \frac{\dot{w}_i}{\rho_c}
\end{aligned} \tag{39}$$

where ρv_T is evaluated using the outer flowfield solution in the region of the dividing streamline.

Because in the modular model the feed rates into the recirculation region are defined by the fluxes of reactants and products through the shear layer, this region becomes a key element of the model. Nevertheless, the shear layer is modeled simply as a region of linear gradients; that is, the gradient in a quantity ϕ at the dividing streamline is approximated by

$$\left(\frac{\partial \phi}{\partial r} \right)_w = \frac{\phi_P - \phi_R}{1} \tag{40}$$

Moreover, the width of the shear layer is assumed to be given by the linear expression

$$l = ax + b \quad (41)$$

in which a and b are defined through comparison of model predictions with experimental data. The results obtained with the modular approach have been found to be relatively insensitive to the values of the coefficients a and b in Eq. (41); for the results presented in this report, $a = 0.03$ and $b = 0.07$.

2.3.2 Parabolic Mixing: The Director-Flow Model

The second major element of the modular model for a sudden-expansion combustor is the formulation for the directed-flow portion of the combustor flowfield. It is assumed that the boundary-layer approximations apply to this part of the flowfield. For a steady, axisymmetric flow, the describing equations may be written as follows:

Global Continuity,

$$\frac{\partial r \rho u}{\partial x} + \frac{\partial r \rho v}{\partial r} = 0 \quad (42)$$

Species Diffusion for the i th Specie,

$$\rho u \frac{\partial \alpha_i}{\partial x} + \rho v \frac{\partial \alpha_i}{\partial r} = \frac{1}{r} \frac{\partial}{\partial r} \left\{ r \rho \frac{v_T}{Sc} \left[\frac{\partial \alpha_i}{\partial r} \right] \right\} + \dot{w}_i \quad (43)$$

Momentum Equation,

$$\rho u \frac{\partial u}{\partial x} + \rho v \frac{\partial u}{\partial r} = \frac{1}{r} \left\{ \frac{\partial}{\partial r} \left(r \rho v_T \frac{\partial u}{\partial r} \right) \right\} - \frac{\partial p}{\partial x} \quad (44)$$

Energy Equation,

$$\rho u \frac{\partial H}{\partial x} + \rho v \frac{\partial H}{\partial r} = \frac{1}{r} \frac{\partial}{\partial r} \left\{ \frac{r \rho v_T}{Pr} \left[\frac{\partial H}{\partial r} - \left(\frac{Pr}{Sc} - 1 \right) \sum_i h_i \frac{\partial \alpha_i}{\partial r} + (Pr - 1) \frac{\partial}{\partial r} \left(\frac{u^2}{2} \right) \right] \right\} \quad (45)$$

These equations, along with expressions for the enthalpy

$$H = h + (u^2/2) \quad \text{and} \quad h = \sum_i \alpha_i h_i(T) \quad (46)$$

and the equation of state

$$p = \rho R T \sum_i (\alpha_i / W_i) \quad (47)$$

can be solved, given an expression for the turbulent eddy viscosity $\mu_T = \rho v_T$. This is defined by a two-equation turbulent kinetic energy model, which introduces transport equations for the turbulent kinetic energy and its dissipation rate. In boundary-layer form, these equations can be written as follows:

Turbulent Kinetic Energy

$$\rho u \frac{\partial k}{\partial x} + \rho v \frac{\partial k}{\partial r} = \frac{1}{r} \frac{\partial}{\partial r} \left(\frac{\mu_T r}{\sigma_k} \frac{\partial k}{\partial r} \right) + \mu_T \left(\frac{\partial u}{\partial r} \right)^2 - \rho \epsilon \quad (48)$$

Turbulence Energy Dissipation,

$$\rho u \frac{\partial \epsilon}{\partial x} + \rho v \frac{\partial \epsilon}{\partial r} = \frac{1}{r} \frac{\partial}{\partial r} \left(\frac{\mu_T r}{\sigma_k} \frac{\partial \epsilon}{\partial r} \right) + C_{E1} \frac{\epsilon}{k} \mu_T \left(\frac{\partial u}{\partial r} \right)^2 - C_{E2} \rho \frac{\epsilon^2}{k} \quad (49)$$

where $\nu_T = C_\mu \rho k^2 / \epsilon$. A standard set of two-equation model coefficients has been used for all of the computations described in this report: thus $C_\mu = 0.09$, $C_{E1} = 1.40$, $C_{E2} = 1.95$, $\sigma_k = 1.00$, and $\sigma_\epsilon = 1.22$.

2.3.3 Chemical Kinetics: The Advanced Quasiglobal Model

It has long been noted that an important limitation of the original basic quasiglobal formulation is its inapplicability under fuel-rich conditions; e g., for fuel-air ratios greater than stoichiometric. For equivalence ratios greater than about 1.5, the adiabatic flame temperature predicted by the basic quasiglobal approach is greater than that observed in experiments, and the discrepancy between the predicted and measured adiabatic flame temperatures becomes larger as the combustion process becomes more fuel-rich. This is a serious difficulty with respect to diffusion flames in general and in liquid-fueled sudden-expansion combustor ram-jet applications in particular. In these devices the local fuel-air ratio in and near the flame-stabilizing recirculation regions has been found to be well above stoichiometric. Gas turbines as well often have fuel-rich primary zones in their combustion chambers. Thus a clear need exists for an improved quasiglobal model, in order to examine kinetic processes in fuel-rich combustor regions.

The basic reason that the original quasiglobal model formulation fails in the prediction of combustion processes in fuel-rich regions is that it does not include the fuel pyrolysis steps that occur in high temperature, oxygen deficient regions, but instead assumes a pure oxidation step for fuel consumption. In the fuel rich regions, both pure pyrolysis and oxidative pyrolysis steps occur to lead to the breakdown of the fuel into lower molecular weight components. At the same time, soot formation occurs: while this process does not soak up a large amount of energy, it does result in the formation of particulates that strongly increase the radiative heat loss from the flame. This radiation enhancement results in both a decrease in the overall temperature (and thus can directly affect the rate of heat release) and an increase in the heat load to the combustor walls. Based on these observations, the advanced quasiglobal model incorporates both fuel pyrolysis and soot formation steps.

In the advanced quasiglobal kinetics approach, the fuel to be modeled is broken down into aromatic and aliphatic components: soot formation is dependent on the amount of aromatic fuel present. The aromatic and aliphatic components are modeled using rates which have been developed for toluene and iso-octane, respectively. That is, the model fuel component which can be treated as aromatic is assigned rates which have been developed by extensive comparison of toluene predictions with experimental data, and the model fuel component that can be treated as aliphatic is assigned the rates developed for iso-octane. Each of these fuels break down into secondary fuels, C_2H_2 from toluene and C_2H_4 from iso-octane, following the pure pyrolysis pathway, as well as partially oxidizing by attack from both O_2 and OH . The secondary fuels then react with the remaining OH and O_2 , and the wet CO mechanism follows. Table 6 illustrates these reactions, along with soot formation/consumption reaction.

While this remains a formidable list of reactions, our studies show that the accuracy of the predictions is most sensitive to the wet-CO portion of the mechanism. This observation indicates that further simplifications are possible depending on the information being sought. For example, Table 7 shows a simplified mechanism intended to examine the heat release distribution in a ramjet combustor where the flame is stabilized by a recirculation zone. In this example, many of the intermediates important in a lower temperature ignition process are presumed to be negligible because of the presence of the recirculation zone. Also, in this example the fuel, JP-7, has been modeled as $C_{12}H_{24}$, and has been treated as being aliphatic in character.

2.3.4 Fuel Injection Model

In addition to the basic components of a parabolic, directed flow analysis and a well-stirred reactor formulation, the modular concept includes other elements of the dump combustor flowfield, for example, the fuel injection process. The detail of the computation provided by the use

TABLE 6. TOLUENE AND ISO-OCTANE QUASIGLOBAL KINETICS MODEL

GLOBAL MECHANISM	A	B	E/R	POWER DEPENDENCIES
<u>Toluene (aromatic)</u>				
$C_7H_8 \rightarrow 3.5 C_2H_2 + 0.5 H_2$	1.7982 E10	0	3.5000 E4	$[C_7H_8]^{1.0}$
$C_7H_8 + 3.5 O_2 \rightarrow 7 CO + 4 H_2$	4.4963 E9	1	2.6785 E4	$[C_7H_8]^{0.5} [O_2]^{1.0}$
$C_7H_8 + OH \rightarrow 3.25 C_2H_2 + 0.5 CO + 0.5 H_2O + 0.75 H_2$	1.4721 E17	0	1.4510 E4	$[C_7H_8]^{1.0} [OH]^{1.0}$
<u>Iso-Octane (aliphatic)</u>				
$C_8H_{18} \rightarrow 4 C_2H_4 + H_2$	1.0473 E12	0	3.5229 E3	$[C_8H_{18}]^{1.0}$
$C_8H_{18} + 4 O_2 \rightarrow 8 CO + 9 H_2$	1.2900 E9	1	2.5160 E4	$[C_8H_{18}]^{0.5} [O_2]^{1.0}$
$C_8H_{18} + OH \rightarrow 3.75 C_2H_4 + 0.5 CO + 0.5 H_2O + 1.5 H_2$	2.0000 E17	0	1.4919 E4	$[C_8H_{18}]^{1.0} [OH]^{1.0}$
<u>Secondary Fuel</u>				
$C_2H_2 + 6 OH \rightarrow 4 H_2O + 2 CO$	4.7850 E15	0	1.3883 E4	$[C_2H_2]^{1.0} [OH]^{1.0}$
$C_2H_2 + 2 OH \rightarrow 2 CO + 2 H_2$	2.8000 E16	0	0	$[C_2H_2]^{1.0} [OH]^{1.5}$
$C_2H_4 + 6 OH \rightarrow 2 CO + 2 H_2O + H_2$	2.2020 E15	0	1.2079 E4	$[C_2H_4]^{1.0} [OH]^{1.0}$
$C_2H_4 + 2 OH \rightarrow 2 CO + 3 H_2$	2.1129 E27	-3.0	6.3062 E3	$[C_2H_4]^{1.0} [OH]^{1.5}$
$C_2H_2 + O_2 \rightarrow 2 CHO$	4.0000 E12	0	1.4092 E4	$[C_2H_2]^{1.0} [O_2]^{1.0}$
$C_2H_4 + M \rightarrow C_2H_2 + H_2 + M$	2.0293 E17	0	3.9810 E4	$[C_2H_4]^{1.0} [M]^{1.0}$
<u>Soot Reactions</u>				
$C_7H_8 \rightleftharpoons HC \rightarrow soot$	-4.0455 E14*	-2.0	1.6110 E4	$[HC]^{1.43} [O_2]^{-0.5}$
$soot + O_2 \rightarrow CO_2$	$[soot] = -12 P_{O_2} A_t \left[\frac{K_A X}{1 + K_Z P_{O_2}} + K_B (1-X) \right]$ $X = \left[1 + K_T / (K_B P_{O_2}) \right]^{-1}$ $K_i = A_i \exp \left\{ -E_i / RT \right\}, i = A, B, T, Z$			
$i = A$ B T Z	2.0000 E1 4.4600 E-3 1.5100 E5 2.1500 E1	0 0 0 0	1.5090 E4 7.6490 E3 4.8820 E4 -2.0630 E3	As indicated by the equation for [soot]
where $A_t = 6 (C_s / \rho_s + D_s)$ (cm ² surface/cm ³), P_{O_2} = partial pressure of O ₂ (atm), C_s = (g = soot/cm ³ of gas), ρ_s = (g = soot/cm ³ of soot), D_s = diameter of soot (cm), [soot] = mass of soot/volume of gas (g/cm ³).				
* sign on A indicates rate of formation of soot				

TABLE 6. (Continued)

ELEMENTARY MECHANISM	A	B	E/R
<u>HC Fragmentation Mechanism</u>			
$\text{CH}_4 + \text{OH} = \text{H}_2\text{O} + \text{CH}_3$	3.0000 E13	0	3020.0
$\text{CH}_4 + \text{O} = \text{OH} + \text{CH}_3$	2.0000 E13	0	4640.0
$\text{CH}_4 + \text{H} = \text{H}_2 + \text{CH}_3$	1.2600 E14	0	5989.0
$\text{CH}_3 + \text{O} = \text{H} + \text{HCHO}$	1.3000 E14	0	1006.0
$\text{CH}_3 + \text{O}_2 = \text{OH} + \text{HCHO}$	1.7000 E 12	0	7045.0
$\text{CH}_2 + \text{H} = \text{H}_2 + \text{CH}$	2.5210 E11	0.67	12934.1
$\text{CH}_2 + \text{OH} = \text{H}_2\text{O} + \text{CH}$	2.5120 E11	0.67	12934.1
$\text{CH}_2 + \text{O}_2 = \text{OH} + \text{CHO}$	1.0000 E14	0	1862.0
$\text{CH} + \text{O}_2 = \text{O} + \text{CHO}$	1.0000 E13	0	0
$\text{CH} + \text{CO}_2 = \text{CO} + \text{CHO}$	1.0000 E10	0.5	2.0000 E3
$\text{CH} + \text{OH} = \text{H} + \text{CHO}$	5.0000 E11	0.5	5.0000 E3
$\text{CH} + \text{O} = \text{H} + \text{CO}$	5.0000 E11	0.5	0
$\text{CH}_4 + \text{M} = \text{H} + \text{CH}_3 + \text{M}$	4.0000 E17	0	44500.0
$\text{CH}_3 + \text{H} = \text{CH}_2 + \text{H}_2$	2.0000 E11	0.7	1510.0
$\text{CH}_3 + \text{OH} = \text{CH}_2 + \text{H}_2\text{O}$	6.0000 E10	0.7	1010.0
<u>Wet CO Mechanism</u>			
$\text{H}_2 + \text{O}_2 = \text{OH} + \text{OH}$	1.7000 E13	0	2.4070 E4
$\text{OH} + \text{H}_2 = \text{H}_2\text{O} + \text{H}$	2.1900 E13	0	2.5900 E3
$\text{OH} + \text{OH} = \text{O} + \text{H}_2\text{O}$	6.0230 E12	0	5.5000 E2
$\text{O} + \text{H}_2 = \text{H} + \text{OH}$	1.8000 E10	1.0	4.4800 E3
$\text{H} + \text{O}_2 = \text{O} + \text{OH}$	1.2200 E17	-0.91	8.3690 E3
$\text{M} + \text{O} + \text{H} = \text{OH} + \text{M}$	1.0000 E16	0	0
$\text{M} + \text{O} + \text{O} = \text{O}_2 + \text{M}$	2.5500 E18	-1.0	5.9390 E4
$\text{M} + \text{H} + \text{H} = \text{H}_2 + \text{M}$	5.0000 E15	0	0
$\text{M} + \text{H} + \text{OH} = \text{H}_2\text{O} + \text{M}$	8.4000 E21	-2.0	0
$\text{CO} + \text{OH} = \text{H} + \text{CO}_2$	4.0000 E12	0	4.0300 E3
$\text{CO} + \text{O}_2 = \text{CO}_2 + \text{O}$	3.0000 E12	0	2.5000 E4
$\text{CO} + \text{O} + \text{M} = \text{CO}_2 + \text{M}$	6.0000 E13	0	0

M indicates general third body.

TABLE 6. (Continued)

ELEMENTARY MECHANISM	A	B	E/R
<u>HCHO Mechanism</u>			
$\text{HCHO} + \text{OH} = \text{H}_2\text{O} + \text{CHO}$	3.0000 E13	0	0
$\text{HCHO} + \text{H} = \text{H}_2 + \text{CHO}$	1.7000 E13	0	1.5100 E3
$\text{HCHO} + \text{O} = \text{OH} + \text{CHO}$	3.0000 E13	0	0
$\text{CHO} + \text{OH} = \text{H}_2\text{O} + \text{CO}$	3.0000 E13	0	0
$\text{CHO} + \text{H} = \text{H}_2 + \text{CO}$	1.0000 E14	0	0
$\text{CHO} + \text{O} = \text{OH} + \text{CO}$	1.2600 E14	0	0
$\text{HCHO} + \text{HO}_2 = \text{H}_2\text{O}_2 + \text{CHO}$	1.0000 E12	0	4.0300 E3
$\text{CHO} + \text{HO}_2 = \text{O}_2 + \text{HCHO}$	1.0000 E14	0	1.5100 E3
$\text{CHO} + \text{O}_2 = \text{HO}_2 + \text{CO}$	3.1620 E12	0	3.5230 E3
$\text{HCHO} + \text{M} = \text{H} + \text{CHO} + \text{M}$	5.0120 E16	0	3.6240 E4
$\text{CHO} + \text{M} = \text{CO} + \text{H} + \text{M}$	5.0000 E14	0	9.5620 E3
<u>H₂O₂ Mechanism</u>			
$\text{H} + \text{H}_2\text{O}_2 = \text{OH} + \text{OH} + \text{H}$	1.2600 E17	0	2.2900 E4
$\text{H}_2\text{O}_2 + \text{O}_2 = \text{HO}_2 + \text{HO}_2$	3.9800 E13	0	2.1440 E4
$\text{H}_2\text{O}_2 + \text{H} = \text{H}_2 + \text{HO}_2$	1.5850 E12	0	1.9120 E3
$\text{H}_2\text{O}_2 + \text{OH} = \text{H}_2\text{O} + \text{HO}_2$	1.0000 E13	0	9.0600 E2
$\text{HO}_2 + \text{OH} = \text{O}_2 + \text{H}_2\text{O}$	5.0100 E13	0	5.0300 E2
$\text{HO}_2 + \text{O} = \text{O}_2 + \text{OH}$	5.0100 E13	0	5.0300 E2
$\text{HO}_2 + \text{H} = \text{OH} + \text{OH}$	2.5000 E14	0	9.5630 E2
$\text{HO}_2 + \text{H} = \text{O}_2 + \text{H}_2$	2.5100 E13	0	3.5230 E2
$\text{H} + \text{O}_2 + \text{M} = \text{HO}_2 + \text{M}$	1.5800 E15	0	-5.0340 E2
$\text{HO}_2 + \text{CO} = \text{CO} + \text{OH}$	1.0000 E10	0	0

M indicates general third body.

TABLE 7. FINITE RATE KINETICS MODEL USED IN RAMJET COMPUTATIONS

GLOBAL MECHANISM	A	B	E/R	POWER DEPENDENCIES
<u>Primary Fuel</u>				
$C_{12}H_{24} \rightarrow 6 C_2H_4$	1.0473 E12	0	3.5229 E4	$[C_{12}H_{24}]^{1.0}$
$C_{12}H_{24} + 6 O_2 \rightarrow 12 CO + 12 H_2$	1.2900 E9	1	2.5164 E4	$[C_{12}H_{24}]^{0.5} [O_2]^{1.0}$
$C_{12}H_{24} + OH \rightarrow 5.75 C_2H_4 + 0.5 CO + 0.5 H_2O + 0.5 H_2$	2.0000 E17	0	1.4919 E4	$[C_{12}H_{24}]^{1.0} [OH]^{1.0}$
<u>Secondary Fuel</u>				
$C_2H_4 + 6 OH \rightarrow 2 CO + 4 H_2O + H_2$	2.2020 E16	0	1.2079 E4	$[C_2H_4]^{1.0} [OH]^{1.0}$
$C_2H_4 + 2 OH \rightarrow 2 CO + 3 H_2$	2.1129 E27	-3	6.3062 E4	$[C_2H_4]^{1.0} [OH]^{1.5}$
$C_2H_2 + 6 OH \rightarrow 4 H_2O + 2 CO$	4.7850 E15	0	1.3883 E4	$[C_2H_2]^{1.0} [OH]^{1.0}$
$C_2H_2 + 2 OH \rightarrow 2 CO + 2 H_2$	2.8000 E16	0	0.0	$[C_2H_2]^{1.0} [OH]^{1.5}$

ELEMENTARY MECHANISM	A	B	E/R	
<u>Wet CO Mechanism</u>				
$CO + OH = H + CO_2$	4.0000 E12	0.0	4.0260 E4	--
$OH + H_2 = H_2O + H$	2.1900 E13	0.0	2.5900 E4	--
$OH + OH = O + H_2O$	6.0230 E12	0.0	5.5000 E2	--
$O + H_2 = H + OH$	1.8000 E11	1.0	4.4800 E3	--
$H + O_2 = O + OH$	1.2200 E17	-0.91	8.3690 E3	--
$O_2 + H_2 = OH + OH$	1.7000 E13	0.0	2.4070 E4	--
$CO + O_2 = O + CO_2$	3.0000 E12	0.0	2.5000 E4	--
$O + H = OH + M$	1.0000 E16	0.0	0.0	--
$H + H = H_2 + M$	5.0000 E15	0.0	0.0	--
$H + OH = H_2O + M$	8.4000 E21	-2.0	0.0	--
$CO + O = CO_2 + M$	6.0000 E13	0.0	0.0	--
$M + C_2 = O + O$	2.5500 E18	-1.0	5.9386 E4	--
$M + C_2H_4 = H_2 + C_2H_2 + M$	2.09E3 E17	0.0	3.9810 E4	--

of a parabolic directed flow analysis is the key feature of the modular model that allows the inclusion of a fuel injection module. This is particularly true in the case of liquid fuel injection, for at the fuel/air ratios appropriate for ramjet combustor operation, the liquid fuel streams initially occupy a very small portion of the overall combustor cross-sectional area. The liquid fuel injection model makes use of a combination of empirical information and turbulent mixing calculations. For example, the fuel jet penetration from the wall is computed through the use of an empirical penetration correlation (Ref. 23), using a breakup time correlation (Ref. 24) to estimate the downstream distance at which penetration is to be computed. That is, it is assumed that the fuel jet has turned parallel to the airflow at the axial position at which the initial fuel jet has broken up into droplets, as given by the breakup time correlation and the local airflow velocity.

Since the basic modular model formulation involves an axisymmetric flowfield, individual fuel jets cannot be resolved, and it is assumed that the liquid fuel spray forms an annulus whose cross-sectional area may either be specified or computed based on an assumed fuel spray bulk velocity. A bulk spray evaporation correlation is then used to compute the fuel vaporization rate; this correlation (Ref. 25) is a function of the initial velocity and temperature difference between the fuel spray and the surrounding air stream. Spreading of the fuel jet is computed through use of a turbulent mixing hypothesis as for the mixing process in the remainder of the parabolic flow. Fig. 25 shows the results of a computation of the fuel injection process for three fuel injectors, located in the combustor inlet wall, along with the centerline, and in a midstream position. Shown are the computed contours of the fuel mass fraction, α_F , with the vapor-phase fuel shown as the solid line and the liquid-phase fuel as the dotted line, as a function of both axial and radial position in the combustor inlet. For these calculations the air inlet velocity was approximately 700 ft/sec at a temperature of 1600°K; the overall fuel/air equivalence ratio was 0.6. The results shown in Fig. 25 provide a good example of the detail of the fuel injection process available through use of this aspect of modular modeling.

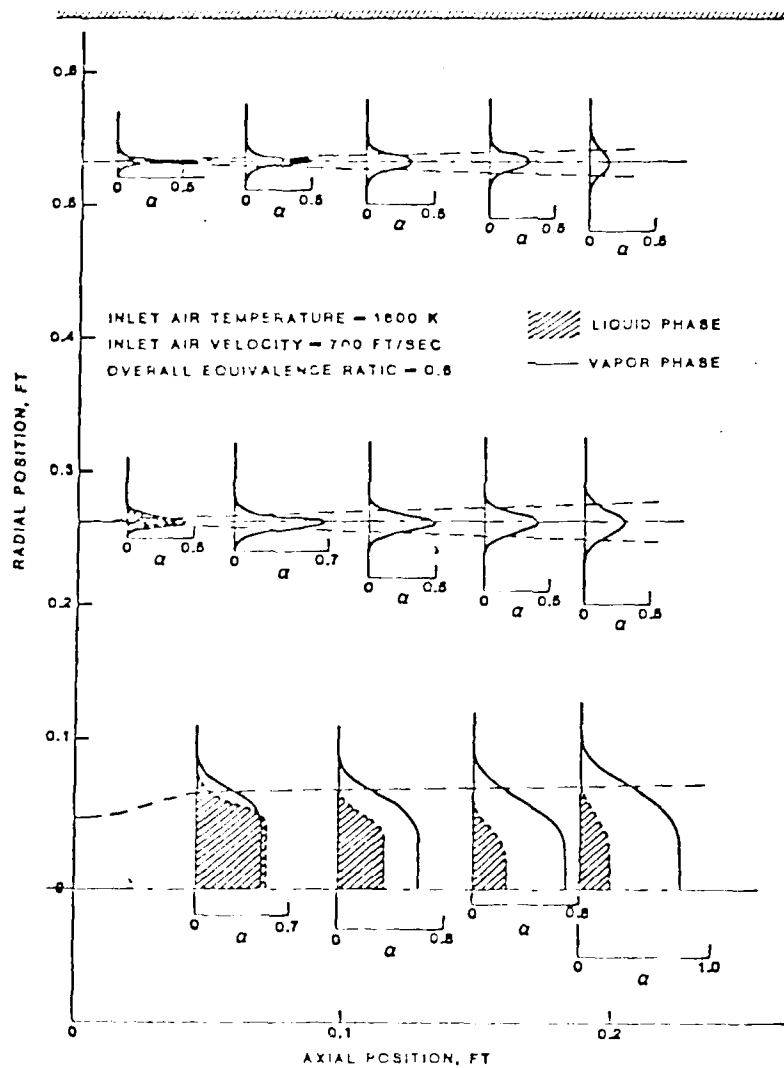


Figure 25. Predicted Fuel Mass Fraction Distributions for Simultaneous Injection at Three Radial Locations

2.3.5 Iteration Procedure

The overall logic of the calculation procedure is shown schematically in Fig. 26. Inlet conditions can be defined upstream or downstream of the fuel injection station as required; if liquid fuel injection is specified, the penetration and spreading of the liquid fuel jets are computed as described in the preceding section. The computation proceeds to the dump plane in the sudden-expansion combustor, at which point the dependent variables in the flowfield are stored for later use in the recirculation zone iteration procedure.

An initial state of the stirred reactor must be specified in order to begin the iteration procedure. This state is reasonably arbitrary, except that a reacted temperature level must be specified. The shape of the dividing streamline separating the directed flow and the recirculation zone must also be specified, along with the shear stress level, expressed as a "skin friction" coefficient. The initial stirred reactor state, in conjunction with a model for the shear layer between the recirculation zone and the directed flow then defines the boundary conditions for the parabolic directed flow calculation. Directed flow computations are carried out to the axial station at which the end of the recirculation zone has been defined; as part of these computations the diffusive flux of species and energy across the dividing streamline is computed. These fluxes then define a new set of stirred reactor "feed rates," i.e., species and energy fluxes into the recirculation zone region. Convergence of the procedure is defined by the change in the stirred reactor feed rates from iteration to iteration; each species and the energy flux must change less than 1.0% before the convergence criteria are satisfied. If they are not, the species and energy fluxes, and the overall diffusive mass flux and physical recirculation zone volume are used to compute a new stirred reactor state. The pressure required for this computation is taken to be the arithmetic average of the pressures computed as part of the directed flow solution at the beginning and end of the recirculation region. The new stirred reactor state is then used to define the directed flow boundary conditions, and the computation is restarted from the

AD-A148 371

COMBUSTION IN HIGH SPEED AIR FLOWS(U) SCIENCE
APPLICATIONS INC CHATSWORTH CA COMBUSTION SCIENCE AND
ADVANCED TECHNOLOGY DEPT R B EDELMAN ET AL. JUL 84
AFOSR-TR-84-0924 F49620-80-C-0082

2/2

UNCLASSIFIED

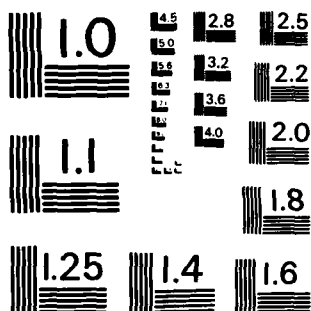
F/G 21/2

NL

END

FILMED

DTIC



MICROCOPY RESOLUTION TEST CHART
NATIONAL BUREAU OF STANDARDS-1963-A

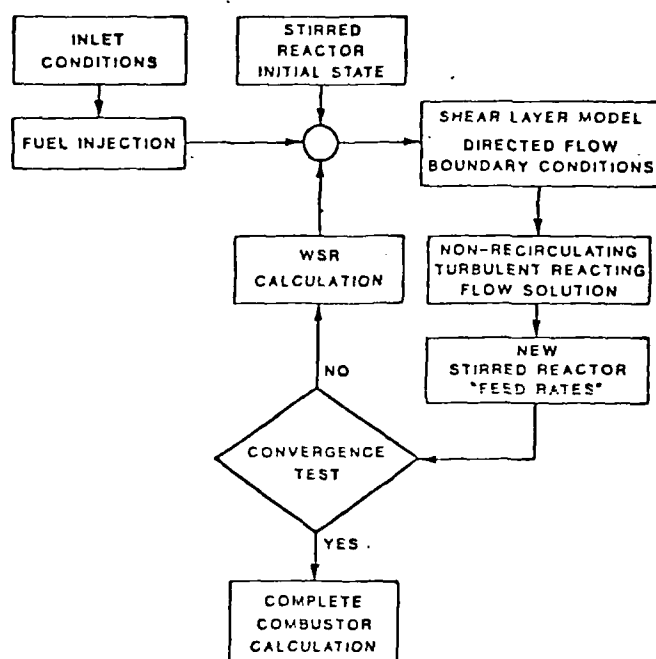


Figure 26. Modular Model Calculation Logic

dump station. When convergence is achieved, typically in 3-5 iterations, the combustor calculation is continued to the specified combustor exit station.

2.3.6 Modular Model Assessment

A variety of applications of different versions of the modular model have been reported in the literature, Refs. 20 and 21, and performance calculations have been carried out for several types of sudden expansion ramjet combustors, with inlet conditions including premixed, uniform inlet profiles, wall and in-stream orifice fuel injectors, and wall-mounted poppet type fuel injectors.

An early set of modular model validation comparisons included the sudden expansion ramjet combustor results described by Craig, et al. (Ref. 26). This work involved a combustor L/D of 3, a dump area ratio A_3/A_2 of 2.25, and an exit nozzle area ratio $A_2/A_3 = 0.40$. Cold flow and reacting flow experimental results are both reported for this configuration. In the modular model computations, the cold flow data were used to evaluate the model coefficient values for the specific configuration, and computations of a premixed dump combustor at a fuel/air ratio of 0.053 were then carried out using these coefficient values for comparison with the data presented in Ref. 26. In the experiments, the fuel used was JP-4 which was represented in the computations by propane. Both a simple one-step global finite-rate chemistry model and the full hydrocarbon oxidation kinetics as represented by the quasiglobal model were used to represent the chemical kinetics processes in the directed flow. A global model was used for the recirculation zone in all cases. Propane was chosen to represent the fuel because it adequately simulates from a heat-release standpoint the actual fuel used and because previous studies with propane had resulted in the development of a one-step finite-rate kinetics model for this fuel. This one-step model represents fairly accurately the ignition delay for propane-air (although not the overall reaction time) over a range of conditions of interest in this work. Initial conditions included an inlet total temperature of 554°K and an inlet static pressure of 1.83 atm. With a mass flow rate of 1.57 kg/sec, the inlet velocity and static temperature were

159 m/sec and 543°K, respectively; the inlet Mach number was 0.351. Initial turbulent kinetic energy and dissipation rate values were established in the same manner as for the cold flow calculations, and the geometry of the combustor and recirculation zone was the same as in the cold flow calculations.

Both combustion efficiency and wall static pressure distribution data are available for this configuration, and the results of the modular model calculation of these quantities are shown in comparison with the experimental data in Fig. 27. The combustion efficiency was computed from the mass-average temperature at each axial location in the calculation, using the JANNAF temperature-rise combustion efficiency definition. For these data, T_{T5} (ideal) = 2178°K. Note that in these comparisons, data points are shown for the fuel/air ratio 0.053 value at which the computations were carried out. These data points were obtained from plots of combustion efficiency vs. fuel/air ratio presented in Ref. 26 for three different values of combustor L/D. The band shown for each data point represents the range of observed combustion efficiencies as a function of fuel/air ratio and is a better indication of the overall trend of the combustion efficiency vs. length data than are the individual data points themselves. Some caution is advised in interpreting the combustion efficiency comparison shown in Fig. 27 since three different combustor configurations were involved in obtaining the data. Thus the relationship between recirculation zone length and combustor length is different for each of the three combustors tested. On the other hand, the static pressure data (for the fuel-air ratios which bracket the fuel-air ratio used in the computation) and the predictions are both for a combustor L/D of 3.0.

Overall, the level of agreement with the experimental data is reasonably good, although there is a drop in both combustion efficiency and wall static pressure towards L/D = 3 in the prediction that is not evident in the data. Both of these differences between prediction and experiment may be related to the inaccuracies inherent in the simple one-step global finite-rate model used in these calculations. Of greater interest, however, is the overall low level of combustion efficiency shown by these results, with a maximum combustion efficiency of less than 0.6 at L/D = 3. While this represents a short combustor, the premixed inlet condition should

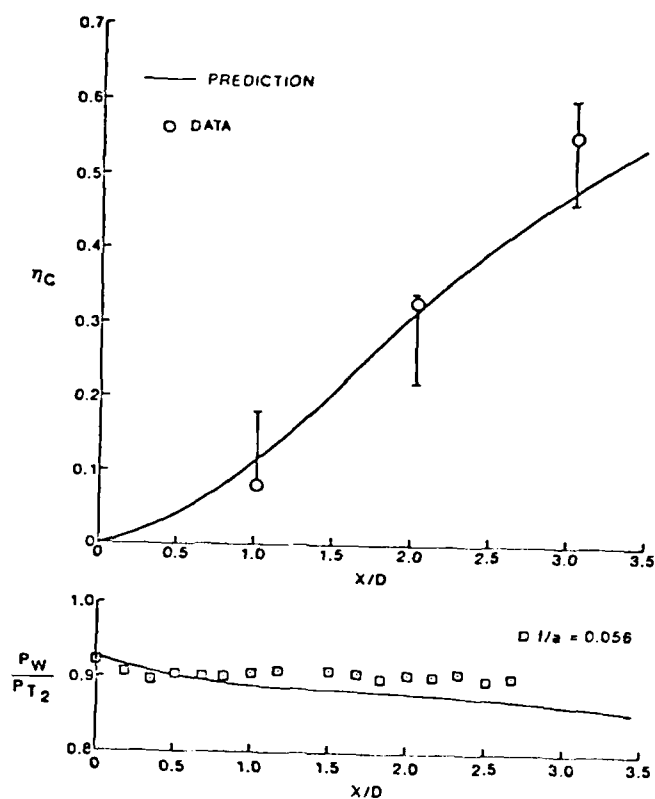


Figure 27. Comparison of Predicted and Measured Combustion Efficiency and Wall Static Pressure Distributions, Premixed Sudden-Expansion Combustor, Global Finite-Rate Chemistry Model

alleviate some of the combustion efficiency problems that short, flameholderless sudden-expansion combustors are known to exhibit. In this case the computation shows that the low combustion efficiency arises from the fact that the combustion is premixed. With a uniform directed flow fuel/air ratio, the recirculation region is also at the same overall fuel/air equivalence ratio which, in this case, is relatively lean ($\phi \approx 0.8$). Thus the recirculation region temperature is lower than it would be at an equivalence ratio nearer 1.0. Since it is the recirculation region that stabilizes the flame, and provides the energy source for flame propagation into the directed flow, this results in relatively slow flame propagation and an overall low combustion efficiency.

While these results indicate a good overall level of agreement with experimental data for a premixed combustor, the nonpremixed case involving liquid fuel injection is of considerably greater practical interest. As a test of the applicability of the modular approach (which, as described in Section 3.4, incorporates a semiempirical model for liquid fuel injection) to the analysis of nonpremixed ramjet combustor flowfield, the experimental configuration tested by Schmotolocha and Economos (Ref. 27) was selected. For these experiments an area ratio $A_3/A_2 = 9$ combustor was used, with liquid JP-4 injected perpendicularly from the inlet walls through an equally-spaced ring of orifices located 6 in. upstream of the dump plane. The inlet air Mach number for this combustor was 0.49 and the global fuel/air equivalence ratio was 0.63. Since the experiments involved a heavy wall combustor, and the code is presently limited to either adiabatic or isothermal wall boundary conditions, the effects of heat loss to the walls on the predicted temperature-rise combustion efficiency were approximated by using a lower air temperature value measured at the exit of the combustor during isothermal testing in place of the actual inlet air temperature.

Model coefficients were taken to be those established from the modeling of the premixed dump combustor described earlier in this section, despite the large difference in dump area ratio between the combustor used by Craig, et al. (Ref. 26) and the present combustor. Results of these compu-

tations are shown in Fig. 28. In the lower part of Fig. 28, the computed combustion temperature distribution is shown. Coalescence of the isotherms along the recirculation zone boundary reflects the highly turbulent shear layer region. The predicted equivalence ratio in the recirculation zone, ϕ_{RZ} , is 1.87, as compared to a measured value of 1.70, for the globally fuel-lean overall equivalence ratio of $\phi_0 = 0.63$. Note that the vaporization process resulting from liquid fuel injection into the 1110°R airstream effectively reduces the heterogeneous mixture temperature levels, as shown by the presence of a 1000°R isotherm. A comparison of predicted and measured radial temperature profiles is provided at the combustor exit plane. As expected, the measured temperature near the wall is lower than theoretical due to local heat loss. In the region near the centerline the local temperature is substantially underpredicted, which could result from deficiencies inherent in the turbulence modeling or in the global finite-rate chemical kinetics model (which substantially overpredicts the required reaction time compared to a more complete chemical kinetics formulation), or both. However, the mass flow in this region is small relative to the overall combustor mass flow, so that overall combustion efficiency, which is based on mass-averaged temperatures, is well represented. This is shown in the upper part of Fig. 28; the two experimental points represent combustion efficiency obtained from exit species distributions and from exit total temperature.

These results indicate another feature of the modular model, which is its depiction of the details of the flowfield that result from the interaction between the fuel injection process and the distribution of fuel at the inlet and within the recirculation region. For example, a variety of observations have shown that with wall orifice fuel injection, the recirculation zone equivalence ratio is generally more fuel-rich than the overall (global) equivalence ratio. This result has been demonstrated by the data of Schmotolocha and Economos (Ref. 27), which was obtained for three different inlet conditions and at two different locations of the fuel injection orifices upstream of the dump plane. Indeed, the data described in Ref. 27 indicate that for overall equivalence ratios greater than 0.2, the equivalence ratio in the recirculation zone is always greater than

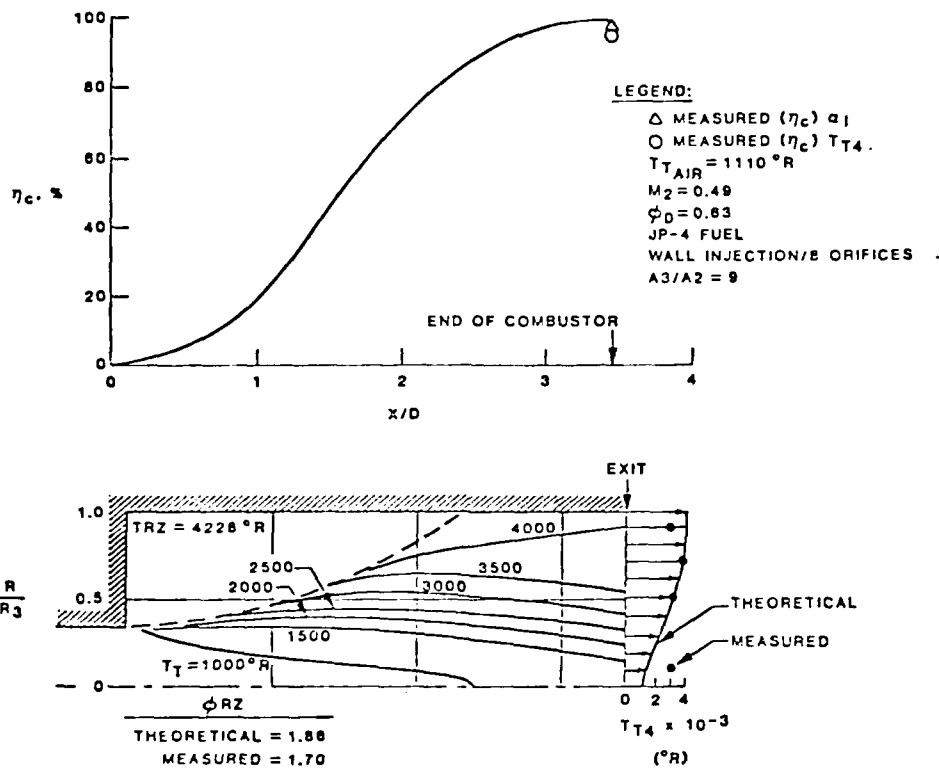


Figure 28. Comparison of Modular Model Prediction with Measured Dump Combustor Performance, Liquid Fuel Injection. Data from Ref. 27.

unity. These data are shown in Fig. 29, in which the results of modular model calculations at two overall equivalence ratios are also shown. The comparison between the data of ref. 27 and the calculations indicates good agreement; what the computational detail shows is that this result arises from the fact that although the peak equivalence ratio in the fuel-air distribution at the inlet plane is away from the wall and within the directed flow, the equivalence ratio near the wall and thus adjacent to the recirculation zone downstream of the dump plane is still substantially greater than one.

Poppet fuel injectors provide, by their design, a fuel penetration that is basically independent of fuel flow rate over their design range. This can be accounted for within the modular model approach by assigning a fixed value for fuel penetration distance and bypassing the fuel penetration calculation described in Section 2.3.4. Fuel mixing and vaporization are still accounted for using the semiempirical approach outlined in the latter section. Recent work carried out at SAI has involved the investigation of ramjet combustor performance characteristics for engines using poppet fuel injectors, for flight conditions representing relatively low Mach numbers. Results of some of this work are shown in Fig. 30; these calculations make use of the version of the modular model incorporating the advanced quasiglobal formulation. The comparison shown in Fig. 30 indicates that the computational results agree very well with the available data. Since a fixed radial fuel injection location was assumed for these calculations, the equivalence ratio in the recirculation region is only slightly above stoichiometric and the temperature is essentially the same in all cases. The performance dropoff observed in both the experimental data and the calculational results as $\phi \rightarrow 1.0$ is a result of the increasing region of fuel-rich equivalence ratio as the overall (global) equivalence ratio approaches one. Combustion in this fuel-rich region results in lower temperatures than are produced by stoichiometric or slightly fuel-lean combustion. Since the ideal equilibrium temperature is that achieved by a one dimensional combustion process starting from the average combustor inlet temperature and at the average fuel-air ratio of the flow, the actual mass-averaged temperature for the nonuniform stream will remain

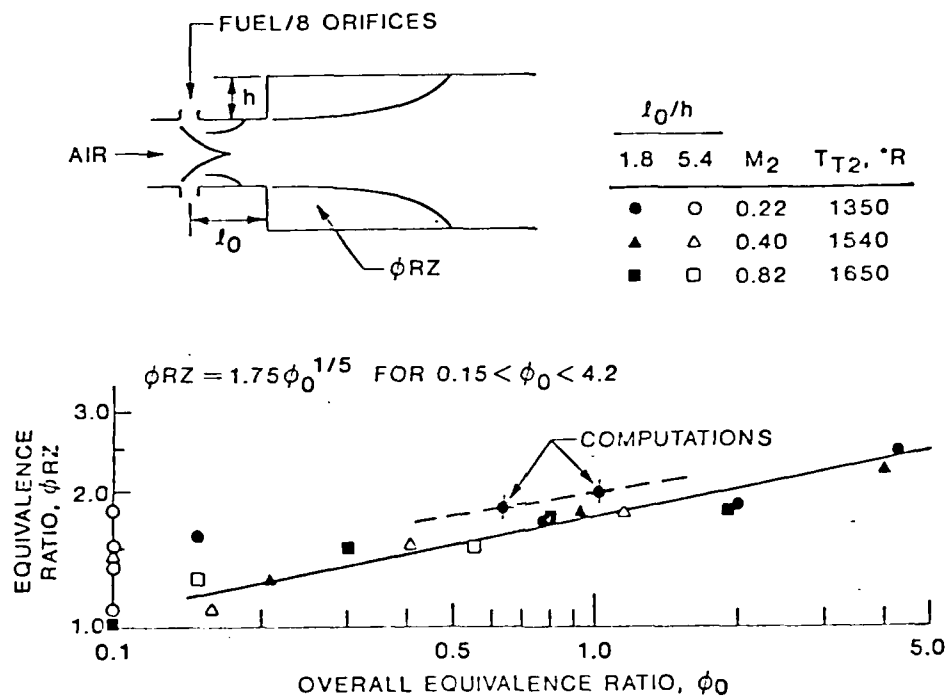


Figure 29. Recirculation Zone Fuel Concentration

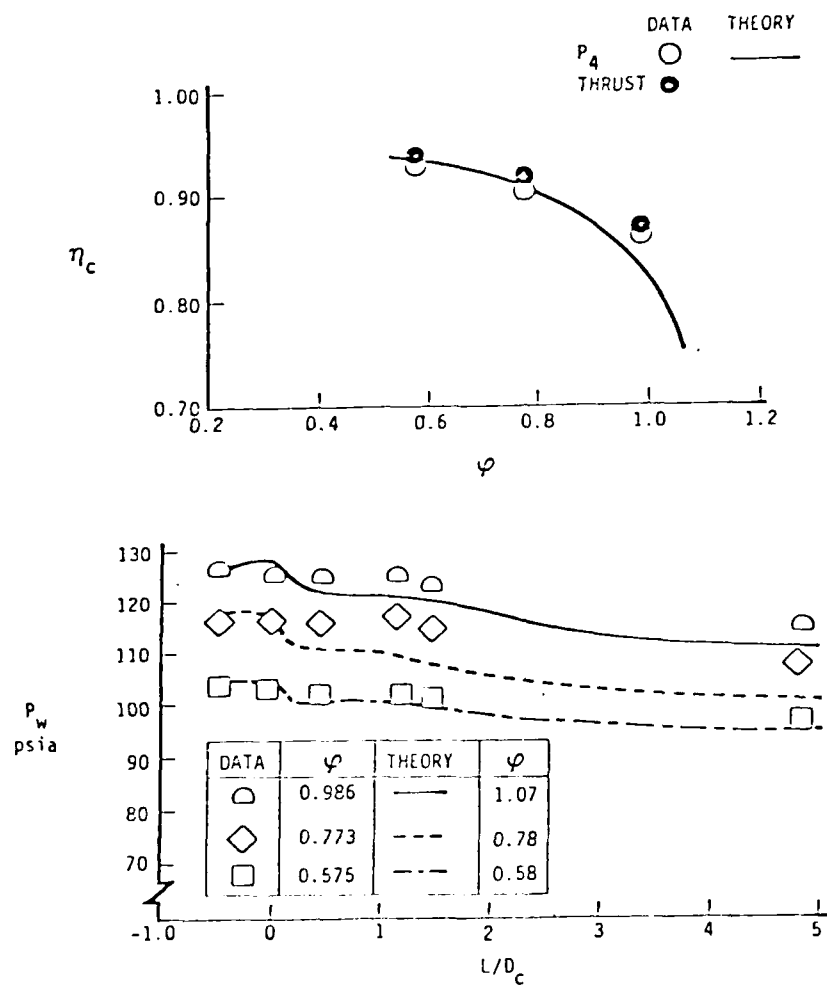


Figure 30. Combustor Performance Prediction, Poppet Injection

lower, even when all fuel is consumed. Thus there is a dropoff in combustion efficiency that represents the nonuniformity of the flow upstream of fuel ignition in the directed flow.

2.3.7 Discussion

The results documented in this section provide considerable evidence of the overall accuracy of the modular formulation for a ramjet combustor model. They also provide certain insights, particularly with respect to the interaction of the mixing and combustion processes, that are useful in interpreting the results obtained in ramjet test programs. For example, the results just discussed indicate that the high fuel-air ratio efficiency falloff that is often seen in ramjet performance data results from the existence of locally fuel-rich gases when the overall fuel-air ratio is stoichiometric and the fuel is injected just upstream of the combustor inlet. However, the results for a premixed combustor also shown in this section show that at lower overall fuel-air ratios a uniformly mixed inlet stream does not provide high levels of performance either. In this case, because the inlet flowfield is premixed, and at an overall low equivalence ratio, the flame-stabilizing recirculation zones are also operating fuel-lean. This results in a recirculation zone temperature that can be considerably less than the stoichiometric flame temperature and thus a reduced rate of propagation of the flame out of the recirculation zones and across the flow. When the fuel is injected from discrete injectors just upstream of the combustor inlet, the modular model results show, in agreement with experiment, that the recirculation zone equivalence ratio is essentially always greater than unity, i.e., fuel-rich. For an overall fuel-lean combustor operation, this results in higher recirculation zone temperatures than would be achieved in a premixed combustor and hence enhanced flame propagation and improved combustion efficiency.

The value of this approach lies both in its utility as a tool for the investigation of the fundamental mechanisms that underlie observed ramjet performance trends and in serving as a foundation for further development of more sophisticated approaches, incorporating, for example, treatments of the two-phase flow in a spray combustion situation. Indeed, one of the considerations involved in the development of the spray flame code discussed at the beginning of this section is that it be compatible with and usable as the directed flow portion of a spray-combustor modular model. Combination of this spray code and advanced versions of the boron particle combustion treatments with the modular model framework outlined in this section would provide a useful tool for the investigation of slurry-fuel combustion. Finally, it is possible to incorporate the effects of swirl into the directed flow module while using the stirred-reactor formulation to represent the large-scale recirculation regions that are formed as a result of the application of large amounts of swirl to a flow. Such an extension of the approach would provide a useful tool for the investigation of fundamental phenomena in chemically-reacting swirling flowfields.

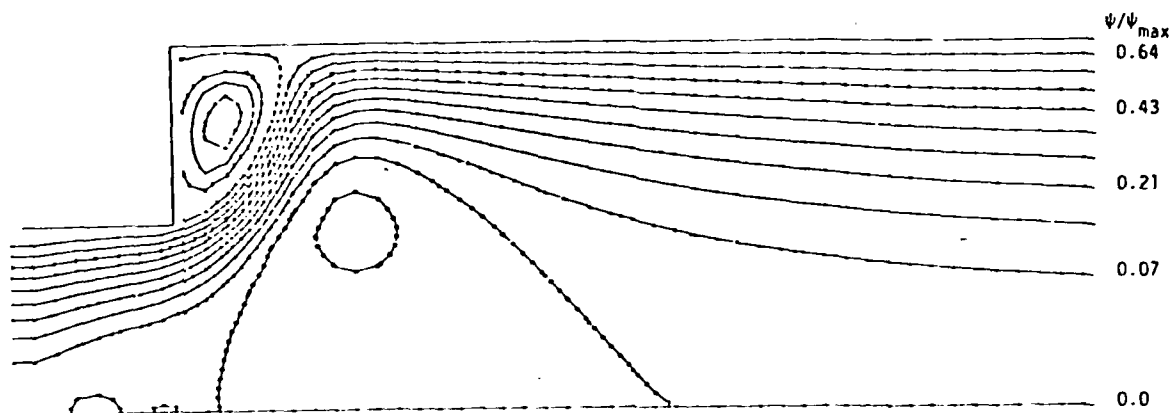
2.3.8 Turbulence Models for Ramjet Flowfields

Another aspect of the ramjet modeling work carried out under the present program is the investigation of advanced turbulence models. Although the two-equation $k-\epsilon$ approach has provided quite widely useful, and is incorporated in the modular model developed as part of this program, it does rest on a gradient diffusion assumption for momentum transfer, and questions have been raised as to the applicability of this approach. The gradient diffusion assumption is avoided if the Reynolds stress equations are solved directly, but this adds three coupled partial differential equations to the set to be solved. If it is assumed, however, that convection and diffusion of each of the Reynolds stresses can be related to convection and diffusion of turbulence kinetic energy, then the partial differential equations reduce to algebraic expressions and only the turbulent kinetic energy (and turbulent kinetic energy dissipation rate) equations remain to be solved; their solution is accomplished in the same manner as in the two-equation model.

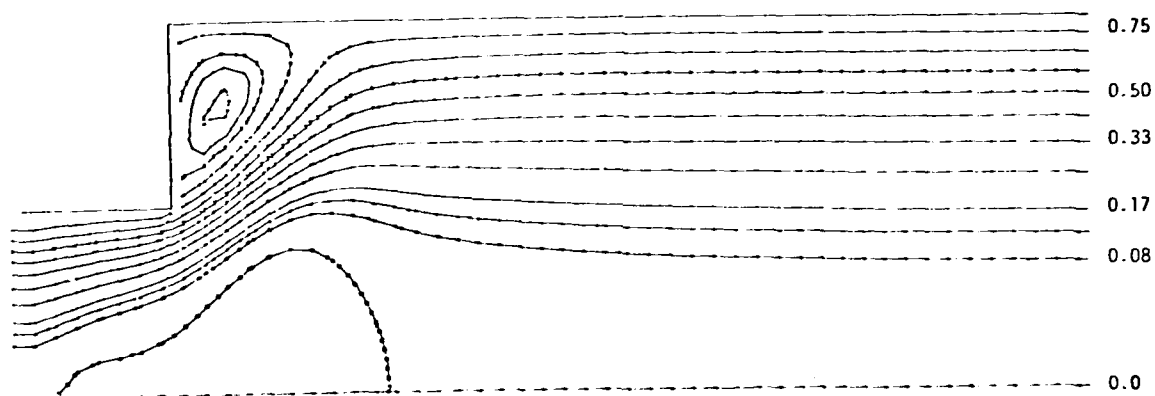
The assumption that convection and diffusion of Reynolds stress can be related directly to convection and diffusion of turbulent kinetic energy forms the foundation of the algebraic stress model (ASM) first proposed by Rodi (Ref. 28). Since each stress component is obtained directly, this approach avoids use of a gradient diffusion hypothesis. Moreover, for flows in which multiple stress components are apparent, e.g., swirl flows, the ASM approach avoids an isotropic eddy viscosity assumption and avoids any empirical relationship between different stress components. This can result in substantial differences in overall flowfield prediction, as is evidenced by the results shown in Fig. 31. These results are for a constant-angle swirl flow at a swirl number of 2, with identical initial and boundary conditions for each computation. Note that while both approaches yield closely similar outer recirculation zone lengths, there are large differences in the predicted extent and location of the centerline recirculation zones, as well as in the uniformity of the exit flow. This latter characteristic is indicated by the parallelism of the stream function contours at the exit in the $k-\epsilon$ model prediction, compared to the convergence toward the centerline of the stream function contours predicted by the ASM model, as well as the near-wall value of normalized stream function.

Although the results shown in Fig. 31 indicate strong differences between the predictions of the two turbulence model formulations, there is as yet insufficient data with which to evaluate the two approaches, particularly with respect to swirling dump combustor flows. However, work already carried out (Ref. 3) has shown that the use of the ASM formulation does improve predictions in planar recirculating flows with large amounts of streamline curvature, and indirect evidence (such as observations of recirculation zone size and levels of exit-plane nonuniformity) also indicates that further development of the ASM formulation should be pursued.

A second aspect of the comparison of turbulence model results for swirling ramjet combustor flowfields involves the examination of the effects of different initial swirl distributions. An example of this is provided by the results shown on Figs. 32 and 33, which show radial profiles of axial (Fig. 32) and tangential (Fig. 33) velocity, for a swirling flow in a 1.5:1



(a) ALGEBRAIC STRESS MODEL



(b) k- ϵ MODEL

Figure 31. Flowfield Streamlines, Sudden-Expansion with Swirl; Swirl No. = 2.0, Constant Angle

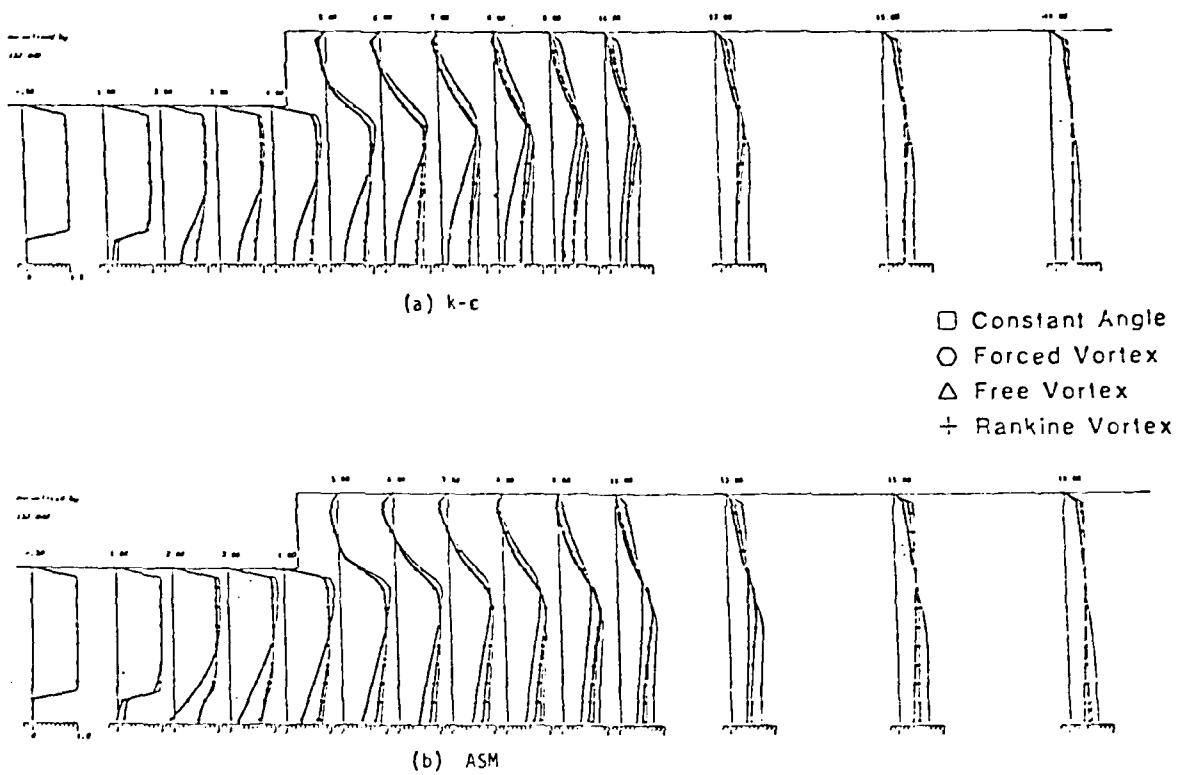


Figure 32. Axial Velocity Profiles, $S = 0.4$,
Different Initial Swirl Distributions

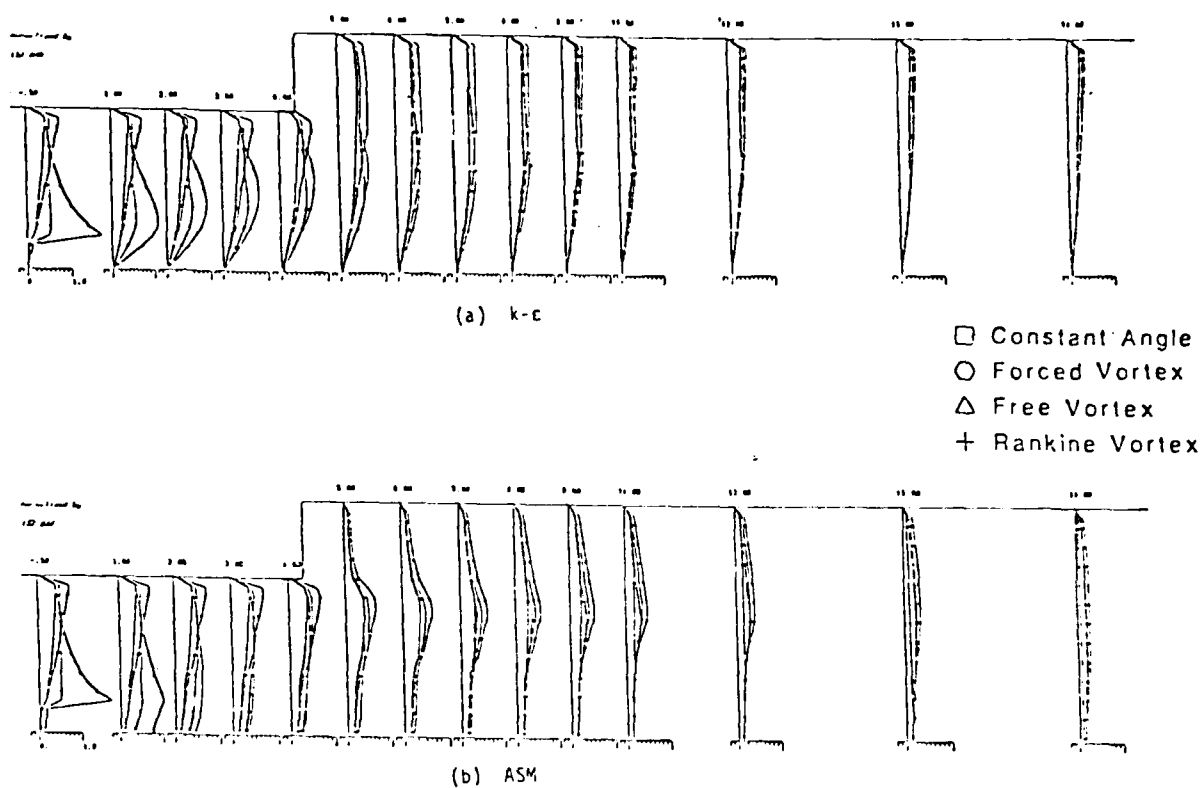


Figure 33. Tangential Velocity Profiles, $S = 0.4$, Different Initial Swirl Distributions

diameter ratio sudden expansion for four different types of inlet swirl. Note that the low area ratio was chosen to minimize inertial effects and thus maximize the effects of the turbulence model formulation on the flowfield prediction. The overall swirl number in this demonstration is held constant at 0.4, and there is a centerbody at the origin of this flow (within the inlet). A nonuniform 37 (axial) by 26 (radial) grid was used, and predictions are shown for both a two-equation and ASM turbulence model. Despite the small size of the figures, it is immediately apparent from the tangential velocity profiles shown in Fig. 33 that the ASM approach prediction of the downstream mixing-out process differs substantially from that predicted using the two-equation approach. It was noted earlier that there is a tendency in the work reported in the literature for predictions of swirl flows to relax to a profile characteristic of a forced vortex, ωr , whatever the initial tangential velocity distribution. Such a tendency is observable in the profiles predicted using the $k-\epsilon$ approach shown on Fig. 33(a), but the ASM predictions, Fig. 33(b) do not exhibit this tendency. This effect thus appears to be directly related to the existence of an isotropic eddy viscosity assumption implicitly in the $k-\epsilon$ model application, whereas with the ASM (different) effective viscosities are obtained for each of the three shear stress components.

2.4 MODELING OF THE DUCTED ROCKET COMBUSTION PROCESS

The work being carried out in this program under the task area outlined in Section 1(d) had as its objective the development of a new theoretical model to describe the three-dimensional reacting flow typical of multiple-inlet ducted-rocket combustion chambers. It was supported, through AFOSR, by the Ramjet Division (RJT), AFWAL. Because of the paucity of experimental data on the aerodynamics of the ducted rocket configuration, the modular model development work under this task area utilized the hierarchy of models concept, in which unified elliptic aerodynamic models were used to define characteristic flowfield regions for the development of modular models which incorporate the fundamental chemical kinetic formulations required to address the performance aspects of ducted rockets.

Aerodynamic calculations were carried out for a three-dimensional configuration similar to an experimental ducted rocket combustor tested at AFWAL/RJT. The three-dimensional elliptic analysis used for these computations was a modified version of an analysis similar to the Imperial College TEACH code, incorporating a two-equation turbulent kinetic energy turbulence model similar to that used for the computations described in Sections 2.1 and 2.3. A three-dimensional grid is, of course, required, with 21 axial, 10 radial, and 18 circumferential grid points. This grid is not fine enough to provide grid-independent results, but since it involves 3780 node points it is a compromise between the fineness needed to obtain grid-independence and the limitations of computer storage and speed*. The configuration examined involves two symmetrically-disposed inlets at 180° apart: this is not identical to the AFWAL configuration but was selected to simplify the implementation of boundary conditions in these computations. A sketch of this combustor geometry is shown in Figure 34, from which it can further be seen that the inlets are disposed at an angle of 45° to the longitudinal axis of the combustor. The air inlet velocity was selected to correspond to an airflow rate of 2 lb/sec/inlet.

The velocity vectors computed for this flow field in a plane through the inlets and along the combustion centerline are shown in Fig. 35. Two recirculation zones can be seen, one at the head end of the combustor and the second along the outer walls just downstream of the inlets. Contours outlining the approximate sizes of these recirculation regions are shown on Fig. 35. For fuel injection in the inlet arms (i.e., the side-dump liquid fueled ramjet configuration) both of these recirculation regions are potential flameholding sites. However, if fuel is injected from the combustor head end (the ducted rocket configuration) it would be expected that the primary flameholding region would involve the recirculation zone at the combustor head end.

*The solution procedure involves eight variables: three velocity components, the pressure, the flow enthalpy, and a species used as a tracer, as well as the turbulent kinetic energy and its dissipation rate. Thus for the grid noted, 30,240 locations are required for the storage of the dependent variables alone, for this nonreacting (but possibly nonisothermal) calculation.

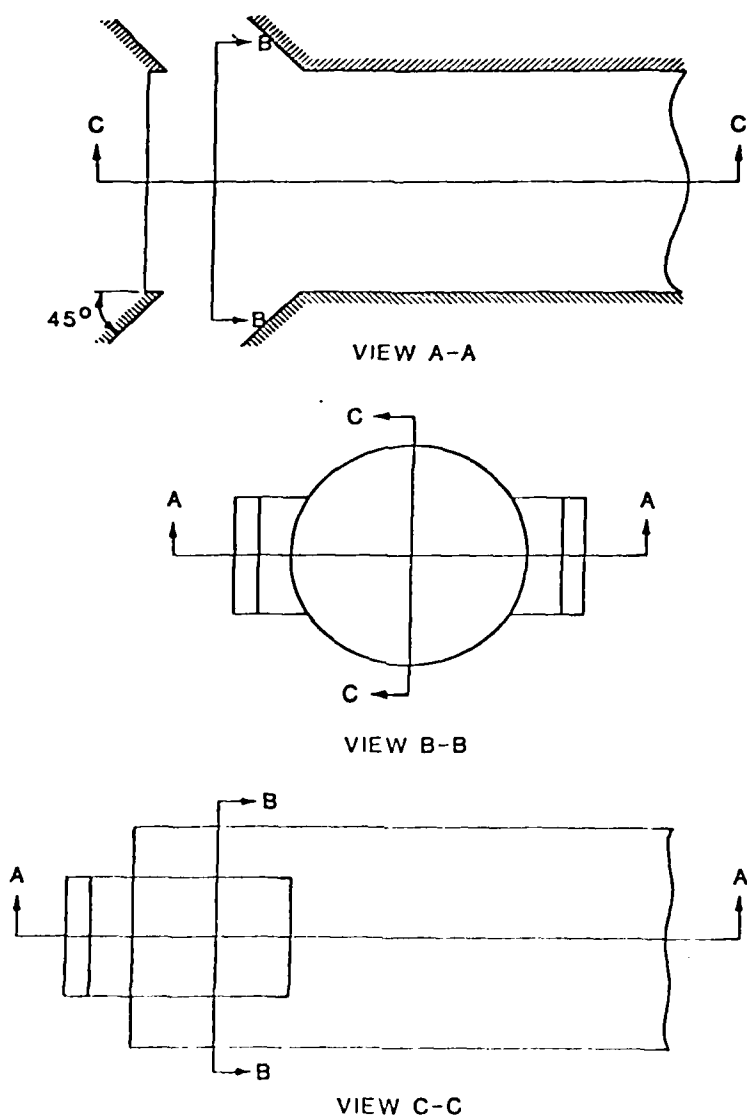


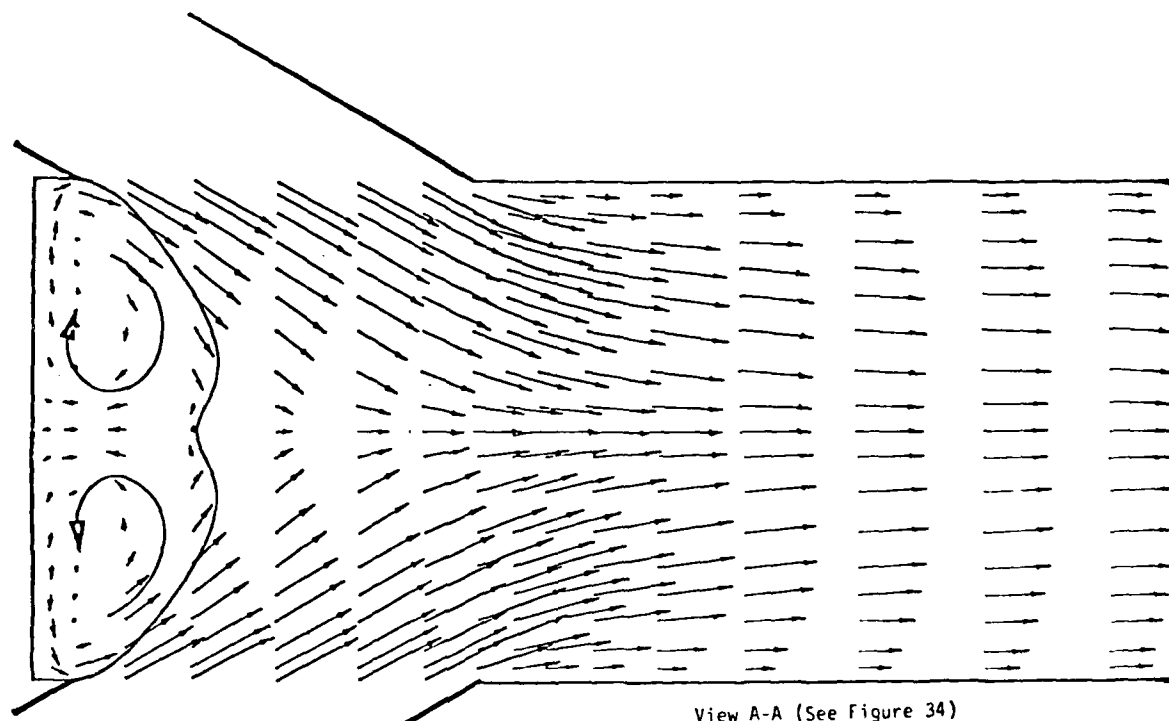
Figure 34. Schematic of Ducted Rocket Configuration for Aerodynamic Flowfield Analysis

The radial extent of the recirculation zone at the head end of the ducted rocket combustor is depicted in Fig. 36. Of interest in this view are the distinctive four-lobed shape of the recirculation region and the stagnation point shown on the flowfield centerline. Through computations such as represented by Figs. 35 and 36 it is possible to build up a three-dimensional view of the size and shape of the recirculation zones in the ducted rocket combustor. This provides one of the required pieces of information for the development of a modular model of this flowfield.

Various types of modular models can be postulated for a flowfield such as shown in Figs. 35 and 36. However, one of the most useful, because of its computational speed and flexibility, is the well-stirred reactor/plug flow with distributed secondary injection/entrainment approach. In this model the intense mixing that occurs in the region of the inlets in the ducted rocket combustor is modeled using a well-stirred reactor formalism, while the subsequent mixing and combustion of fuel and air not transported into the recirculation zone is modeled as a plug flow with distributed entrainment. While this approach is fast and flexible, it requires, in addition to a specification of the size and shape of the recirculation zone, a measure of the proportion of the flow involved in the recirculation region and in the subsequent mixing region. This specification of the proportion of the flow found in different regions can be provided using the elliptic aerodynamic formulation with a species tracer.

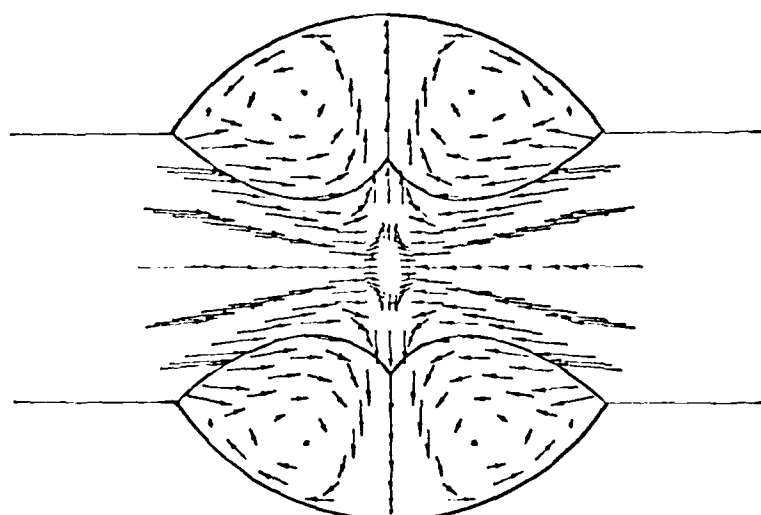
Calculations carried out to date to examine the mixing and kinetics limitations within the side-dump combustor used at AFWAL have not been successful. In part this state of affairs arises from the complexity of the overall flowfield, but in general the characteristics of the combustor appear to be such that kinetics are not limiting. Mixing-limited situations are inherently more difficult to approach with the sort of modular model being applied in this phase of the program. The work in this specific area is continuing under a follow-on AFOSR contract.

It should be noted that the configuration tested at AFWAL is not a true ducted rocket but represents a side-dump ramjet combustor configuration. One of the essential features of a ducted rocket is the presence at the head end of the combustor of one or more jets of higher temperature,



View A-A (See Figure 34)

Figure 35. Longitudinal Cross-Section through Inlet Arms, Ducted Rocket Combustor Aerodynamic Flowfield



View B-B (See Figure 34)

Figure 36. Lateral Cross-Section through Inlet Arms, Ducted Rocket Combustor Aerodynamic Flowfield

fuel-rich, partially reacted products of the rocket combustion process. These jets are sonic, or more usually, highly underexpanded supersonic flows. Thus the flowfield within a true ducted rocket involves both subsonic and supersonic regions, with strong shock and pressure wave interactions, and could be expected to be considerably different in character from the flowfield shown in Figs. 35 and 36. This aspect has not been accounted for in any ducted rocket modeling so far described and will be considered in continuing SAI work in this area.

2.5 REFERENCES

1. Edelman, R.B., Schmotolocha, S., and Slutsky, S., "Combustion of Liquid Hydrocarbons in a High Speed Airstream," AIAA Journal, Vol. 9, No. 7, July 1971, pp. 1357-1364.
2. Hossain, M.S., and Rodi, W., "Equations for Turbulent Buoyant Flows and Their Modeling," Report SFB 80/T/46, Sonderforschung bereich 80, Ausbreitungs - and Transportvorgänge in Strömungen, Universität Karlsruhe, December 1974.
3. Sindir, M.M., and Harsha, P.T., "Assessment of Turbulence Models for Scramjet Flowfields," NASA CR 3643, November 1982.
4. Genovese, J., Edelman, R.B., and Fortune, O.F., "Some Aspects of Two-Phase Flows with Mixing and Combustion in Bounded and Unbounded Flows," Journal of Spacecraft & Rockets, Vol. 8, No. 4, April 1971, pp. 352-357.
5. Heys, N.W., Roper, F.G., and Kayes, P.J., "A Mathematical Model of Laminar Axisymmetrical Natural Gas Flames," Computers and Fluids, Vol. 9, 1981, pp. 85-103.
6. Edelman, R.B., et al., "Gas Generator Fueled Scramjet Program Part III, Theoretical and Experimental Investigations of Metal Particle Combustion in a Supersonic Gas Stream," AFAPL TR 70-84, 1971, pp. 20-37.
7. Edelman, R.B., Farmer, R.C., and Wang, T.-S., "Combustion and Emissions of Synthetic Fuel Components," Combustion of Synthetic Fuels, William Bartok, ed., ACS Symposium Series 217, American Chemical Society, 1983, pp. 29-48.
8. Edelman, R.B., and Harsha, P.T., "Laminar and Turbulent Gas Dynamics in Combustion - Current Status," Progress in Energy and Combustion Science, Vol. 4, No. 1, 1978, pp. 1-62.
9. Shearer, A.J., Tamura, H., and Faeth, G.M., "Evaluation of a Locally Homogeneous Flow Model of Spray Evaporation," Journal of Energy, Vol. 3, No. 5, September - October 1979, pp. 271-277.
10. Mao, C.P., Szekely, G.A., Jr., and Faeth, G.M., "Evaluation of a Locally Homogeneous Flow Model of Spray Combustion," Journal of Energy, Vol. 4, No. 2, March - April 1980, pp. 78-87.
11. King, M.K., "Boron Particle in Hot Gas Streams," Combustion Science and Technology, Vol. 8, 1974, pp. 255-273.
12. King, M.K., "Boron Ignition and Combustion in Air-Augmented Rocket After-burners," Combustion Science and Technology, Vol. 5, 1972, pp. 155-164.
13. Meese, R.A., and Skifstad, J.G., "Ignition and Global Combustion Models for Clouds of Boron Particles," AIAA Journal, Vol. 12, No. 1 (1974), pp. 71-77.

14. Vovchuk, Y.I. et al., "High Temperature Combustion of an Immobile Boron Particle in an Oxygen-Bearing Medium," Combustion, Explosion and Shock Waves, Vol. 11 (1975), pp. 471-476.
15. Mohan, G. and Williams, F.A., "Ignition and Combustion of Boron in O_2 /Inert Atmospheres," AIAA Journal, Vol. 10, No. 6 (1972), pp. 776-783.
16. Edelman, R.B. et al., "Part III: Theoretical and Experimental Investigation of Metal Particle Combustion in a Supersonic Gas Stream," Gas Generator Fueled Scramjet Program, 1971, AFAPL-TR-70-84, pp. 20-37.
17. Edelman, R.B., Genovese, J., and Fortune, O.F., "Some Aspects of Two-Phase Flows with Mixing and Combustion in Bounded and Unbounded Flows," Journal of Spacecraft and Rockets, Vol. 8, No. 4 (1971), pp. 82-87.
18. Yang, W.T. D. Eng. Thesis, School of Engineering, Yale University, 1963.
19. Edelman, R.B., and Economos, C. "Theoretical Investigation of Metal Particle Combustion in a Supersonic Gas Stream," AFAPL-TR-70-84, Part III, Air Force Aero Propulsion Laboratory, January 1971.
20. Harsha, P.T., Edelman, R.B., Schmotolocha, S.N., and Pederson, R.J. "Combustor Modeling for Ramjet Development Programs," Ramjets and Ram-rockets for Military Applications, AGARD-CP-307, March 1982, Paper 29.
21. Harsha, P.T., and Edelman, R.B., "Assessment of a Modular Ramjet Combustor Model," Journal of Spacecraft and Rockets, Vol. 19, No. 5, Sept.-Oct. 1982, pp. 430-436.
22. Launder, B.E., et al., Prediction of Free Shear Flows - A Comparison of the Performance of Six Turbulence Models," Free Turbulent Shear Flows, Vol. 1, Conference Proceedings, NASA SP-321, 1973, pp. 463-519.
23. Catton, I., Hill, D.E., and McRae, R.D., "Study of Liquid Jet Penetration in a Hypersonic Stream," AIAA Journal, Vol. 6, No. 11, Nov. 1977, pp. 2084-2089.
24. Clark, B., "Break-up of a Liquid Jet in a Transverse Flow of Gas," NASA TN D-2424, Aug. 1964.
25. Ingebo, R., and Foster, H., "Drop Size Distribution for Cross-Current Break-up of of Liquid Jets in Air Stream, NASA TN-4087, Oct. 1957.
26. Craig, R.R., Drewry, J.E., and Stull, F.D., "Coaxial Dump Combustor Investigation," AIAA Paper 78-1107, July 1978.
27. Schmotolocha, S.N., and Economos, C., "An Experimental Combustion and Flame Stabilization Study of Dump Burners," AFOSR TR-75-1446, Sept. 1975.
28. Rodi, W., "The Prediction of Free Turbulent Boundary Layers by Use of a Two-Equation Model of Turbulence," Ph. D. Thesis, University of London, 1972.

3. PUBLICATIONS

1. Edelman, R.B., Harsha, P.T., and Schmotolocha, S.N., "Modeling Techniques for Ramjet Combustion Processes," AIAA Journal, Vol. 19, No. 5, May 1981, pp. 601-609.
2. Harsha, P.T., "Combustion Modeling for Dractical Applications," Prediction of Turbulent Reacting Flow in Practical Systems, T. Morel, Ed., New York, ASME, 1981.
3. Harsha, P.T., Edelman, R.B., Schmotolocha, S.N., and Pederson, R.J., "Combustor Modeling for Ramjet Development Programs," Ramjet and Ram-rockets for Military Applications, AGARD CPP-307, October 1981.
4. Harsha, P.T., and Edelman, R.B., "Assessment of a Modular Ramjet Combustor Model," Journal of Spacecraft and Rockets, Vol. 19, No. 5, September - October 1982, pp. 430-436.
5. Edelman, R.B., Farmer, R.C., and Wang, T.-S., "Combustion and Emission of Synthetic Fuel Components" Combustion of Synthetic Fuels, William Bartok, ed., ACS Symposium Series 217, American Chemical Society, 1983, pp. 29-48.
6. Harsha, P.T., and Edelman, R.B., "Computational Hierarchy for the Analysis of Combustion Phenomena in Ramjet Environments" Presented at 1984 JANNAF Propulsion Meeting, New Orleans, 7-9 February 1984. To be published by CPIA.
7. Harsha, P.T., and Edelman, R.B., "Analytical Modeling of a Spray Diffusion Flame," AIAA Paper 84-1317, Presented at AIAA/SAE/ASME 20th Joint Propulsion Conference, Cincinnati, 11-13 June 1984. Submitted for publication in AIAA Journal.

4. PROFESSIONAL PERSONNEL

The following personnel have contributed to the work discussed in this report:

1. Dr. R.B. Edelman
2. Dr. P.T. Harsha
3. Dr. T.-S. Wang
4. Dr. M.M. Sindir
5. Mr. W.N. Bragg
6. Mr. G.C. Cooper
7. Mr. C. Morrison

5. INTERACTIONS

5.1 PRESENTATIONS

During the course of this work, the following presentations were made:

1. "Combustion Modeling for Practical Applications," Presented at ASME Fluids Engineering Conference, June 22-24, 1981.
2. "Interpretation of Ramjet Combustor Test Data," Presented at AIAA/SAE/ASME 17th Joint Propulsion Specialist' Conference, July 22-29, 1981.
3. "Combustion Modeling for Ramjet Development Programs," Presented at AGARD Propulsion and Energetics Panel 58th Symposium, October 26-29, 1981.
4. "Mixing, Ignition and Combustion in Flowing, Reacting Fuel-Air Mixtures," Presented at 1981 AFOSR Combustion Dynamics Contractors' Meeting, Nov. 16-20, 1982.
5. "Mixing, Ignition and Combustion in Flowing, Reacting Fuel-Air Mixtures," Presented at 1982 AFOSR Combustion Dynamics Contractors' Meeting, Nov. 1-4, 1982.
6. "Modeling of Multi-Phase Flows in Ramjet Combustors," Presented at 1983 JANNAF Propulsion Meeting, Monterey, CA, February 15, 1983.
7. "Fundamental Processes in Spray Combustion" Presented at 1983 AFOSR Combustion Dynamics Contractors' Meeting, Sept. 19-23, 1983.
8. "Kinetics Limitations in the Consumption of Particulate Boron," Presented at 1983 AFOSR Combustion Dynamics Contractors' Meeting, Sept. 19-23, 1983.
9. "An Approach to Non-Gradient Diffusion in the Analysis of Turbulent Combustion" Presented at 1983 AFOSR Combustion Dynamics Contractors' Meeting, Sept. 19-23, 1983.
10. "Computational Hierarchy for the Analysis of Combustion Phenomena in Ramjet Environments" Presented at 1984 JANNAF Propulsion Meeting, New Orleans, February 7-9, 1984.
11. "Analytical Modeling of a Spray Diffusion Flame" Presented at AIAA/SAE/ASME 20th Joint Propulsion Specialist' Conference, June 11-13, 1984.
12. "Ducted Rocket Combustion Modeling" Presented at JANNAF Workshop on Ducted Rocket Combustors, Cincinnati, OH, June 13, 1984.

5.2 CONSULTATIVE AND ADVISORY FUNCTIONS

Two of the task areas of this program involve continuing and formal

interactions with DOD laboratories. The ducted rocket modeling work carried out under the task area outlined in Section 1(d) involves close interaction with experimental work carried out by Drs. F.D. Stull and R.D. Craig at AFWAL/RJT. In addition, the boron slurry modeling effort described in Section 1(c) involves coordination with experimental work being done by Dr. Klaus Schadow at NWC.

In addition, Dr. Edelman served on the Propulsion Technology Panel of the Military Space System Technology Model (MSSTM) evaluation activity for the Space Division of the Air Force Systems Command, and Drs. Edelman and Harsha have both been active in participating in JANNAF-sponsored workshops on swirl flows in ramjets, two-phase flow in ramjet combustors, and ducted rocket combustion technology.

END

FILMED

1-85

DTIC